Gamma detector system for nuclear fingerprinting

Alessia Giroletti

A dissertation submitted to the University of Bristol in accordance with the requirements of the degree of PhD in the Faculty of Science, School of Physics, Bristol

2019

~29000 words

Abstract

Mapping and measurement of radiation is a crucial activity to be performed when radioactive sources are involved, for example during decommissioning of existing nuclear power plants. These environments require fast and reliable devices able to identify the type and amount of the source but also to provide their geographical distribution. Since emitted photons have the longest life-time and carry specific energies typical for each isotope, gamma spectroscopy is the most common technique used. Spectrometers usually use semiconductor detectors. Their properties allow to build small and light detector systems. This makes them attractive for integration in Unmanned Air Vehicles (UAV). This is a key feature when considering deployment in hostile or dangerous conditions where human access is too dangerous. However, high precision spectroscopy systems have a limited bandwidth, which ultimately translates into a limit in the maximum dose rate they can measure. The system proposed overcomes this issue. The apparatus is based on a matrix of 5 different semiconductors (Silicon, Gallium Arsenide, Uranium Dioxide, Cadmium Zinc Telluride, and Diamond) which, thanks to their different response to incident photons of different energies, allow the identification of a large variety of isotopes by comparing count rates in the individual detectors after using a simple, fast thresholding system. This detector system allows the detection of the most common 12 isotopes (whose energies range from some keV to approximately 2 MeV) usually found in nuclear power plants at very high dose rates. A large GEANT4 simulation study was performed to prove the validity of the system, demonstrating that the detector will exhibit excellent performance as a fast readout gamma spectrometer in high radiation fields, and in addition will provide the location of the sources.

Acknowledgements

I would like to thank my University supervisors Prof. Tom Scott and Dr. Jaap Velthuis for all the support during these years and for the opportunity to develop my knowledge. I would also like to thank my Industry supervisor Mr. James Moore to give me the opportunity to find a solution for a challenging problem. Always from the academic side, I would like to thank Anna, Paolo, Yannick and David for their support and help in lab, with paper and with coffee!

With Leonor, Emma, Lana, Doug and Lana everything was much easier and for sure funnier, thanks to feed me with pocket coffee, salmon tea and chocolate. I am planning our lovely beach gazebo (with some risotto too)!

But the most important person for me during this period was Keith, a new friend always present. Thanks to make me smile during the hardest period uomo barbuto.

And thanks Cosimo, I do not have to say nothing more. Lulu.

Author's Declaration

I, Alessia Giroletti, declare that the work in this dissertation was carried out in accordance with the requirements of the University's Regulations and Code of Practice for Research Degree Programmes and that it has not been submitted for any other academic award. Except where indicated by specific reference in the text, the work is the candidate's own work. Work done in collaboration with, or with the assistance of, others, is indicated as such. Any views expressed in the dissertation are those of the author.

Signed

Date

Author's contribution

I was involved in all steps of the project. The central idea for the project came from my Supervisors, but all practical work including simulation study was performed by me. The preamplifier board was developed by myself with the support of Dr. Paolo Baesso and Dr. David Cussans, who helped me to debug the board. The work carried out in the particle physics laboratory at the University of Bristol was carried out by myself with the support of Dr. Yannick Verbelen, who helped to overcome the issues occurring during MAROC3 and FPGA tests. The readout board containing the MAROC3 and FPGA was created for the muon telescope system, another project which I was involved at the beginning of my PhD.

Contents

Abstract iv

Acknowledgements vi

Author's Declaration vi

Author's Contribution viii

Table of Contents xiii

List of Figures xxi

List of Tables xxiii

1 Introduction 1

2 Interaction of Radiation with Matter 5

2.1 Generation of Radiation 5

2.2 Nuclear decay mechanisms 6

2.3 Charged Particle Interactions with Matter 12

2.3.1 Interaction of matter in compound material 21

2.3.2 Landau distribution 21

2.4 Interaction of photons with matter 22

2.4.1 Photoelectric effect 22

2.4.2 Compton scattering 23

2.4.3 Pair production 27

2.4.4 Total Cross Section 28

2.5 Summary 32

3 Semiconductor-based detectors **33**

3.1 Semiconductor material 35

3.2 p-n Junction 39

3.3 Operating the pn-junction as a radiation detector 44

3.4 Signal generation in semiconductor devices 45

3.5 Summary 49

4 A Gamma Detector System for Nuclear Fingerprinting **51**

4.1 The device concept 52

4.2 Choice of semiconductor materials 56

4.3 Simulations 59

4.3.1 Simulation of the interaction of photons with matter 61

4.3.2 Dependence on material thickness at fixed energy 63

4.3.3 Dependence on energy for fixed thickness 68

4.3.4 Source Simulations 68

4.4 The reconstruction method 74

4.4.1 Radioisotopes identification 74

4.4.2 Relative activities studies 86

4.5 Supporting studies 90
4.6 Propagation in Water and air 90
4.7 Distances 92
4.8 Conclusion 95

5 Readout electronics and Muon Tomography 97

5.1 Signal processing chain 98
5.1.1 Single channel board test results 104
5.2 Muon tomography 107
5.2.1 Geevor system 107

6 Future Studies and Applications 113

6.1 Design Concept Options 113
6.2 Measurements and Future Development 116
6.3 Further System Application 116

7 Conclusion 119

A Signal generation and noise 121

A.1 Signal generation and acquisition 121
A.2 Detector response spectral broadening 122
A.2.1 Fano noise 123
A.2.2 Electronic noise 124

References 129

List of Figures

2.1 Decay level diagram for ^{60}Co [8]. 6

2.2 Binding energy per nucleon as function of the number mass A [10]. 7

2.3 Chart of observed nuclei. The colour indicates their type of decay [11]. 8

2.4 Range of α particles in dry air at sea level as a function of their kinetic energy [13]. 9

2.5 Stopping power of 5 MeV α particle in the air as function of the path lenght [12]. 10

2.6 The typical β spectrum for a ^{210}Bi emitting source [15, 16]. 11

2.7 Range of β particle in dry air at sea level [17]. 11

2.8 Sketch of the collision of an heavy charged particle with an atomic electron. 13

2.9 Energy lost by muons through a Cu layer [18]. 18

2.10 Radiation and collision contribution to the energy loss by electrons in copper [18]. 20

2.11 Landau distribution in Silicon for 500 MeV pions for different detector thicknesses [18]. 22

2.12 The cross section for the photoelectric effect in lead as a function of the photon energy. The cross section is obtained from [26]. 24

2.13 Sketch of Compton interaction. The incident photon interact with an electron which is consequently scattered with an angle ϕ. 25

2.14 Compton cross section in lead. 26

2.15 Deposited energy for Compton scattering. Two peaks are visible, the well defined photopeak at full peak energy and the spread Compton edge which covers a broad range of energies [14]. 27

2.16 Pair production cross section in lead as a function of the photon energy. 29

2.17 Total cross sections for lead and carbon as a function of energy. Where $\sigma_{p.e.}$ is the photoelectric effect cross section, ... 31

3.1 Energy band structure for semiconductor detector [28] 35

3.2 Energy band structure for semiconductor detector [28]. The orbital levels are shown to better identify the band structure correspond to each level. 37

3.3 On the left of the page the intrinsic Si, in the centre doping with n material and on the right with p material [29]. 39

3.4 p-n junction structure. 40

3.5 Forward and reverse bias effect on the junction. 42

3.6 Diagram of IV curve for forward and reverse bias. 43

3.7 The IV for a silicon detector at room temperature. 44

3.8 pn junction with a fully depleted region. The charge carriers are generate in x. The electric field direction is also showed. 46

3.9 Charge collection as a function of time. The charge collection time for holes is slower compare to the charge collection time for the electrons [31]. 49

4.1 Effects of radiation damage in semiconductor. 58

4.2 Geometry of the simulation. 60

4.3 Energy deposited by 1 MeV photon beam in different semiconductor materials. 61

4.4 Deposited energy spectrum generated by 0.8 MeV photons (in red) and by 2 MeV photons (in blue) in a 1 mm thick GaAs detector. . 62

4.5 Electron-hole pairs in 1 mm thick GaAs detector by 1 MeV photon beam. 63

4.6 Energy deposited by a 1 MeV photon beam as a function of different material thickness for: a) CdZnTe, b) UO_2, c) GaAs, d) Si, e) diamond, f) Ge and g) HgI_2 64

4.7 Energy deposited by a 1 MeV photon beam in all the detectors considered in the project. 66

4.8 Number of event collected in each detector per each energy in 1 mm of material. 67

4.9 Best material thickness combination. 67

4.10 Energy deposited by different photon energy beam in 1 mm thick material: a) CdZnTe, b) UO_2, c) GaAs, d) Si. 69

4.11 Energy deposited by different photon energy beam in 1 mm thick material: a) diamond, b) Ge and c) HgI_2. 70

4.12 Energy deposited in different detectors by 10^7 photons of different sources: a) ^{241}Am, b) ^{131}Ba, c) ^{6}0Co, d) ^{137}Cs, e) ^{152}Eu, f) ^{68}Ga. . 72

4.13 Energy deposited in different detectors by 10_7 photons of different sources: a) ^{131}I, b) ^{192}Ir, c) ^{85}Kr, d) ^{22}Na, e) ^{210}Po, f) ^{226}Ra. 73

4.14 In blue the number of electron-hole pairs produced in a 1 mm thick UO_2 detector is shown for a ^{60}Co source. The accumulation plot is shown in red. Please note the log scale on the y axis. 75

4.15 Fit template in all detectors for each source: a) CdZnTe, b) UO_2, c) GaAs, d) Si, e) diamond based on table 4.2. 76

4.16 Value of the reconstructed amplitude for the Eu in a)Si and the b)Ra amplitude in UO_2. 78

4.17 Gaussian fit for the reconstructed parameter for the Eu parameter in Si and Ra parameter in UO_2. 79

4.18 Fit to the reconstructed measured spectrum for 10^7 photons beam of Ba source in a 2 mm thick CdZnTe material. The dots represent the accumulation plot, while the red line is the fit. 80

4.19 Number of reconstructed photons as a function of the number of simulated photons from a Ba source in 2 mm thick CdZnTe material. Figure a) shows the reconstructed Ba source photons and figure b) the number of photons wrongly reconstructed as coming from a Ga source. The number of reconstructed photons for the Ba source increase linearly with the number of simulated photons while the number of photons reconstructed wrongly as coming from Ga remains 0 within errors. 81

4.20 Number of reconstructed photons as a function of the number of simulated photons from a Ir source in 1 mm thick GaAs material. Figure a) shows the reconstructed Ir source photons and figure b) the number of photons wrongly reconstructed as coming from a Na source. The number of reconstructed photons for the Ir source increase linearly with the number of simulated photons while the number of photons reconstructed wrongly as coming from Na remains 0 within errors. 82

4.21 Fit results for the mixtures summarised in table 4.6: a) mix 1, b) mix 2. 84

4.22 Fit results for the mixtures summarised in table 4.6 a) mix 3 and b) mix 4. 85

4.23 Comparison between simulated and reconstructed value for each source (Co, Am and Cs) and mix. 87

4.24 Number of reconstructed photons as a function of the number of simulated photons for different mixtures of Co, Ga and Na. 89

4.25 Different combinations of Co, Ga and Na. 90

4.26 Geometry of the simulation. 91

4.27 Spectrum of the energy deposited by 10^7 photons emitted by a Cs source in a 2 mm thick CdZnTe detector. The medium between the source and the detector was filled with air and water to simulate a human body. 92

4.28 Energy deposited by 10^7 photons emitted by a Cs source in a 2 mm thick CdZnTe. 93

4.29 Energy deposited by 10^7 photons emitted by a Cs source in a 2 mm thick CdZnTe. 94

4.30 Energy deposited by 10^7 photons emitted by a Cs source in a 2 mm thick CdZnTe at different distances. The medium between the detector and the source is water. 94

5.1 Sketch of readout chain. γ's generated by a radioactive source interact with the detector depositing resulting in the generation of charge. The detector is connected to a charge-sensitive preamplification/amplification stage connected to a MAROC3 chip. The MAROC3 chip converts the signal using an ADC and the signal is than collected and stored in the FPGA to be analysed and transferred to an external processor. 98

5.2 Component of readoud chain for semiconductor material [54]. 99

5.3 Readout chain and sketch indicating the signal shaping process. . . 100

5.4 The complete system. At the bottom the preamplifier board with a 500 μm thick Si detector on top. On the top the single MAROC3 board is shown 101

5.5 Schematic of the board with a single output. 102

5.6 Schematic of the board with 64 output channels. 103

5.7 Measured board response when a 10 pF capacitor is connected to the board to simulate detector and 15 mV pulses are injected into the capacitor. In red the Gaussian fit. 104

5.8 MCA board response when a 10 pF capacitor is connected to the board to simulate detector. The injected charge was varied from 10 mV and 30 mV. 105

5.9 MCA board response when a 10 pF capacitor is connected to the board to simulate detector. 105

5.10 MCA response when a 500 μm thick Si detector is connected to the amplifier board. 106

5.11 MCA response when a 500 μm thick Si detector is connected to the amplifier board and the Am source is placed 5 cm far from the detector surface. 107

5.12 In (a) is shown a structure of single RPC in all components. In (b) a picture of RPC built in Bristol laboratory is presented. 108

5.13 In (a) a picture of Geevor setup is presented. In (b) is shown the structure of cassettes and where trigger scintillators are located. . . 108

5.14 Muons rate data for (a) sea side case and (b) mountain case. 109

5.15 In (a) and (b) two particle tracks are displayed. In (c) an example of signal to noise ratio is shown. 110

5.16 Comparison between number of muons per each side. 111

6.1 Detectors placed on the same plane to maximise the solid angle covered. 113

6.2 Detectors placed one on top of the other to select the energy in each detector. 114

6.3 Mixture of configuration 1 and 2. 114

6.4 Triangular shape detector configuration without GaAs. In this configuration the detector can be swapped and added as required. . . . 115

A.1 Semiconductor detector material and its amplification chain. When the particle interacts with the material the electrons and holes produced during the process drift towards the cathode and anode respectively. The signal is transmitted to the preamplifier, shaper and finally to the amplifier. 122

A.2 Amplification chain. 126

A.3 Energy resolution of 3.1 mm^2, 2.5 mm thick CdZnTe detector [65]. . 128

List of Tables

1.1 Expected nuclear waste accumulated by 2125. 3

4.1 Energy levels of gammas emitted by the most common sources which can be found in nuclear power plants. 52

4.2 The threshold levels for each detector and energy. The upper number is the lower threshold value and the lower number is the higher threshold value. 55

4.3 Comparison of different semiconductors properties: density, bandgap, energy required to create an electron hole pair, charge carrier mobility and the atomic number ([30], [46], [31].) 59

4.4 Fit results for all 12 sources. 10^7 photons from ^{131}Ba were simulated and deposited their energy in 2 mm thick CdZnTe detector. As expected the only detected source was ^{131}Ba. 77

4.5 Minimum number of photons required to identify a source in each detector. 83

4.6 Mixtures of sources created. All the sources have the same amount. 86

4.7 Mixtures of sources created. The total amount was kept constant. . 86

4.8 Different mixtures combination of Co, Ga and Na. The amount for each source is specified as well as the total amount. 88

Chapter 1 | Introduction

The ability to identify radioactive sources, their activity and amount is a process of fundamental importance when radioactive materials are present. Examples of situations in which a fast, reliable radiation measurement is essential are during decommissioning of nuclear power plants, analyses of nuclear wastes, security reasons or when a nuclear accident takes place, such as the one that recently happened at the Fukushima Daiichi Nuclear Power Plant (FDNPP) [1–3]. In 2011 after the big earthquake in Tohoku, a tsunami was generated. The waves generated have hit the city of Okuma, where on the cost Fukushima Daiichi Nuclear Power Plant is located. The tsunami destroyed the emergency generator, while the nuclear reaction was already stopped. The refrigerator pumps were not able to keep the temperature at the correct value and the emission of radioactive sources occurred. For such situations, it is important to provide staff, involved in these situations, with easy to use tools that can provide this information, without coming in direct contact with the radioactive material.

The system proposed during this PhD work aimed to address this challenge and is presented in this thesis.

The life-cycle of a nuclear power plant can be divided into several phases: planning and design, construction, facility testing, operation, decommissioning and waste management [4, 5]. Decommissioning is defined as administrative and technical actions taken to allow the removal of some or all of the regulatory controls from a facility; also all steps leading to the release of a nuclear facility, other than a disposal facility, from regulatory control [6]. These steps include the processes of decontamination and dismantling. The decommissioning stage and waste storage are nowadays part of the planning of a nuclear power plant. Factors that are considered when the decommissioning is planned are the type and quantity of

radionuclides, feasibility of decommissioning, economic considerations and policy issues. In 2013, in the United Kingdom, 29 reactors were shut down and are at different stages of their decommissioning phase [4]. During the decommissioning phase it is important to identify the radioactive sources present for safety reasons: not only for the safety of employees responsible for decommissioning, but also to properly store the waste. The IAEA (International Atomic Energy Agency) indicates 3 different stages for nuclear decommissioning: remove fuel or process inventory, remove all ancillary plants and buildings, and complete the decommission to bring the territory back to green field [5]. In nuclear power plants radioactive waste is produced. The IAEA (International Atomic Energy Agency) defines radioactive nuclear waste as solid, liquid or gaseous nuclear material with no further use and which contains or is contaminated by radionuclides with radioactive levels higher than the clearance levels, determined by the authority [6]. Nuclear waste is typically divided into different categories, according to the level of danger they present, their half life and the heat generated: high level waste (HLW), intermediate level waste (ILW), low level waste (LLW) and very low level waste (VLLW). These exhibit different radiation levels and are stored in different ways. HLW is highly radioactive and is produced by spent fuel from reactors. Usually, these are stored in large containers with thick walls. The short lived elements are not separated from the elements with longer half-lives. To be sure that it is stored safely HLW is monitored continuously. ILW exceeds the LLW limits but does not generate any heat. This kind of waste includes the radioactive elements from the decommissioning of the reactor. Several techniques, such as consolidation, dissolution and concrete storage, are used to store ILW safely. VLLW and LLW are any material which has entered in contact with any contaminated material, or it was in a radioactive environment. In table 1.1 the volume of nuclear waste (of different types) that are predicted to be stocked by 2125 is listed [7]. The calculation is based on the stored waste in April 2016 in all the UK nuclear facilities. 2125 is the supposed year when all the current UK facilities will be fully decommissioned.

Type	Examples	Volume m^3	Activity (TBq)
HLW	Spent fuel	366	79×10^6
ILW	Steel graphite	299×10^3	3.8×10^6
LLW	plastic, pipework	1.57×10^6	26
VLLW	Concrete and brickwork	4.58×10^6	2×10^{-3}

Table 1.1: Expected nuclear waste accumulated by 2125.

The highest quantity of nuclear waste is predicted to be LLW or VLLW. HLW presents the lowest amount of the total waste, however it has the highest activity. During the decommissioning stage it is crucial to identify the correct type of waste under inspection and to establish the sources, their location and their quantity. One of the main reasons to develop the system proposed in this PhD is to undertake this task and be able to function up to a very high count rate, allowing fingerprinting of large amounts of highly active isotopes. In addition, the system is aimed to be lightweight so it can be mounted on a drone and be used in aerial surveys. The system proposed can also be employed in any situation where a fast identification and reconstruction of radioactive sources is required (such as after a nuclear disaster).

This PhD thesis is divided into six chapters and organised as follows. Chapter 2 describes the interaction between radiation and matter. In particular it describes the interaction mechanisms between matter and heavy charged particles, electrons and positrons, and photons. Interactions between photons and matter are the most important for this project. Chapter 3 gives an overview of the operational principles of semiconductor detectors. In chapter 4 the multi-threshold detection system developed in this work is introduced. The validity of the concept is proved and its expected performance is investigated through a Monte Carlo simulation study. Is is shown how the novel threshold technique allows to identify radioisotopes and their activities. An overview of the real system is given in 4.8, as well as some experimental work about muon tomography in the first year of my PhD. The flexibility of the system developed here (based on lightweight semiconductors and a multi-threshold method) allow for many useful applications. In particular,

the combined use of this system with an UAV (Unmanned Air Vehicle) might enable the realisation of a relatively low cost, flying detection system, that can be operated to scan hostile radiation sites (for example Fukushima) or sites in decommissioning. This would allow operators to fly the detectors with no risk to their health, crucially enhancing the safety protocols. Future applications, based on this concept, are briefly described in chapter 6. Finally, conclusions are given.

Chapter 2 | Interaction of Radiation with Matter

This chapter is devoted to the description of the interaction of radiation with matter. The chapter is focused on the description of the main nuclear processes as well as the different interaction mechanisms between radiation and matter, with particular emphasis on particles and photon interaction processes.

2.1 Generation of Radiation

Radiation can be generated by different sources such as: natural radioactivity, cosmic rays, radioisotopes used in nuclear medicine, produced in accelerators or in nuclear power plants after fission of nuclear material.

Radioactive decay occurs when a nucleus changes to a different nucleus (daughter) or to the same nucleus but with a lower energy. In nuclear decays the emitted radiation can be electromagnetic (x-rays, γ-rays) or corpuscular, such as α or β particles, internal conversion electrons, Auger electrons, neutrons, protons and fission fragments ([8]). A single radioactive source may emit different types of radiation at the same time. This emission generates a specific energy spectrum, which provides information about the nuclear processes that are taking place and isotopes present. Each radioactive source has a different decay chain which goes from an excited state, through several different steps, to the ground stable level. For example Figure 2.1 shows the decay scheme for ^{60}Co, which is one of the most common radioactive sources, in which two beta decays occur with different probabilities. With lower probability, 0.12% a 1.48 MeV β might be emitted followed by a 1.332 MeV photon. The majority of β decays, with a branching ratio of 99.88%, results in the emission of a β with an energy of 0.31 MeV followed

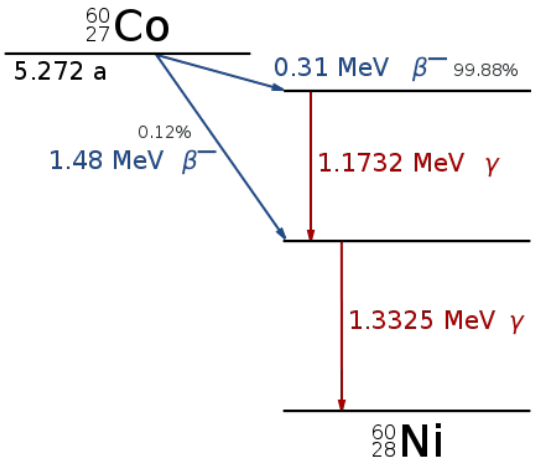

Figure 2.1: Decay level diagram for ^{60}Co [8].

by the emission of two gammas (1.1732 MeV and 1.3325 MeV) to reach the ground state of ^{60}Ni. These two gammas are emitted in cascade: the first decay happened and the atoms moves n an excited state, to reach its ground state a second photon must be emitted after the first one.

The gammas emitted during the de-excitation of the state are unique for ^{60}Co and can be considered the source fingerprint. By detecting the two emitted photons, one might be able to identify the source of the emission. Hence, this is a key concept behind the developed device.

2.2 Nuclear decay mechanisms

Nuclei are bound structures consisting of neutrons and protons. They can stay together due to the an average attractive force. The binding energy of a nucleus containing Z protons and N neutrons can be written as [9]

$$B = (Zm_p + Nm_n - m_N)c^2 \tag{2.1}$$

where m_N is the mass of the nucleus and c the sped of light. The binding energy is in the order of MeV. In figure 2.2 the binding energy as a function of A number is shown, where A is the total number of nucleons in nucleus. Up to A=58 the

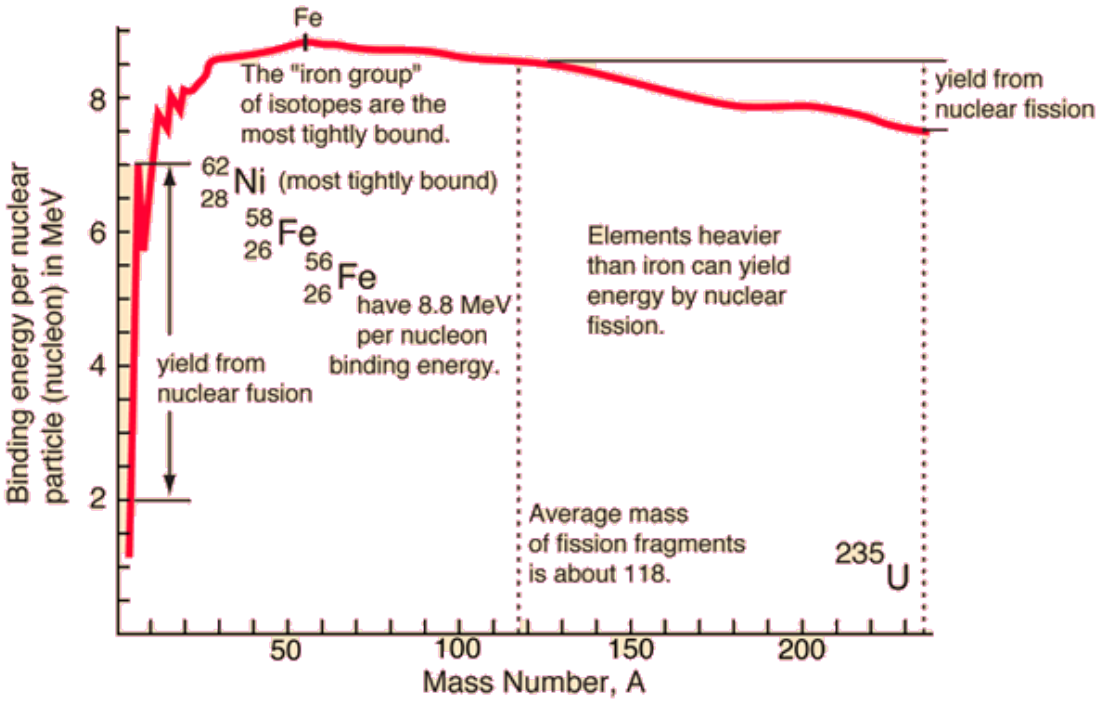

Figure 2.2: Binding energy per nucleon as function of the number mass A [10].

binding energy per nucleon increases, reaching its maximum. From this point the binding energy per nucleon decreases and the nuclei become more unstable. Smaller nuclei, $2<A<20$ can fuse, releasing energy, to yield larger and more stable nuclei. Large nuclei, $A>120$, can break apart into smaller nuclei. In this fission process smaller nuclei are produced. As shown in figure 2.3 many nuclei have been observed but only very few are stable. The unstable will decay. In nuclear decays, radiation may be emitted in several ways. The most common emitted forms of radiation are α, β and γ.

α decay corresponds to the emission of a ^4He nucleus, a bound state of 2 protons and 2 neutrons. As such α particles carry a double positive charge. They are emitted as decay products by radionuclides with atomic number Z greater than $\sim$60. The kinetic energy of emitted α's ranges up to approximately 9 MeV.

The interaction of α particles with matter occurs within few centimetres of the material. The high mass and charge of α particles, compared to electrons, gives it greater ionisation power and results in poorer penetration power. Figure 2.4 shows the range of α particles in air is shown as a function of their kinetic energy.

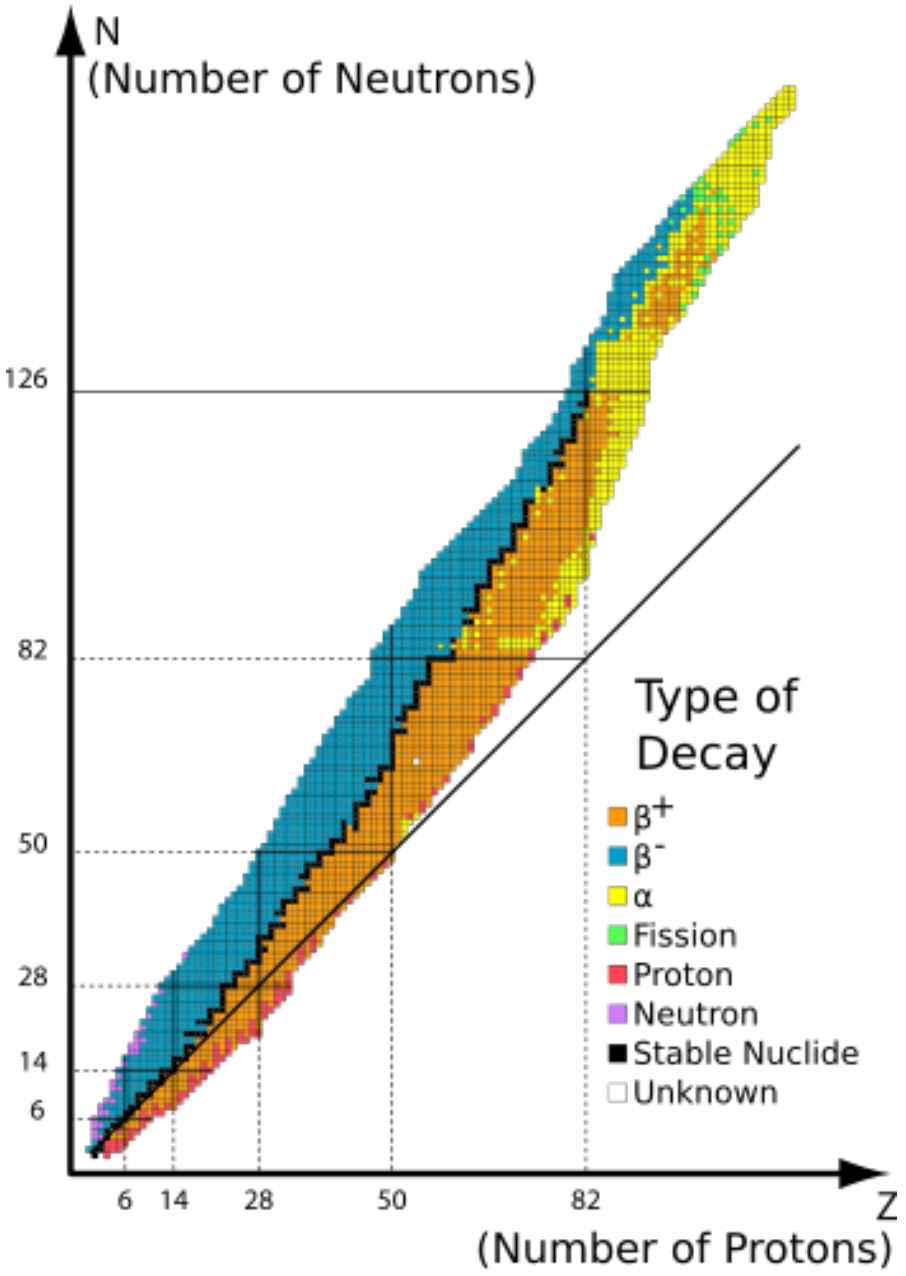

Figure 2.3: Chart of observed nuclei. The colour indicates their type of decay [11].

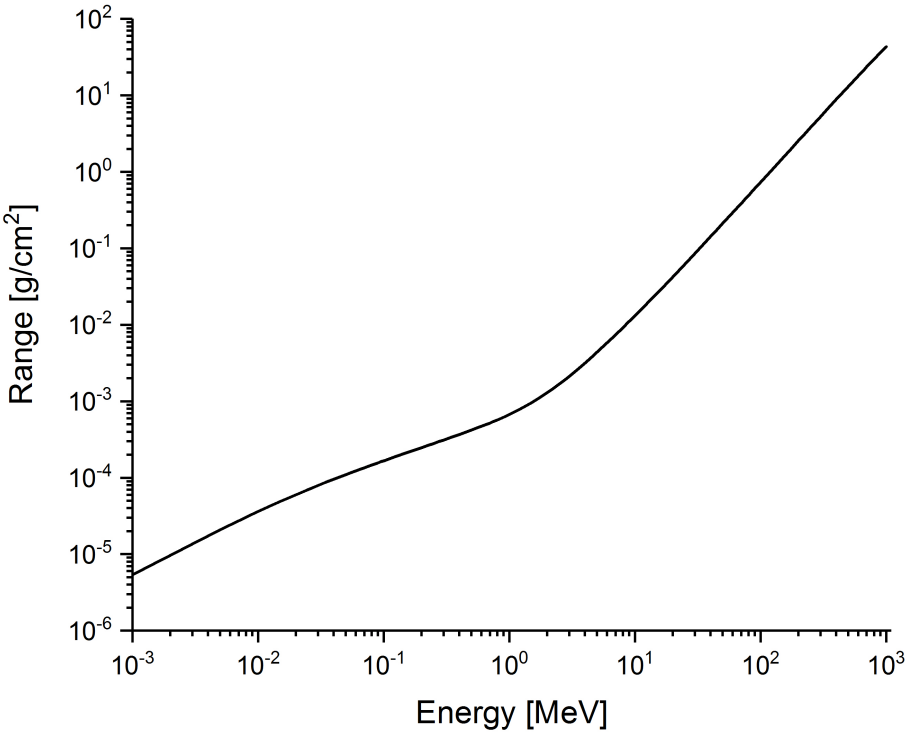

Figure 2.4: Range of α particles in dry air at sea level as a function of their kinetic energy [13].

The range is given in g/cm^2. The density of the air is typically around ρ=0.0012 g/cm^3 at sea level at 20°. For example, a 5.5 MeV α particle emitted by ^{241}Am has a range of approximately 4 cm in dry air, but only 24 μm in aluminium [12]. α particles deposit energy in matter according to the Bethe-Bloch formula, which will be explained in detail in section 2.3. The deposited energy depends on the penetration depth according to the Bragg curve, as shown in figure 2.5. α particles are easy to detect, but, due to their short range, detectors need to be placed very close to the source.

Beta decay is a manifestation of the weak decay whereby a proton is converted into a neutron or viceversa. The emitted W decay is semi-leptonic, leading to the emission of β's for ^{210}Bi decay. In β decay the mass number remains the same but the atomic number (Z) changes. The β energy range varies from 10 keV up to a few MeV as this is a three-body decay. The energy of the β exhibits a continuous energy spectrum [14]. Figure 2.6 shows the energy spectrum of β^+ and

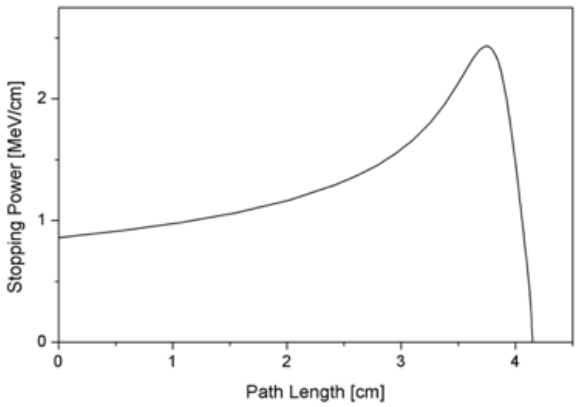

Figure 2.5: Stopping power of 5 MeV α particle in the air as function of the path lenght [12].

β^- particles. Since the interaction cross section of (anti)neutrinos with practical detector systems at the relevant energy scale is extremely low, these can be safely ignored. The range of β particle is higher than for α particles, as shown in figure 2.7. In air the range for a 5 MeV β is approximately 20 m, more than 2 orders of magnitude more compared to α's of equivalente energy. In many β sources the daughter nucleus is in an excited state. In general, excited states decay by emission of γ's. The energy of the emitted photons can vary from keV to MeV. The photon spectrum shows specific lines which can be identify as nucleus signature, making them the ideal choice for the realisation of radioactive source identification systems. The range of γ's varies a lot with their energy and with the material that they are travelling in. More details are given in section 2.4.

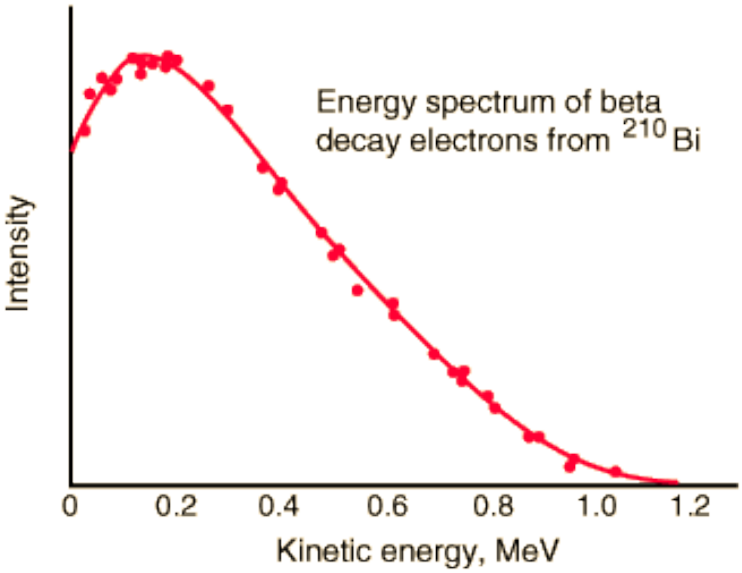

Figure 2.6: The typical β spectrum for a ^{210}Bi emitting source [15, 16].

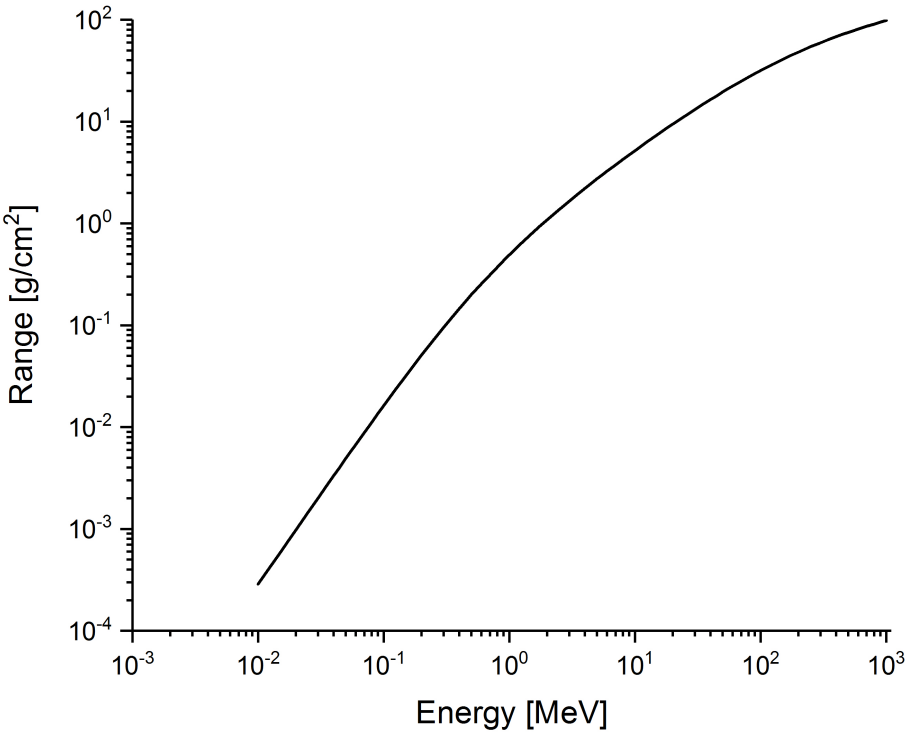

Figure 2.7: Range of β particle in dry air at sea level [17].

2.3 Charged Particle Interactions with Matter

Charged particles, such as α's, muons and electrons, interact with matter mainly via two electromagnetic processes: inelastic collisions with the atomic electrons, which in turn produces excitation and ionisation, and elastic scattering from nuclei. The total results of these interactions generates two effects: loss of energy by the particle and a deflection from its original direction. In some collisions so much energy is transferred to an electron that it gathers enough energy to travel itself through the material and ionise more material. This is known as a δ-ray. Heavy charged particles such as α's behave differently than light particles like electrons and positrons. In both cases, however, the deposited energy per unit length (stopping power) can be calculated.

The energy loss by charged particles is described by the Bethe-Block formula. Considering the classical case, the Bethe-Bloch formula can be simplified to Bohr's calculation. The full Bethe-Bloch takes into account the quantum mechanics effect.

Consider a heavy particle with mass M and charge ze crossing material and a free electron located at a distance b (impact parameter) from the particle trajectory, as shown in figure 2.8. We make the approximation that after the collision the heavy particle is undeviated ($M \gg m_e$) from its trajectory. The incident particle has a velocity v and the electron in the absorber is taken to be free and stationary, assuming the velocity of particle passing through matter is higher than the average speed of the atom's electrons. The particle applies a force $\overrightarrow{F(t)}$ on the electron at each moment. This force can be decomposed into two different components: longitudinal $F_{\parallel}$ and transverse $F_{\perp}$. The longitudinal component of the transferred momentum is 0, due to the symmetry of the problem. The impulse is given by the integral over time of the force acting at each moment [14]:

$$I = \int F \perp dt = e \int \mathcal{E}_{\perp} dt = e \int \mathcal{E}_{\perp} \frac{dt}{dx} dx = e \int \mathcal{E}_{\perp} \frac{dx}{v} \tag{2.2}$$

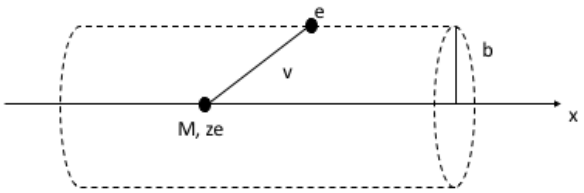

Figure 2.8: Sketch of the collision of an heavy charged particle with an atomic electron.

where v is the heavy particle velocity passing through the matter and $\mathcal{E}_\perp$ is the electric field perpendicular to the particle path, the force is equal to the charge of the electron multiplied by the electric field, which is the acting force. The electric field at the location of the electron, can be calculated using Gauss's Law. As shown in figure 2.8, the geometry of a heavy particle passing trough matter can be schematise as a infinite wire, indeed the heavy particle does not modify its path and charge while crossing the matter. The direction of the travelling is x and the radius of the cylinder created during the passage of the heavy particle in the matter is the position of an atomic electron considered b. The Gauss's Law for a wire can be written as $\oint \mathbf{E} \cdot d\mathbf{A} = 4\pi Q$, where $Q = ze$ is the total charge. $d\mathbf{A}$ is the total cylinder area and can be divided in three different part: the area of the basis S_b and the area of the later surface $2\pi b dx$. The integral can be also divided in three parts related to each area. The electric field $\mathbf{E}$ can be than considered as a sum of two components: $\mathcal{E}_\perp$ and $\mathcal{E}_\parallel$. The longitudinal component is equal to 0 due to the geometry of the system.

Applying Gauss law to the cylinder with a radius b, yields:

$$\int \mathcal{E}_{\perp} 2\pi b dx = 4\pi z e \tag{2.3}$$

and consequently

$$\int \mathcal{E}_{\perp} dx = \frac{2ze}{b} \tag{2.4}$$

Then the impulse can be written as

$$I = \frac{2ze^2}{bv} \tag{2.5}$$

and the acquired energy E by the electron as

$$\Delta E(b) = \frac{I^2}{2m_e} = \frac{2z^2e^4}{m_e v^2 b^2} \tag{2.6}$$

Let N_e be the density of the electrons, then the energy transferred by the heavy particle to the electrons located between b and $b + db$ over a length dx is

$$-dE(b) = \Delta E(b) N_e dV = \frac{4\pi z^2 e^4}{m_e v^2} N_e \frac{db}{b} dx \tag{2.7}$$

where $dV = 2\pi b db dx$ and N_e is the density of electrons. This must be integrated to give the total energy loss. If the integral is considered between 0 and ∞ it diverges. If $b \to 0$ the electron is on the particle trajectory and it cannot be consider in its position after the interaction due to the effect of the heavy particle hitting it; if $b \to \infty$ the energy received by the electrons is lower than the excitation energy and the assumption that the electron is free is not valid anymore. For these reasons, the integration has to be made between b_{min} and b_{max}, to take account all of the electrons that can be involved in the interaction. The equation 2.7 can be written, after the integration as

$$-\frac{dE}{dx} = \frac{4\pi z^2 e^4}{m_e v^2} N_e \ln \frac{b_{max}}{b_{min}} \tag{2.8}$$

We can estimate b_{min} as follows. Electrons are relativistic particles and taking this into account, the maximum transferred energy in a single head-on collision is the kinetic energy $2\gamma^2 m_e v^2$ where $\gamma = (1 - \frac{v^2}{c^2})^{-1/2}$. The energy gained by the electron expressed in equation 2.6 can match the maximum energy transferable

$$\frac{2z^2e^4}{m_e v^2 b_{min}^2} = 2\gamma^2 m v^2 \tag{2.9}$$

then b_{min}

$$b_{min} = \frac{ze^2}{\gamma m_e v^2} \tag{2.10}$$

To obtain an estimate of b_{max}, we note that the transfer energy to a bound electron circling the nucleus, must take place in a short time compared to the orbital period of the electron $\tau = 1/\bar{\nu}$

$$\frac{b}{\gamma\nu} \leq \tau \tag{2.11}$$

where $\frac{b}{\gamma\nu}$ is the interaction time, consequently

$$b_{max} = \frac{\gamma v}{\bar{\nu}} \tag{2.12}$$

Equation 2.7 can then be integrated between those two extremes and the deposited energy in dx calculated to be

$$-\frac{dE}{dx} = \frac{4\pi z^2 e^4}{m_e v^2} N_e \ln \frac{b_{max}}{b_{min}} = \frac{4\pi z^2 e^4}{m_e v^2} N_e \ln \frac{\gamma^2 m v^3}{z e^2 \bar{\nu}} \tag{2.13}$$

this is called Bohr's classical formula to determine the stopping power for a particle in matter, which works very well for heavy particles such as α. The maximum momentum transferable for a non relativistic particle is $2m_e v$, while for relativistic particles the maximum momentum takes into account the relationship between

the velocity of the particle and the speed of light: $p_e = \frac{2m_e v}{\sqrt{1-\beta^2}}$. In the direction of the particle the electric field is reduced by a factor of $1-\beta^2$, while in the transverse direction it is increased by a factor $(1-\beta^2)^{1/2}$. The energy can then be parametrised in terms of momentum transferred, which is a measurable quantity. The average energy loss per length is described by the Bethe-Bloch formula [14]:

$$-\left\langle \frac{dE}{dx} \right\rangle = 2\pi N_A r_e^2 m_e c^2 \rho \frac{z^2}{\beta^2} \frac{Z}{A} \left(\ln \frac{2m_e c^2 \gamma^2 v^2 W_{max}}{I^2} - 2\beta^2 - \delta - 2\frac{C}{Z} \right) \quad (2.14)$$

where z represents the charge of the incident particle; Z, A the atomic number and the atomic weight of the material of the absorber, respectively; m_e is the rest mass of electron, r_e is the classical electron radius, N_A is the Avogadro number, I represents the mean excitation potential, ρ is the density of the material, W_{max} is the maximum energy transfer in a single collision, γ is the Lorentz factor $\frac{1}{\sqrt{1-\beta^2}}$, δ is the density correction which is relevant at relatively high energy and C is the shell correction which is relevant at relatively low energies [14]. The maximum energy transfer is generated by a head or knock on collision and can be defined as $W_{max} \simeq 2m_e c^2 \beta^2 \gamma^2$ when $M \gg m_e$. I is defined as Planck's constant times the average orbital frequency $\bar{\nu}$ $h\bar{\nu}$. It can also be explained as the logarithmic average of the frequency weighted on the oscillation strengths of the harmonic oscillator related to the atomic levels, due to this reason I depends on the atomic shells. There are two more corrections on the Bethe-Bloch related to the shell and the density of the material. The shell correction C is relevant at relatively low energy when the assumption that the electron is stationary compare to the incident particle is not valid anymore. In this condition the velocity of incident particle and the orbital velocity of the electron are comparable and the Bethe-Bloch needs the shell correction to take into accounts these effects. At relatively high energy the shell correction δ must be considered. When a particle interact with matter its electric field tends to polarize the atoms around the particle path, while the

atoms far from the path are not influenced by particle's electric field. Due to this the collision with outer electron will contribute less to the total energy deposited. The effect of the polarization depends on the density of the material, indeed in denser material the polarization will be higher compare to less dense material.

The Bethe-Bloch formula describes the rate of energy loss in the range of approximately 0.1 $<\beta\gamma<$100 and is valid for single element absorbers. Figure 2.9 shows the stopping power or energy loss per unit length, for positive muons in Copper as a function of the muons momentum. At relatively low energies the dominant term of Eq. 2.14 is $\frac{1}{\beta^2}$: the stopping power decreases rapidly with increasing muon momentum, and a minimum value is reached approximately for $\beta\gamma \simeq$ 3-3.5; particles at this point are called minimum ionising particles (MIP). At higher energies the logarithmic rise occurs and a plateau is reached. As shown in figure 2.9 at aprroximately 50 GeV, the muon momentum starts increasing again.

Muons are much heavier than electrons, hence the assumption made to derive equation 2.14 that the projectile is much heavier is satisfied. However, when considering β's the mass of the projectile is comparable to the mass of the atomic electron. Therefore the effect of the emission of electromagnetic radiation originating from the scattering in the electric field of the nucleus (called bremsstrahlung) needs to be taken into account as well. The total energy loss $\left(\frac{dE}{dx}\right)_{tot}$ for incoming positrons and electrons is given by[14]:

$$\left(\frac{dE}{dx}\right)_{tot} = \left(\frac{dE}{dx}\right)_{coll} + \left(\frac{dE}{dx}\right)_{rad} \tag{2.15}$$

where $\left(\frac{dE}{dx}\right)_{coll}$ is the energy loss by collisions and $\left(\frac{dE}{dx}\right)_{rad}$ the energy loss by radiative stopping [19]. The energy loss by collisions $\left(\frac{dE}{dx}\right)_{coll}$ is described by a modified Bethe-Bloch equation 2.14, taking into account the lower electron mass

$$-\left(\frac{dE}{dx}\right)_{coll} = 2\pi N_a r_e^2 m_e c^2 \rho \frac{Z}{A}\frac{1}{\beta^2}\left[\ln\frac{\tau^2(\tau+2)}{2(I/m_e c^2)^2} + F(\tau) - \delta - 2\frac{C}{Z}\right] \tag{2.16}$$

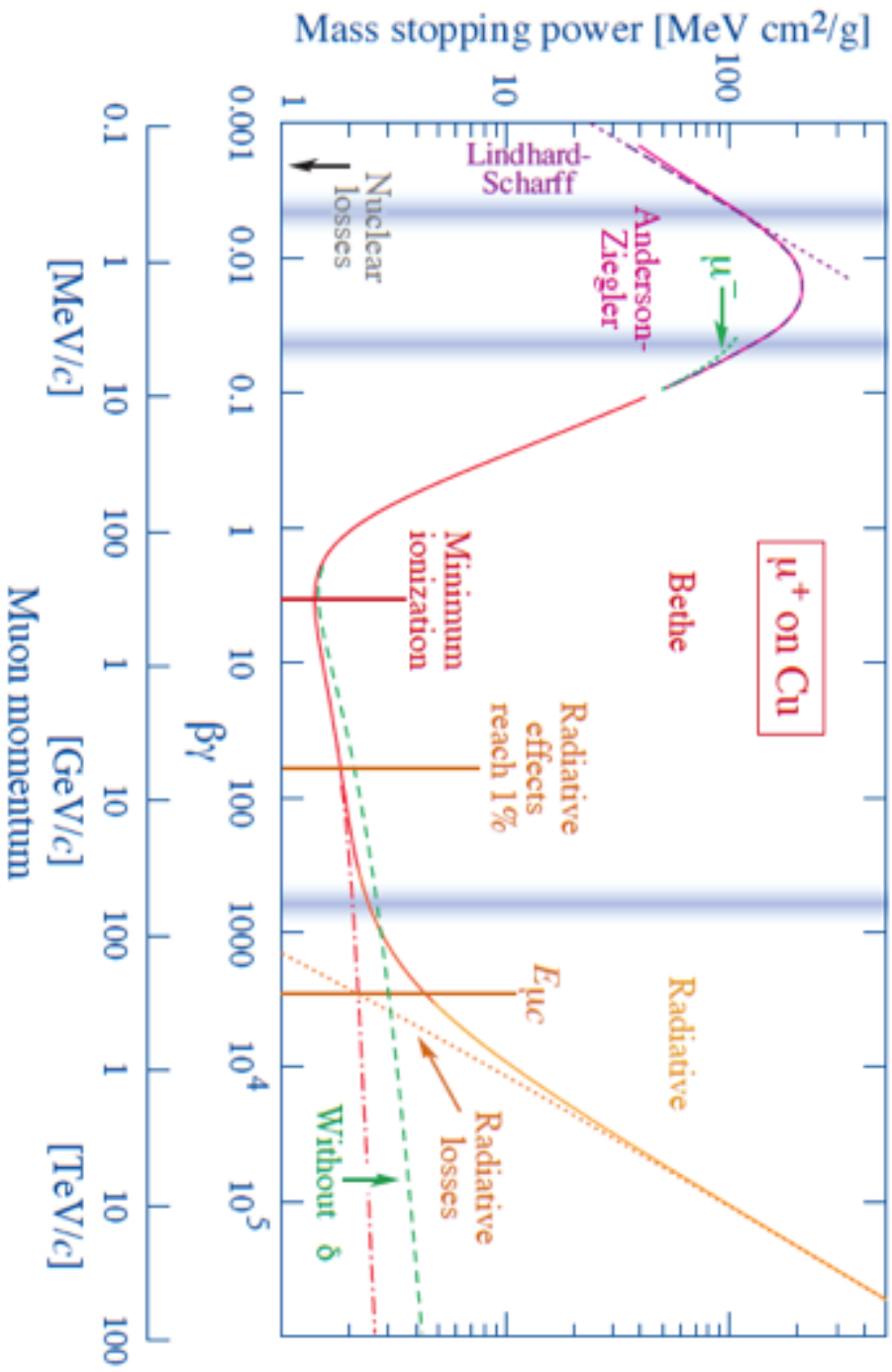

Figure 2.9: Energy lost by muons through a Cu layer [18].

where τ is the kinetic energy of the particle and $F(\tau)$ is defined as:

$$\begin{aligned} F(\tau) &= 1 - \beta^2 + \frac{\frac{\tau^2}{8} - (2r+1)\ln 2}{(\tau+1)^2} \quad \text{for } e^- \\ F(\tau) &= 2\ln 2 - \frac{\beta^2}{12}\left(23 + \frac{14}{\tau+2} + \frac{10}{(\tau+2)^2} + \frac{4}{(\tau+2)^3}\right) \quad \text{for } e^+ \end{aligned} \tag{2.17}$$

The second part of the total energy loss in the matter is given by the energy loss by radiation [19].

The electrons, while passing through matter, are effected by the electric field. The screening from the atomic electrons to the electric field generated by the nucleus has an effect on the cross section. The screening parameter is related to the screening radius of the Thomas-Fermi model of atoms r_{TF} [20–22]. The screening effect is parametrised as

$$\xi = \frac{100 m_e c^2 h\nu}{E_0 E Z^{1/3}} \tag{2.18}$$

where $h\nu$ is the energy of the emitted photon, E_0 is the initial energy of the particle passing through the matter and E its final energy. The screening parameter is approximately equal to the ratio between $r_{TF} \approx 137 Z^{1/3}\lambda_0$ and the highest possible value of the impact parameter $b_{max} = \lambda_0 E E_0 / mc^2 h\nu$, where λ_0 is the Compton wavelength [23]. If $\xi \simeq 0$ the screening is complete and if $\xi \gg 0$ the screening is absent.

The energy loss by radiation can be evaluated considering the cross section for energies greater than few MeV [14]:

$$d\sigma = 4Z^2 r_e^2 \alpha \frac{d\nu}{\nu}\left\{(1+\epsilon^2)\left[\frac{\phi_1(\xi)}{4} - \frac{1}{3}\ln Z - f(Z)\right] - \frac{2}{3}\epsilon\left[\frac{\phi_2(\xi)}{4} - \frac{1}{3}\ln(Z) - f(Z)\right]\right\} \tag{2.19}$$

where $\phi_{1-2}(\xi)$ are the screening functions calculated with empirical formulae valid for $Z \geq 5$, α is 1/137 and $\epsilon = E/E_0$. $f(Z)$ is a correction of Born approximation taking into account the Coulomb interaction between electron and nuclei.

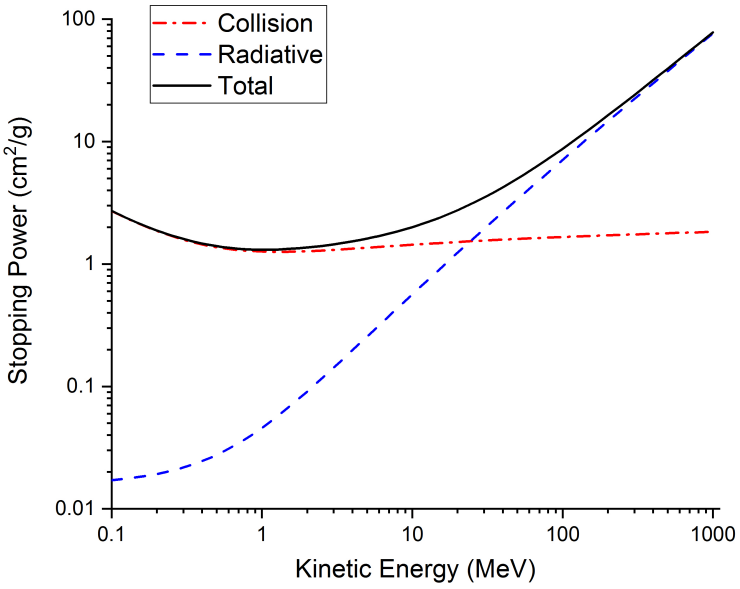

Figure 2.10: Radiation and collision contribution to the energy loss by electrons in copper [18].

Integrating the cross section the energy loss by radiation can be evaluated as:

$$-\left(\frac{dE}{dx}\right)_{rad} = N\int_0^{\nu_0} h\nu\frac{d\sigma}{d\nu}(E_0,\nu)d\nu = NE_0\Phi_{rad} \tag{2.20}$$

where $\Phi_{rad} = \frac{1}{E_0}\int h\nu\frac{d\sigma}{d\nu}(E_0,\nu)d\nu$, $\nu_0 = E_0/h$ and N the number of atoms/cm^3. The integral is approximately independent of ν, indeed $d\sigma/d\nu \approx \nu^{-1}$. The integration provides the value of Φ_{rad}

$$\begin{aligned}\Phi_{rad} &= 4Z^2r_e^2\alpha\left(\ln\tfrac{2E_0}{m_ec^2} - \tfrac{1}{3} - f(Z)\right) \qquad \text{for no screening}\\ \Phi_{rad} &= 4Z^2r_e^2\alpha\left[\ln(183Z^{-1/3}) + \tfrac{1}{18} - f(Z)\right]\end{aligned} \tag{2.21}$$

As shown in figure 2.10, here is a specific energy in which $\left(\frac{dE}{dx}\right)_{rad} = \left(\frac{dE}{dx}\right)_{coll}$. This called critical energy and is given by $E_c = \frac{800}{Z+1.2}$, after this point radiation effect begins to dominate.

2.3.1 Interaction of matter in compound material

The Bethe-Bloch expressed in the previous equation 2.14 is valid only for material comprising a single element. For compounds, the Bethe-Bloch formula has to be modified by taking into account the different material amounts and properties. The energy loss can be calculated as the weighted average of the energy loss in each single element in the compound under consideration. Using Bragg's rule for compounds the mass stopping power can be calculated as [14]:

$$\frac{1}{\rho}\frac{dE}{dx} = \frac{w_1}{\rho_1}\left(\frac{dE}{dx}\right)_1 + \frac{w_2}{\rho_2}\left(\frac{dE}{dx}\right)_2 + \dots \tag{2.22}$$

where $w_i = \frac{a_i A_i}{A_m}$ is the fraction by weight of the element, A_i is the atomic weight of the element, a_i the number of atoms of the i element, $A_m = \Sigma a_i A_i$ and ρ the density of element.

2.3.2 Landau distribution

A particle beam consists of several particles which interact with matter. Since the interaction with the material is a stochastic process, the energy deposited for a single particle can vary from the mean described by the Bethe-Bloch equation, equation 2.14. The energy loss is essentially Gaussian distributed. However, in some interactions a lot more energy is transferred by the projectile to an electron. In that case the electron might receive enough kinetic energy to move through the material and deposit more energy. These are known as δ electrons. This leads to a tail in the energy loss distribution towards higher energy loss. This distribution is known as a Landau distribution [14, 24]. The tails are particularly clear for a thin absorber while due to the central limit theorem, the energy loss in a thick absorbers is almost Gaussian. This is illustrated in figure 2.11 where the measured Landau distributions for several thicknesses of silicon are shown, normalised to the thickness.

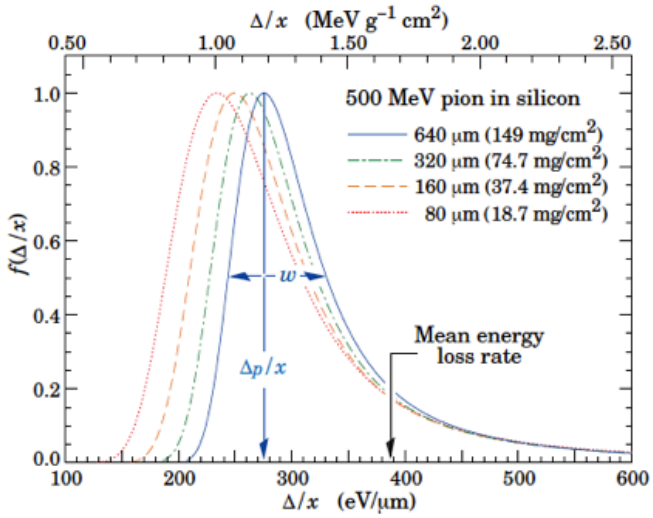

Figure 2.11: Landau distribution in Silicon for 500 MeV pions for different detector thicknesses [18].

2.4 Interaction of photons with matter

As explained in section 2.2, the most useful particles to identify sources are γ's. Their interaction with matter is completely different compared to charged particles due to the fact that they do not have a charge. Photons interact with the matter according to three processes: the photoelectric effect, Compton scattering and pair production [14, 18, 24]. These processes have cross-sections that depend on the energy of the photon beams. In the next section all the processes are explained in detail.

2.4.1 Photoelectric effect

The photoelectric effect describes the emission of electrons (called photo-electrons) when an incident photon is absorbed by a material [14]. The kinetic energy of the photo-electron is given by Einstein's equation:

$$E = h\nu - B.E. \tag{2.23}$$

where $B.E.$ represents the binding energy and $h\nu$ is the energy of the incoming photon. The photo-electron can be ejected from different shells depending on the energy of the incident photon. The atom may release further electrons (Auger effect) or the vacancy might be filled by electrons from higher orbits, releasing X-rays.

The cross section of the photo electric effect $\sigma_{p.e.}$ can be calculated in the Born approximation as:

$$\sigma_{p.e.} = 4\alpha^4\sqrt{2}Z^5\phi_0\left(\frac{m_e c^2}{h\nu}\right)^{7/2} \tag{2.24}$$

where $\phi_0 = 8\pi r_e^2/3 = 6.651 \times 10^{-25} cm^2$. The photoelectric cross section strongly depends on the atomic number Z and it is proportional to Z^5.

Figure 2.12 shows the photoelectric cross section $\sigma_{p.e.}$ as a function of the photon energy in lead. Photons can be absorbed by the electrons with different shell energies. This results in sharp absorption edges located at each ionisation threshold energy occurring at the shell binding energies. Subsequently, rapid decreases in probability occur when the specific shell electrons are not available any more [25].

Equation 2.24 only describes the trend line of the cross section as a function of the photon energy and not the spikes due to the shells. The photoelectric cross section is proportional to Z^5 and is also strongly dependent on the energy of the incident photons. The strong dependence on the Z of the material is exploited in our detector design.

2.4.2 Compton scattering

Compton scattering describes the scattering of a photon on a free electron, which can be considered free if the energy of the photon is higher than the binding energy. The process is illustrated in figure 2.13, the incident photon interacts with the electron, in the interaction energy is transferred from the photon to the electron and the photon is scattered by its original trajectory over an angle θ. The recoil electron is emitted at an angle ϕ. Applying the conservation laws for energy and momentum θ and ϕ can be related as

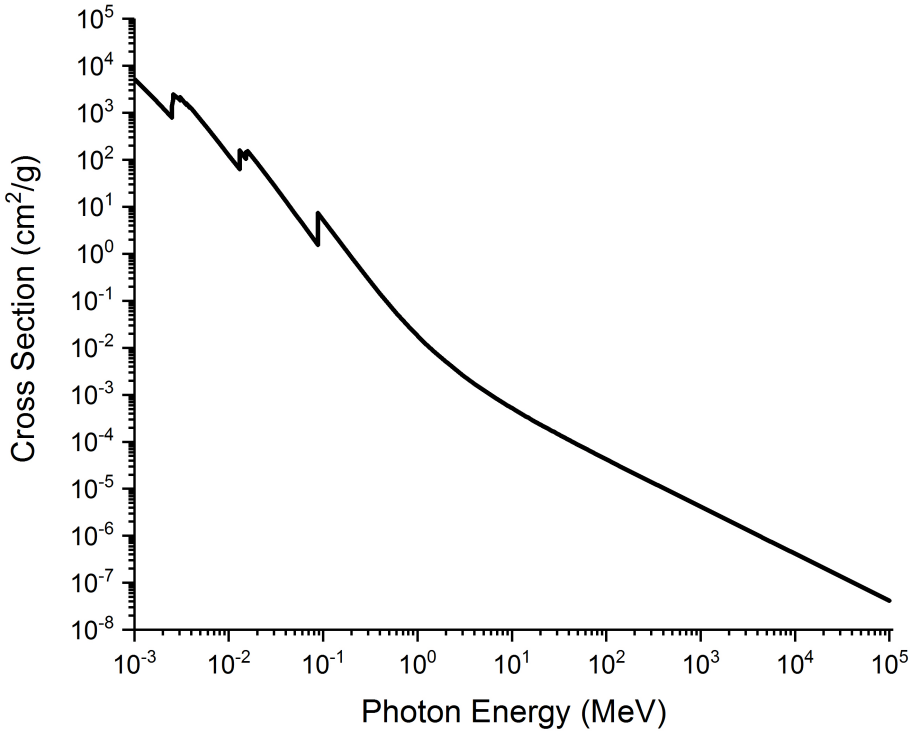

Figure 2.12: The cross section for the photoelectric effect in lead as a function of the photon energy. The cross section is obtained from [26].

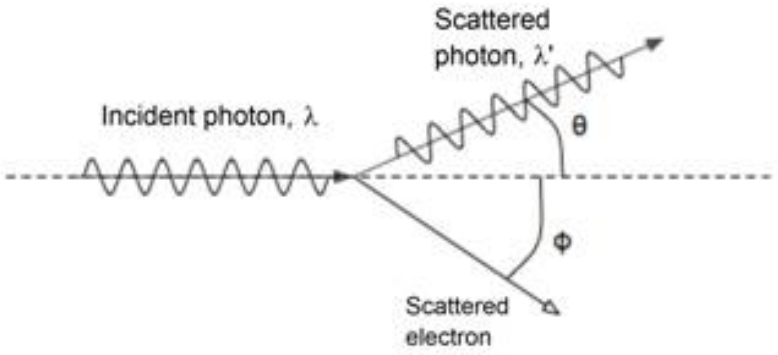

Figure 2.13: Sketch of Compton interaction. The incident photon interact with an electron which is consequently scattered with an angle ϕ.

$$\begin{aligned} \cos\theta &= 1 - \frac{2}{(1+\gamma)^2 \tan^2\phi + 1} \\ \lambda - \lambda' &= \frac{h}{m_e c}(1 - \cos\theta) \end{aligned} \tag{2.25}$$

The differential cross section $\frac{d\sigma_c ompton}{d\Omega}$ can be obtained using the Klein-Nishina formula [14]:

$$\frac{d\sigma_c ompton}{d\Omega} = Z\frac{1}{2}r_0^2 \left\{ \frac{1}{[1+\gamma(1-\cos\theta)]^2} \left[1 + \cos^2\theta + \frac{\gamma^2(1-\cos\theta)^2}{[1+\gamma(1-\cos\theta)]} \right] \right\} \tag{2.26}$$

where r_0 is the classical electron radius. Integrating this equation over $d\Omega$ the cross section for Compton scattering is obtained

$$\sigma_{compton} = 2\pi r_e^2 Z \left\{ \frac{1+\gamma}{\gamma^2} \left[\frac{2(1+\gamma)}{1+2\gamma} - \frac{1}{\gamma}\ln(1+2\gamma) \right] + \frac{1}{2\gamma}\ln(1+2\gamma) - \frac{1+3\gamma}{(1+2\gamma)^2} \right\} \tag{2.27}$$

The Compton cross section is proportional to Z of the material. Compare to the photoelectric effect, where the dependence was Z^5, the relation is weaker. In figure 2.14 the Compton cross section is shown as a function of the photon energy in lead. For low energy the cross section has its initial point, while with the increasing in

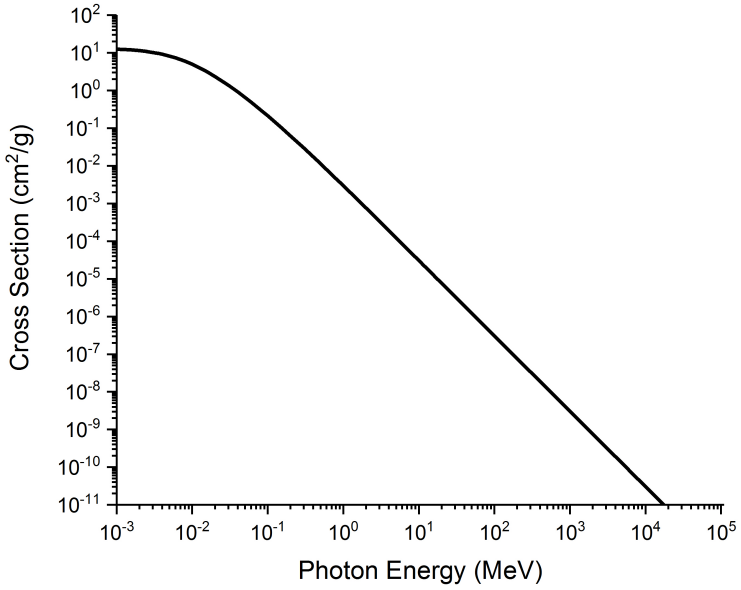

Figure 2.14: Compton cross section in lead.

energy it starts to drop down, up to when the Compton contribution is irrelevant, compare to other energy loss mechanism, for high energy photons.

The energy of the recoil electron has a maximum, which is results in a maximum deposited energy in an absorber.

The maximum transferred energy occurs when the photon is scattered back in the direction it came from, i.e. a scattering over 180°. The recoil electron will then have an energy of [14]:

$$T_{max} = h\nu \frac{2\gamma}{1 + 2\gamma} \tag{2.28}$$

This is know as the Compton edge [14]. The energy of the recoil electron is smaller for smaller angles. Figure 2.15 illustrates the deposited energy due to Compton scattering. The full energy peak is defined as the peak generated by the photoelectron; theoretically it is in a specific energy value represented by the energy of the emitted particle. In reality, the peak is centered at the full energy peak but it is spread around it. Compare to the well defined photopeak there is

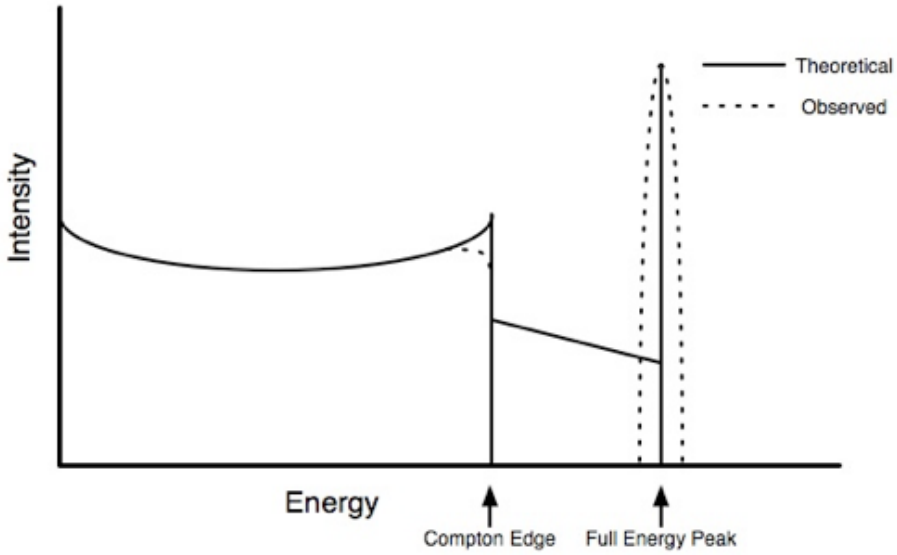

Figure 2.15: Deposited energy for Compton scattering. Two peaks are visible, the well defined photopeak at full peak energy and the spread Compton edge which covers a broad range of energies [14].

the Compton edge which is spread across different energies due to the effect of the angle of interaction.

2.4.3 Pair production

The final interaction of gammas with matter is pair production, which occurs if the energy of the photon exceeds a threshold energy level of 1.022 MeV, double the mass of the electron. Then the photon can produce an electron positron pair. The pair production only occurs if a nucleus is present to conserve momentum. As for the radiation energy loss for electrons, the screening of the atomic electrons (equation 2.18) has an effect on the cross section. Instead of the initial and final energy, in this configuration the energy of the outgoing positron E_+ and electron E_- must be considered [27].

The differential cross-section dk can be expressed, considering the Born approximation and the value of ξ, screening effect. If $\xi \gg 1$, no screening, the differential cross section is expressed by:

$$dk = 4Z^2\alpha r_e^2 dE_+ \frac{3(E_+^2 + E_-^2) + 2E_+E_-}{3(h\nu)^3}\left[\ln\frac{2E_+E_-}{h\nu m_e c^2} - \frac{1}{2} - f(Z)\right] \tag{2.29}$$

and for complete screening $\xi \to 0$:

$$dk = 4Z^2\alpha r_e^2 \frac{dE_+}{(h\nu)^3}\left\{\left(E_+^2 + E_-^2 + \frac{2E_+E_-}{3}\right)[\ln(183Z^{1/3} - f(Z)] - \frac{E_+E_-}{9}\right\} \tag{2.30}$$

The pair production cross section k after the integration of equation 2.29 and equation 2.30 is given by [14]

$$\begin{aligned} k &= 4Z^2\alpha r_e^2\left[\tfrac{7}{9}\left(\ln\tfrac{2h\nu}{m_e c^2} - f(Z)\right) - \tfrac{109}{54}\right] \quad \text{for non screening} \\ k &= 4Z^2\alpha r_e^2\left\{\tfrac{7}{9}[\ln(183Z^{-1/3}) - f(Z)] - \tfrac{1}{54}\right\} \quad \text{for complete screening} \end{aligned} \tag{2.31}$$

where $h\nu$ is the energy. The pair production cross section is proportional to Z^2.

The cross section in lead is shown as a function of the photon energy in figure 2.16. Below 1.022 MeV the cross section for pair production is zero and then it rises up. For energies higher than 1 MeV it is the dominant interaction mechanism.

In the spectrum the pair production is represented by 1 or 2 peaks at the photon energy minus 511 keV or 1022 keV or both. The two gammas emitted are due to the annihilation of the positron and the conservation of momentum.

2.4.4 Total Cross Section

To summarise the dependence of cross section to Z and E can be made explicit

$$\begin{aligned} \sigma_{p.e.} &\approx \tfrac{Z^5}{E_\gamma^{7/2}} \quad \text{when} E_\gamma > I_i \\ \sigma_{p.e.} &\approx \tfrac{Z^5}{E_\gamma} \quad \text{when} E_\gamma \gg I_i \\ \sigma_{compton} &\approx \tfrac{Z}{E_\gamma} \\ k &\approx Z^2 \ln\tfrac{E_\gamma}{m_e c^2} \end{aligned} \tag{2.32}$$

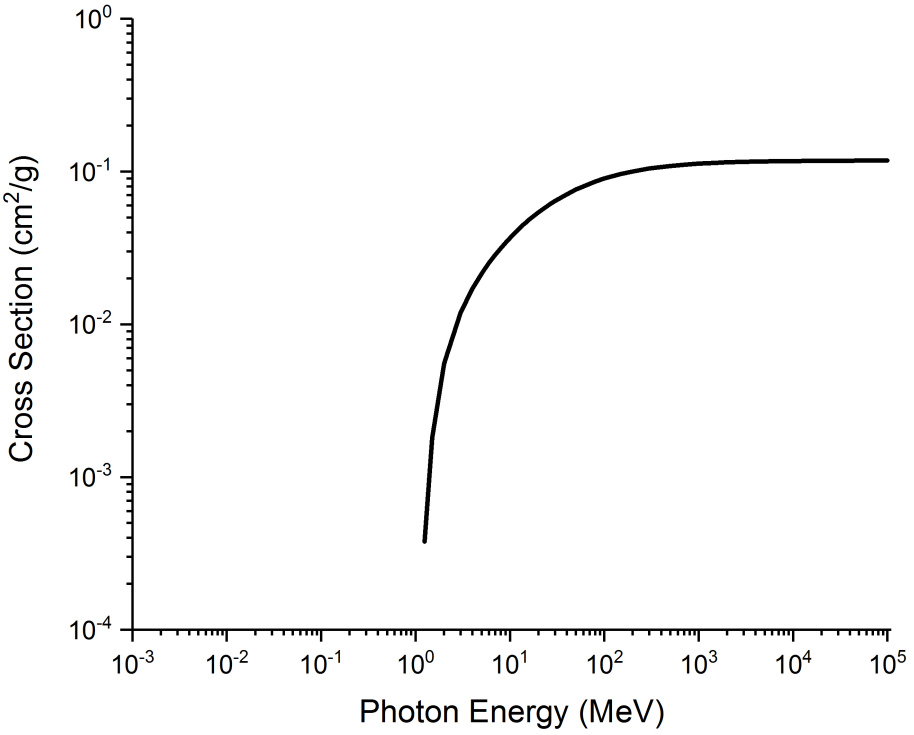

Figure 2.16: Pair production cross section in lead as a function of the photon energy.

where I_i is the ionising energy. As mentioned before, the total cross section for the interaction of photons in matter is dominated by the sum of the photoelectric effect $\sigma_{p.e.}$, Compton scattering $\sigma_{Compton}$ and pair production k. Other effects are present but their contributions are negligible:

$$\sigma_{tot} = \sigma_{p.e.} + \sigma_{Compton} + k \tag{2.33}$$

The total cross section for photon interactions strongly depends on the Z of the detector material. The total cross sections calculated for lead and carbon are shown in figure 2.17. Carbon is a relatively light element whereas lead is a relatively heavy element. At low energy the photoelectric effect is dominant for both materials, with a contribution of Compton scattering. The different absorption edges can be observed at low photon energy. There are more filled electron energy shells in lead, resulting in more edges. The Compton effect is the highest contribution for energies between approximately 0.8 MeV and 1.2 MeV for carbon, and a lower spectrum range for lead, between 1 MeV and 1.2 MeV, after that the pair production is the most probable effect and the highest cross section contribution.

The Compton cross section ($\sigma_{Compton}$) in lead is higher than in carbon, reflecting the larger number of electrons in lead. At high photon energies pair production dominates for both materials. Other effect are present with lower cross section value, such as Rayleigh related to the elastic scattering of a particle, k_{nuc} and k_e related to the effect due to the nuclear and electronic shells and $sigma_{g.d.r.}$ related to the dipole resonance.

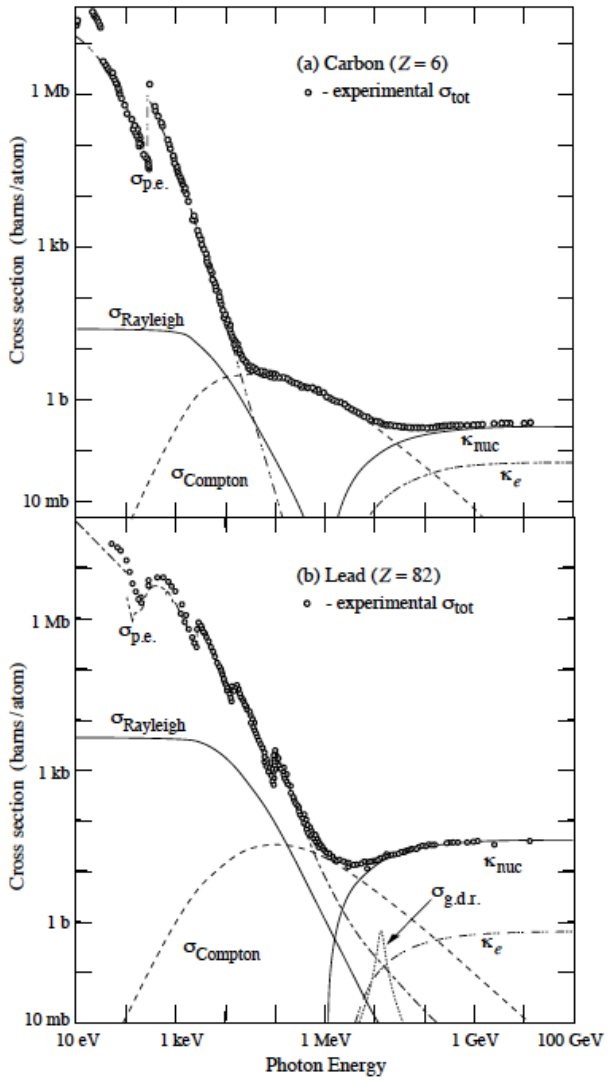

Figure 2.17: Total cross sections for lead and carbon as a function of energy. Where $\sigma_{p.e.}$ is the photoelectric effect cross section,

2.5 Summary

Nuclear decays generate α, β and γ's. α's are doubly charged, heavy particles with a very limited range before absorption. β's are electrons and positrons. They tend to travel much further than α's but their range, even in air, is still limited to $\sim$1 m. γ's, or photons, travel appreciable distances and thus can be observed at much greater distances. Furthermore, their energy is characteristic for each isotope. This makes them the key particles to detect and identify radioactive isotopes. Those three particles interact with the matter in different ways due to their charge and their mass. Photons interact with matter mainly in three different ways: the photoelectric effect, Compton scattering and pair production. The cross sections for these processes depend strongly on the photon energy and the Z of the absorber. This will be exploited in the design of the fingerprinting device.

Chapter 3

Semiconductor-based detectors

Particle detection can be done with different detector systems, for example: gaseous detectors, scintillators and solid state detectors. As discussed in section 2.4, the cross-section for the interaction of γ's with matter increases with the Z of the absorber. Hence, the best detection efficiency is obtained using detectors with high Z material. Gaseous detectors are usually filled with low Z elements making them less suitable for γ-detection. Scintillators can have high Z. They can also be produced with a large area and thickness. Compared to other detector types, solid state detectors have a low ionisation energy, i.e. a few eV compared to $\simeq$ 30 eV for gaseous detectors and 10-200 eV for scintillators. In solid-state detectors the charge carrier mobilities are faster compared to gas detectors leading to a faster response and less dead time. Due to the relatively high density of solid state detectors, they also exhibit a large stopping power, enabling them to operate as efficient detectors. Therefore, they can be made thin while still being an efficient detector. Some of them (i.e. diamond) are highly radiation tolerant, which makes them a good option for operation in a high radiation environment.

Detectors used in elementary particle and nuclear physics are based on the principle to transfer radiation energy to detector mass. Charged particles are transferring their energy through collisions to atomic electrons leading to excitation and ionisation. In most cases, neutral particles have to produce charged particles first inside the detector volume which in turn are transferring their energy by excitation or ionisation to the detector. All these interaction processes are random processes.

There is no detector which is perfectly suited for all possible applications. Depending on the application at hand detectors and complex detector systems are

designed according to several criteria. There are several characteristics specifying the features of a detector:

- *Energy resolution*: due to fluctuations in the number of excitation and ionization in the detector material, one observes a Gaussian-like peak for a monoenergetic particle beam instead of an ideal delta-function peak. The width of this peak determines the capability to distinguish particles with different energy. The energy resolution ΔE is given by the full-width-at-half-maximum (FWHM) of the signal peak. For a Gaussian distribution with standard deviation σ the FWHM is defined by

$$FWHM = 2.35\sigma \tag{3.1}$$

  energies closer than this resolution can not be separated.

  The same situation occurs for *spatial resolution* and *time resolution*;

- *Detector Efficiency*: the total efficiency (ϵ_{tot}) of a detector is defined by the fraction of events registered (N_{reg}) at the detector with respect to the number of events emitted by a radiation source ($N_{emitted}$):

$$\epsilon_{tot} = \frac{N_{reg}}{N_{emitted}} \approx \epsilon_{int} \times \epsilon_{geom} \tag{3.2}$$

  where ϵ_{int} is the *intrinsic efficiency* given by the fraction of events registered by the detector with respect to the number of events hitting the detector; the ϵ_{geom} dependes on the polar and azimuthal angle of the emitted particle and on the momentum of the particle.

This chapter provides a description of semiconductor detectors, and their operation principles.

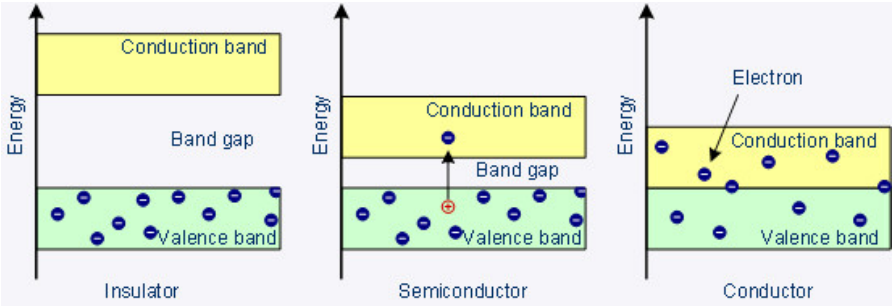

Figure 3.1: Energy band structure for semiconductor detector [28]

3.1 Semiconductor material

Solid state materials are characterised by a crystalline structure in which the electron energy shows a band structure. These bands form a valence and a conduction band, separated by an energy gap, as illustrated in figure 3.1; the band size is determined by the lattice space between the atoms which depend on temperature and pressure. Charge carriers (electrons and holes) with enough thermal energy may transition across the gap between the bands. Conductor materials do not have any band gap between the conduction and the valence band. Insulator materials have a big energy gap between the two bands which under normal circumstances prevents charge carriers to transition from one band to the other. Semiconductor materials have a small energy band gap, in the order of a few eV, which allows, under the right conditions, the transition of charge carriers between those bands. Different semiconductor materials have different energy band gap values. For example, the band gap is 1.12 eV in silicon and 5.5 eV in diamond. For comparison, the typical thermal energy of an electron at room temperature is around 0.025 eV.

In order to understand the concept underlying the operational principles of semiconductor particle detectors, a brief description and discussion on semiconductor materials is given. Semiconductors are classified as intrinsic (pure semiconductor) and extrinsic (doped with impurities). In intrinsic semiconductors free electrons and holes are generated by thermal excitation. Some of electron hole pairs produced recombine and an equilibrium concentration of electron hole pairs is achieved. An electron can recombine with a hole when a open level in the valance

band is present, then the electron drops from the conduction band and emits a photon to release the excess energy. In general, the probability that an energy state is occupied is given by [28]:

$$F(E) = \left[1 + exp\left(\frac{E - E_F}{k_B T}\right)\right]^{-1} \tag{3.3}$$

where E_F is the Fermi energy, T is the absolute temperature and k_B is Boltzmann's constant. The Fermi energy corresponds to the energy level (Fermi level) where there is the 50% of probability of an energy state to be occupied. More specifically this is the probability than an electron occupies a state in the conduction band or a hole in the valance band.

The equation 3.3 can be approximated for electrons and holes if E_F is in the band gap and at a distance larger than $3k_BT$ from the edge of both the valance and the conduction band. In an intrinsic semiconductor, E_F is approximately in the middle of the band gap. Then equation 3.3 can be simplified as

$$\begin{cases} F_e(E) \simeq exp\left(\frac{E_F - E}{k_B T}\right) & \text{electrons} \\ F_h(E) \simeq exp\left(\frac{E - E_F}{k_B T}\right) & \text{holes} \end{cases} \tag{3.4}$$

where E_F is the Fermi energy.

The density of free electrons is simply the product of the probability of occupation multiplied by the density of states available in the conduction band. The density of states N is a function of the kinetic energy E_{kin}

$$N(E_{kin}) = 4\pi \left(\frac{2m}{h^2}\right)^{3/2} E_{kin}^{1/2} \tag{3.5}$$

then by evaluating the product of the density of states and the occupation probability the density of free electrons (n) and holes (p) is obtained:

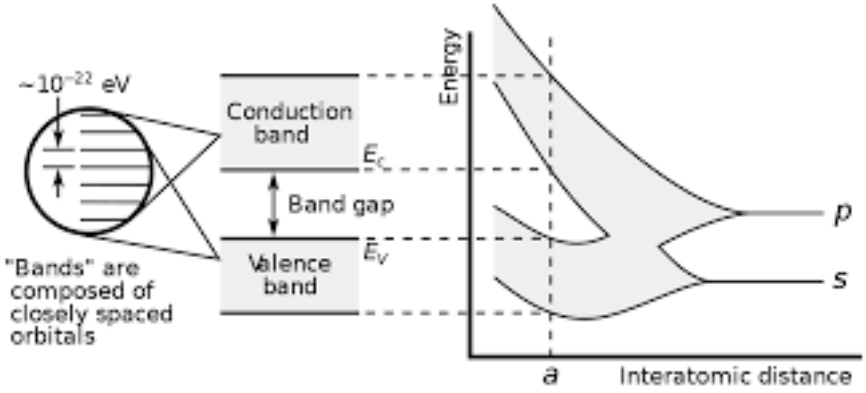

Figure 3.2: Energy band structure for semiconductor detector [28]. The orbital levels are shown to better identify the band structure correspond to each level.

$$\begin{aligned} n &= 2\left(\frac{2\pi m_n k_B T}{h^2}\right)^{\frac{3}{2}} exp\left(-\frac{E_C - E_F}{k_B T}\right) \\ p &= 2\left(\frac{2\pi m_p k_B T}{h^2}\right)^{\frac{3}{2}} exp\left(-\frac{E_F - E_V}{k_B T}\right) \end{aligned} \tag{3.6}$$

where $m_{n,p}$ is the effective mass of respectively the electron or the hole and the energy difference between the energy levels of the conduction band and the valence band is the band gap energy, E_g. E_C is the energy level of the conductive band and E_V is the energy level of the valance band. For intrinsic semiconductors $n = p$ and the product of the charge carrier concentrations is given by:

$$np = N_C N_V e^{-\frac{E_C - E_V}{kT}} \tag{3.7}$$

where N_C and N_V are the densities of the states in conduction and valence band. The product of the charge carrier concentrations is directly related to the band gap energy of the material. The higher the band gap the lower the product of the charge carrier concentrations. In intrinsic semiconductor the density of electrons or holes is:

$$n_i = \sqrt{np} \tag{3.8}$$

Equation 3.7 and 3.8 show that the number of mobile charge carriers depends strongly on the temperature and band gap. Figure 3.2 shows the band structure in a semiconductor material.

At the same temperature the mobile charge carriers concentration for diamond (E_g=5.48 eV) and germanium (E_g=0.664 eV) differ by a factor $\sim$34. As a consequence, diamond detectors can be operated without special measures at room temperature while germanium detectors are usually operated at liquid nitrogen temperature to reduce the number of thermally generated mobile charge carriers.

The charge carrier concentration can be modified by adding donor or acceptor impurities to the semiconductor. Silicon atoms in a lattice are connected to their neighbours with four covalent bonds. Introducing impurities from group V elements like Sb, P, As which have five covalent electrons provides an excess of electrons (donor), and introducing impurities from group III elements like B, Al, Ga, which have only 3 covalent electrons which provides an excess of holes (acceptor). This is illustrated in figure 3.3. The presence of the impurities creates new energetic levels, indeed the energy level is shifted towards the other band and, due to this effect, for an electron in this state jumping from a valence to a conduction band is easier. The new levels typically are so close to the bands that these states are ionised under normal circumstances. This results in an excess of mobile electrons and/or holes, which changes the material properties significantly. Materials with an excess of donor are known as n-type materials, while materials with an excess of acceptors are known as p-type.

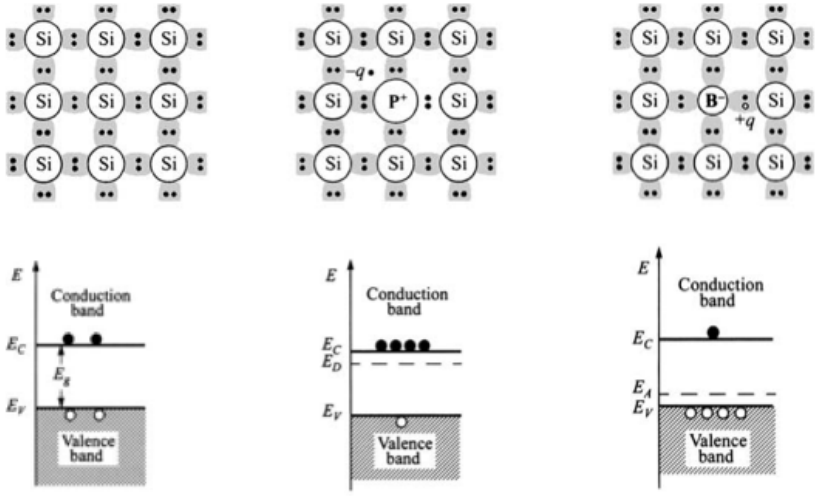

Figure 3.3: On the left of the page the intrinsic Si, in the centre doping with n material and on the right with p material [29].

3.2 p-n Junction

When n- and p-type semiconductors are brought in contact a so-called p-n junction is realised. The excess electrons on the n-side of the junction diffuse into the p-side of the junction where they will recombine with the excess holes. This lead to a depletion zone where no mobile charge carriers are present and to a built-in electric field which opposes the diffusion. This is illustrated in figure 3.4. The depletion zone is between $-x_p$ and x_n. The size of the depletion region has an important role for the radiation detection as in this region there are essentially no background charge carriers to mask the charge carriers generated by the interaction with radiation. However, a small leakage current is still present due to thermal generation of mobile charge carriers.

Initially the depletion zone generated is small and depends on the concentration impurities. The potential difference over the junction ($V(x)$) can be calculated using the Poisson equation [14] if the charge densities $\rho(x)$ are known

$$\frac{d^2V}{dx^2} = -\frac{\rho(x)}{\epsilon} \tag{3.9}$$

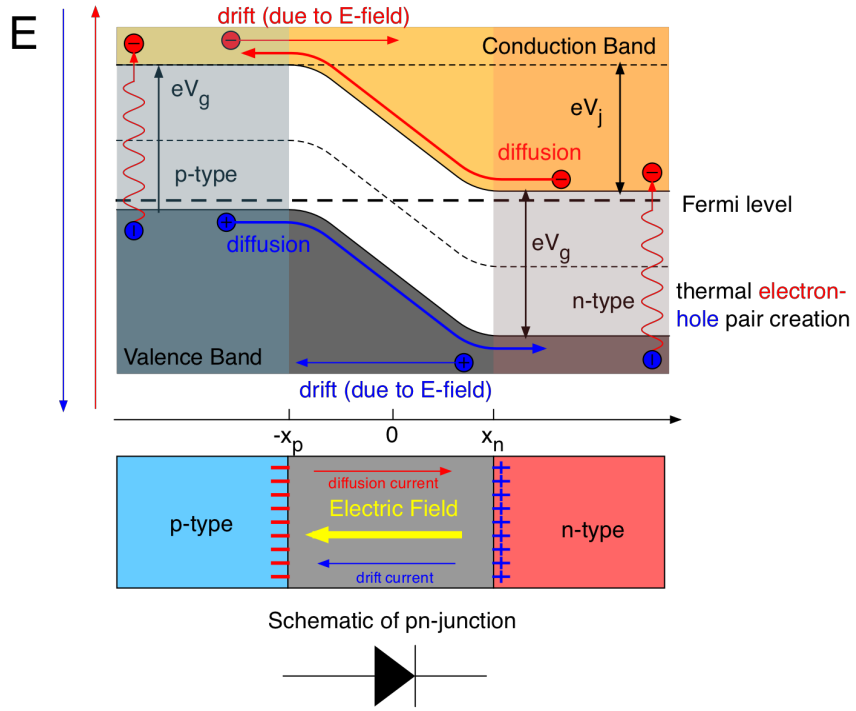

Figure 3.4: p-n junction structure.

where ϵ is the dielectric constant. Considering an abrupt junction; then

$$\rho(x) = \begin{cases} qN_D & 0 < x < x_n \\ -qN_A & -x_p < x < 0 \end{cases} \tag{3.10}$$

where N_D is the donor concentration, N_A the acceptor concentration and q the charge of electrons. Since the excess electrons diffuse into the p-type material and vice versa, charge conservation yields

$$N_A x_p = N_D x_n \tag{3.11}$$

and using the boundary condition of $\frac{dV}{dx} = 0$ at $x = x_n$ and $x = -x_p$

$$\frac{dV}{dx} = \mathcal{E} = \begin{cases} -\frac{qN_D}{\epsilon}(x - x_n) & 0 < x < x_n \\ \frac{qN_A}{\epsilon}(x + x_p) & -x_p < x < 0 \end{cases} \tag{3.12}$$

Then $V(x)$ is

$$V_(x) = \begin{cases} -\frac{qN_D}{\epsilon}\left(\frac{x^2}{2} - xx_n\right) + C & 0 < x < x_n \\ \frac{qN_A}{\epsilon}\left(\frac{x^2}{2} + xx_p\right) + C' & -x_p < x < 0 \end{cases} \tag{3.13}$$

The solution of the system of equations has to merge for x=0, so $C = C'$. Without loss of generality, the potential at $x = -x_p$ can be set to 0, then the built-in potential at the junction (V_0) is

$$V_0 = \frac{q}{2\epsilon}(N_D x_n^2 + N_A x_p^2) \tag{3.14}$$

Then x_n and x_p can be determined as

$$\begin{aligned} x_n &= \sqrt{\frac{2\epsilon V_0}{qN_D(1+N_D/N_A)}} \\ x_p &= \sqrt{\frac{2\epsilon V_0}{qN_A(1+N_A/N_D)}} \end{aligned} \tag{3.15}$$

The depletion zone width is then [14, 28, 30]

$$d = x_n + x_p = \sqrt{\frac{2\epsilon V_0(N_A + N_D)}{qN_A N_D}} \tag{3.16}$$

Equation 3.16 is valid under the assumption that the width of the depletion region is smaller than the device thickness. If an external voltage (bias voltage V_b) is applied, the depth of the depletion zone can be altered

$$d = x_n + x_p = \sqrt{\frac{2\epsilon(V_0 + V_b)(N_A + N_D)}{qN_A N_D}} \tag{3.17}$$

When applying a voltage opposing V_0, the width gets smaller. This configuration is typically referred as forward biased p-n junction. If V_b is opposite but larger in magnitude than V_0, there is no longer an electric field opposing charge transport and the resistance of the junction is minimal. When applying a voltage parallel to V_0, the width of the depletion zone becomes larger and the current flow is inhibited. This is know as a reverse biased diode. The effects on the width are shown in figure

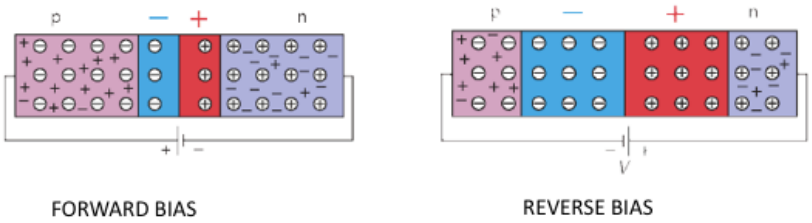

Figure 3.5: Forward and reverse bias effect on the junction.

3.5. The larger the depletion zone, the larger the area with minimal background to the charge carriers generated by the interaction with radiation.

The p-n junction current-voltage (IV) characteristic is shown in figure 3.6. As described above, when the p-n junction is forward biased the current slowly increases, until a threshold level, where $V_b = -V_0$ is reached. From that point onward the current follows a exponential growth with applied voltage. In reverse bias the barrier region increases and a very small reverse current flows through the device. With increasing voltage there is a particular value, called the breakdown voltage, beyond which the current increases rapidly. This is called junction breakdown.

Semiconductor detectors are typically operated as reverse biased diodes and hence they can be seen as two contacts with a highly resistive material in between and thus can be modelled as a planar capacitor with its capacitance defined as $C = \epsilon \frac{A}{w}$ where A is the detector area and w the thickness. The space charge on the plates is then given by

$$Q = AqN_d x_n = AqN_a x_p \tag{3.18}$$

and thus the capacitance C is

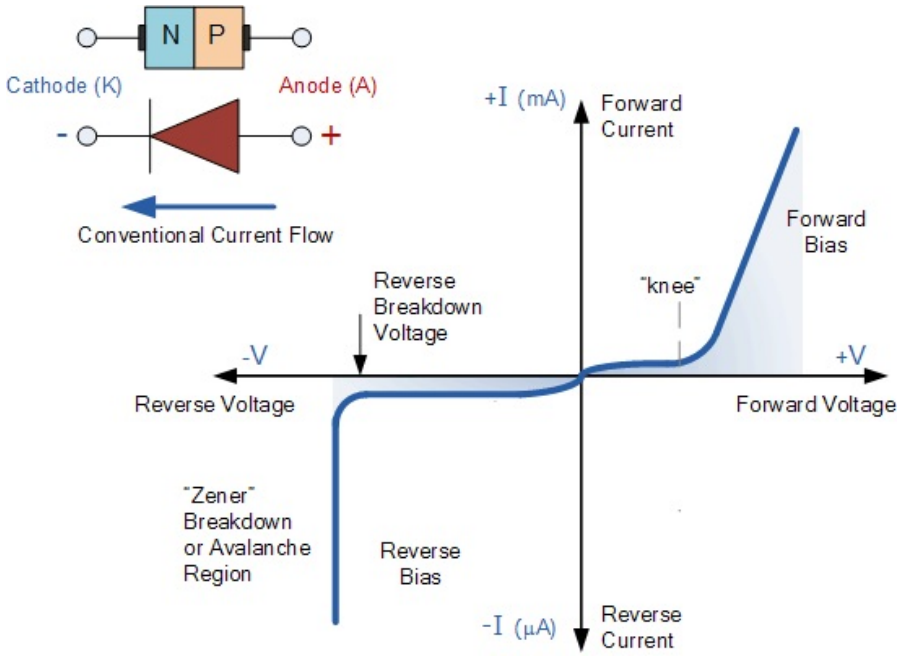

Figure 3.6: Diagram of IV curve for forward and reverse bias.

$$C = \frac{dQ}{dV} = \frac{Aq}{2\sqrt{V_0 + V_b}} \sqrt{\frac{2\epsilon}{q} \left(\frac{1}{N_A} + \frac{1}{N_D} \right)^{-1}} \tag{3.19}$$

Thus the capacitance can be varied using the bias voltage.

Detectors are typically required to have low capacitance values to reduce the noise level and to increase the depletion region and the probability of interaction. This allows to improve the total signal to noise characteristic of the device.

Although in reverse bias, all mobile charge carriers are removed due to the recombination of the excess electrons with the holes, electrons still cross the bandgap due to thermal excitation forming a flow of current called leakage current. The leakage current depends on the temperature and the applied bias voltage (V_b) and is described by [31]:

$$I(T) = I(293) \left(\frac{T}{293} \right)^2 e^{-\frac{E_g(T)}{2k_b T}} \tag{3.20}$$

and

$$I(V_b) = qAw\frac{n_{int}}{2\tau} = qA\frac{n_{int}}{2\tau}\sqrt{\frac{2\epsilon(V_0 + V_b)}{q}\left(\frac{1}{N_A} + \frac{1}{N_D}\right)} \tag{3.21}$$

where τ is the carrier lifetime, n_{int} the intrinsic carrier concentration.

Figure 3.7 shows an experimental IV curve obtained for a 500 μm silicon junction in the reverse bias region at room temperature. As expected the current increases with voltage but remains very small and displays the expected square root behaviour.

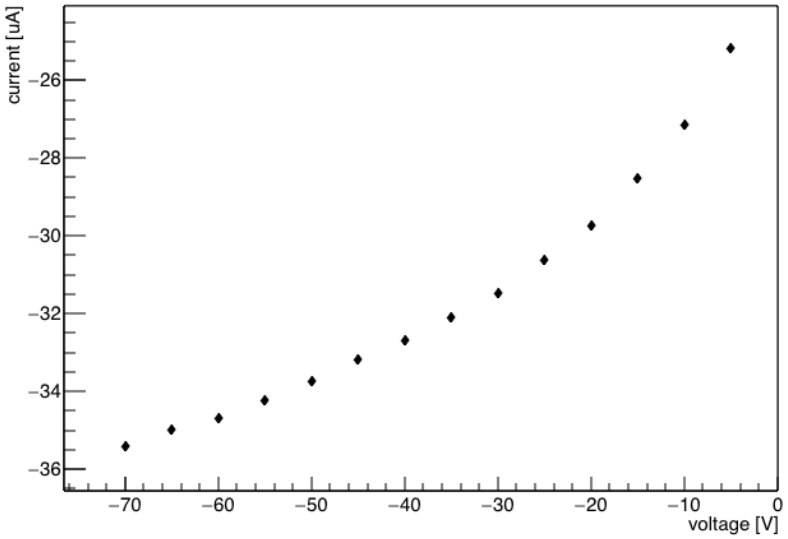

Figure 3.7: The IV for a silicon detector at room temperature.

3.3 Operating the pn-junction as a radiation detector

Most semiconductor radiation detectors are operated as reverse bias diodes. Notable exceptions are SIPMs (silicon photomultiplier), who operated in forward bias just around the knee (see figure 3.6) and diamond detectors, who do not require a pn-junction as the bandgap is so large than there are a negligible number of thermally generated charge carriers present. Typically using an external bias voltage the depleted area is extended to the entire sensor thickness. This maximises

the area with negligible background and thus maximise the sensitive area. The detector can also be operated partially depleted, in this situation the bias voltage applied is lower than the voltage necessary to create a depletion region as wide as the detector. In that case the undepleted part of the detector acts as a high ohmic resistor.

An other alternative is to operate the detector at cryogenic temperatures. In that case the number of thermally generated mobile charge carriers is suppressed simply by the low temperature, see equation 3.6. This has been used successfully in several experiments [32–34].

3.4 Signal generation in semiconductor devices

When particles interact with the detector material, energy is deposited, see chapter 2, and as a result mobile electron hole pairs are created. Due to the bias voltage and the resulting electric field, the electron hole pairs do not recombine but travel towards the electrodes. This results in a current, which induces a current at the detector electrodes as described by Ramo's Theorem [35]:

$$i = E_v q v \tag{3.22}$$

where E_v is the electric field component in the direction of the particle velocity, v the instant velocity of charge carrier and q its charge.

The Ramo's theorem can then be used to identify the total charge generated:

$$\Delta q = q\frac{\Delta x}{w} \tag{3.23}$$

where Δx is the distance between the electron and the hole, and w the detector thickness.

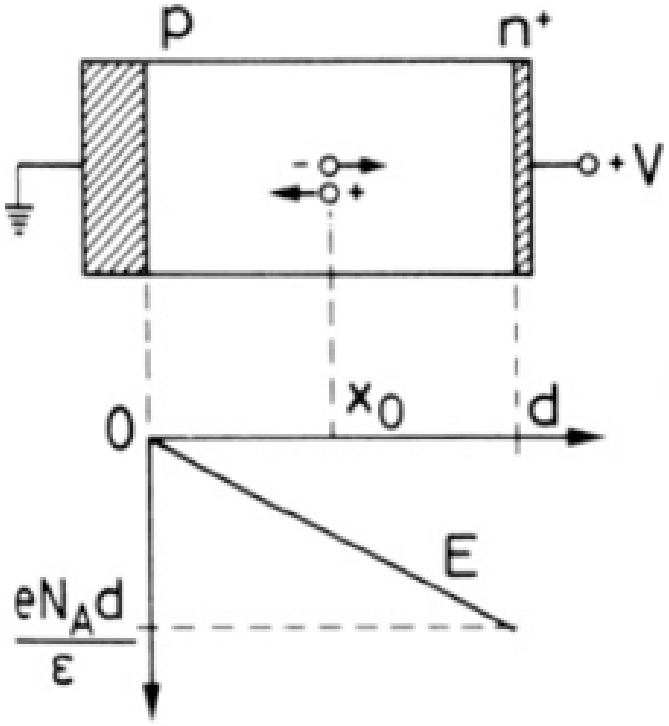

Figure 3.8: pn junction with a fully depleted region. The charge carriers are generate in x. The electric field direction is also showed.

To evaluate the electric field a fully depleted, asymmetric pn-junction detector can be considered, where the detector bulk is p-type as shown in figure 3.8, the electric field $\mathcal{E}$ can be written as

$$\mathcal{E} = -\frac{eN_A}{\epsilon}x = -\frac{x}{\mu_h \tau} \tag{3.24}$$

where $\tau = \epsilon/\sigma = \rho\epsilon$, where ρ is the resistivity and σ the conductivity of the material.

When an electron hole pair is created at a specific position x in the depletion zone, then the generated electron will drift towards the n layer and the hole towards the p electrode. The drift velocity of the electron is given by:

$$v = \frac{dx}{dt} = -\mu_e \mathcal{E} = \frac{\mu_e}{\mu_h}\frac{x}{\tau} \tag{3.25}$$

Assuming the mobilities are independent on the electric field, then its position x a function of time can be written as

$$x(t) = x(0)e^{\frac{\mu_e t}{\mu_h \tau}} \tag{3.26}$$

and the time needed by the electron to reach the electrode is

$$t = \tau\frac{\mu_h}{\mu_e}\ln\frac{w}{x_0} \tag{3.27}$$

which is typically in the order of ns.

The same approach can be taken for the hole. The charged induced by the interaction during the period of time t is given by [14]:

$$\begin{aligned} Q_e(t) &= -\tfrac{e}{w}\textstyle\int \frac{dx}{dt}dt = \frac{e}{w}x_0\left(1 - e^{\frac{\mu_e t}{\mu_h}}\right) \\ Q_h(t) &= -\tfrac{e}{w}\textstyle\int exp\frac{-t}{\tau}dt = \frac{e}{w}x_0\left(1 - e^{\frac{-t}{\tau}}\right) \end{aligned} \tag{3.28}$$

The total electrons and holes collected are obtained by integrating over time equation 3.28.

The total charge collected is then given by the sum of both contribution

$$Q_{tot} = \frac{e}{w} x_0 \left(1 - e^{\frac{\mu_e t}{\mu_h}}\right) + \frac{e}{w} x_0 \left(1 - e^{\frac{-t}{\tau}}\right) = -q \tag{3.29}$$

The induces charge change continuously with time while the charge traverses the space between the two electrodes. This induced charge can be analysed towards the Ramo's theorem equation 3.22. Assuming that a charge created at the opposite electrodes has to cross all the material thickness w the corresponding collection time is given by

$$t_e = \frac{w}{v} = \frac{w^2}{\mu V_b} \tag{3.30}$$

The collection time depends on the mobilities of charge carriers which is different for holes and electrons. Then the collection time can be written as

$$\begin{aligned} t_{ce} &= \tfrac{x}{v_e} = \tfrac{xw}{\mu_e V_b} \\ t_{ch} &= \tfrac{w-x}{v_h} = \tfrac{(w-x)w}{\mu_h V_b} \end{aligned} \tag{3.31}$$

for electrons and holes respectively, where x is the point of interaction. The contribution to the induced charge are then different

$$\begin{aligned} Q_e &= q_e \mu_e \tfrac{V_b}{w^2} \tfrac{xw}{\mu_e V_b} = q_e \tfrac{x}{w} \\ Q_h &= q_e \mu_h \tfrac{V_b}{w^2} \tfrac{(w-x)w}{\mu_e V_b} = q_e \left(1 - \tfrac{x}{w}\right) \end{aligned} \tag{3.32}$$

For example considering a layer of silicon in which and a charge mobilities generation point at $x = w/2$ can be considered as an example. The collection time for the electron is t_e and only half of the total charge is induced. The mobility of the holes ($\approx$450 cm^2/Vs) is approximately a third of the mobility of electrons ($\approx$1450

cm^2/Vs), so in t_e $q_e/6$ is generated, with a total induced charge of 2/3 of the total charge. Additional time is then required for the remaining induced charge to be collected.

The generated signal for holes and electrons is different as shown in figure 3.9.

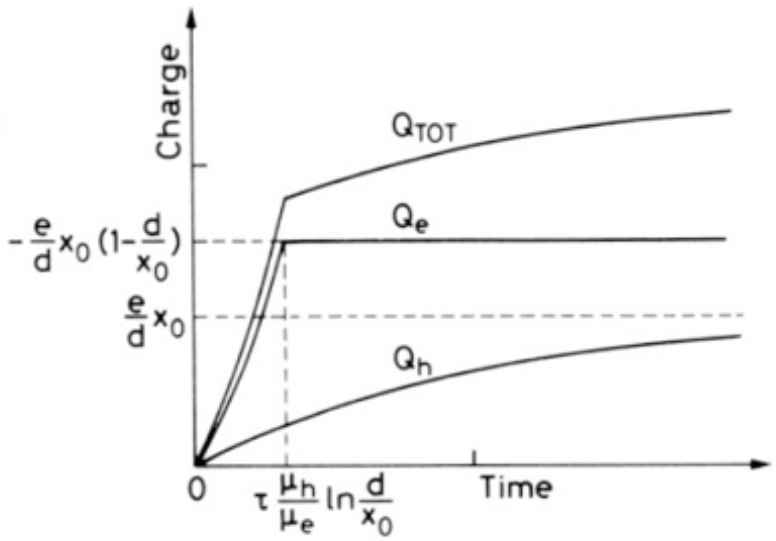

Figure 3.9: Charge collection as a function of time. The charge collection time for holes is slower compare to the charge collection time for the electrons [31].

The total amount of generated electron hole pairs (n_{gen}) is directly proportional to the deposited energy E

$$n_{gen} = \frac{E}{\varepsilon} \tag{3.33}$$

where ε is the energy required to produce an electron hole pair. This energy is at least two time the band gap as an electron need to move from the valence band to the conduction band and a hole need to move from the conduction to the valence band. Table 4.2 shows the band gap energy and the energy required to generate an electron hole pairs for selected materials.

3.5 Summary

In this chapter a brief overview of operational principles of semiconductor detectors was given. Semiconductors offer a viable way to the realisation of efficient radiation

detectors due the relatively low energy necessary to create an electron-hole pair and due to their density being much higher than gas detectors. The moving mobile charge carriers generated by the interaction with particles induce a current which is collected on the electrodes and a signal is generated. The generated signal is proportional to the deposited energy and allows reconstruction of the source spectrum.

Chapter 4 | A Gamma Detector System for Nuclear Fingerprinting

At nuclear power plants many different isotopes are present. Some of them will decay and produce new isotopes. In the decays particles may be emitted. As explained in chapter 2 the most relevant decays for detecting isotopes are the decays in which γ's are emitted. The energy of the photons emitted during the decay can be used to identify the isotopes. The system presented here exploits the differences in cross-section-dependence on the photon energy and Z of the detector material. The developed system consists of 5 different semiconductor detectors with different thicknesses that are selected to work over different energy ranges.

The list of possible isotopes that can be identify, detect and generated in nuclear power plants are limited. Their gamma emission energies are given in table 4.1. Some of them are radionuclides that care left after the decay of heavier elements [5]. Each listed isotope can be found in medical nuclear waste or in nuclear power plant waste. Radioactive materials such as ^{68}Ga, ^{151}Ba and ^{22}Na are produced as waste in medical environment. The other isotopes listed are produced as fission by products of the fuels use in the nuclear power plant, such as ^{241}Pu (found in mixture after the reprocessing process), ^{239}Pu and the U isotopes 235. ^{60}Co can be artificially produced in nuclear reactors. In this project only γ's emitted by radioisotopes listed in table 4.1 have been considered.

The detector developed in this project is based on semiconductor technology. As discussed in section 3, they offer the chance to realise lightweight and cost-effective

Material	Energy (keV)
^{60}Co	1173 and 1332
^{241}Am	59
^{137}Cs	661
^{85}Kr	513
^{192}Ir	317, 468 and 604
^{226}Ra	186
^{22}Na	1274
^{131}Ba	123, 216, 373, 496, 620 and 1047
^{68}Ga	1077 and 1883
^{152}Eu	344, 1112 and 1408
^{131}I	284, 364, 636 and 723
^{210}Po	803

Table 4.1: Energy levels of gammas emitted by the most common sources which can be found in nuclear power plants.

detectors, without strongly compromising the device performance. Five different semiconductor materials were selected and considered appropriate for the scope of this project: Silicon (Si), Diamond, Cadmium Zinc Telluride (CdZnTe), Gallium Arsenide (GaAs) and Uranium Dioxide (UO_2). Those materials were chosen for their different properties, such as Z, band gap and density. Furthermore, with the exception of UO_2, they are well know semiconductor materials used as semiconductor detectors.

4.1 The device concept

To identify isotopes, it is essential to measure the photon energy with good precision. In commerically available devices, this is usually done using spectrometers. These typically consist of small blocks of CdZnTe. When the signal is generated by the interaction between detector and photon, the internal semiconductor convertion due to thermal motion or impurity, can modify the signal generation. This is called noise level and has to be minimize to get a good resolution and good detector response.Due to this effect, the signals measured due to the incoming photon are shaped with slow shapers to maximise the signal-to-noise. This limits the rate to few kHz. For example, the Kromek GR1 CZT has a maximum count

rate of 300000 counts/s [36]. In A.1 more details about noise are given.

The device presented here circumvents the slow shaping process that limits normal detectors with the use of fast amplifiers and thresholding systems. The threshold system is based on setting several thresholds across the energy range of interest, from a few keV up to approximately 2 MeV on a readout chip produced for the ATLAS experiment at CERN. The design of a practical implementation can be found in appendix 4.8. As already mentioned, in the desired application there are a limited number (12) of radioisotopes of concern, with each having a specific set of energy levels (26 in total) that can be distinguished, see table 4.1. As explained in chapter 2, the Compton effect results in a continuum of deposited energy with a characteristic edge, while the photoelectric effect generates a clear peak centred at the isotope's photon energy. The photopeak can be used as the isotope's fingerprint. The photo peaks are detected by comparing count rates at two thresholds: one just below the photon energy and one just above.

The threshold energies are shown in table 4.2. Since the ionisation energy in each detector material is different, the thresholds for them in terms of electron-hole pairs are different for each detector material. In table 4.2 the upper number corresponds to the threshold before the peak and the lower one to the threshold after the photopeak. The threshold, for the purpose of this project, is defined as the value of the energy (or electron-hole numbers) deposited by the incident particle; two different threshold are defined to take into account the Landau shape of the deposited energy in the real experiment one just before the expected photopeak and one after the expected photopeak. This gives 52 thresholds. This method allows the number of counts in each detector material above specific threshold values to be counted simultaneously. Table 4.2 represents the full concept applied to analyse the data to identify the radioactive source. The first column represent the energy value of all possible energy level corresponded to radioactive sources listed in table 4.1. Than the connection between the energy deposited and the

number of electron holes generated is made using equation 3.33, where the value of ϵ is defined in table 4.3 per each selected material. Based on the energy value the thresholds are set between 1 and 4 keV from the energy peaks and the set windows around the peaks have widths between 3 and 7 keV, which is translated in the number of electron holes listed as upper and lower limit per each material. The last column of the table represent the number allocated to each threshold. The number of possible energies is 26, which correspond to 52 different threshold value (th value), two more thresholds where set before the first energy to stabilize the fit (threshold value 1 and 2), so the threshold values corresponded to energy of ^{241}Am (59 kev) are given by the value 3 and 4.

The threshold method uses the integrated number of electron-hole pairs over the total range of electron-hole pairs generated, created above a certain energy threshold, which results in an accumulated energy distribution. Differentiation shows the energy peaks. However, it was chosen to fit the accumulated energy distributions with a set of templates to identify the isotopes. This will be explained in detail in section 4.4.

E keV	**th Si**	**th GaAs**	**th Diamond**	**th CdZnTe**	**th UO_2**	**th value**
59	16306	12734	4515	10390	13812	3
	16473	12864	4562	10496	13953	4
123	34000	26551	9416	21664	28800	5
	34334	26812	9508	21877	29083	6
186	51409	40146	14237	32756	43546	7
	51925	40549	16699	33085	43984	8
216	59700	46621	16533	38039	50570	9
	60300	47089	14380	38422	51078	10
284	78495	61298	21737	50015	66490	11
	79284	61914	21956	50517	67158	12
317	87617	68421	24264	55827	74217	13
	88495	69107	24507	56386	74960	14
344	95078	74248	26330	60581	80537	15
	96034	74994	26594	61190	81346	16
364	100606	78564	27860	64103	85219	17
	101617	79354	28140	64747	86076	18
373	103092	80506	28549	65687	87325	19
	104131	81317	28837	66349	88205	20
468	129350	101011	35820	82418	109568	21
	130650	102027	36180	83247	110669	22
496	137089	107055	37964	87349	116123	23
	138467	108130	38345	88227	117290	24
513	141795	110729	39267	90347	120109	25
	143206	111831	39657	91247	121304	26
604	166939	130364	46230	106369	141408	27
	168617	131675	46694	107438	142829	28
620	171362	133818	47454	109186	145153	29
	173084	135163	47931	110284	146612	30
636	175784	137272	48679	112004	148899	31
	177550	138651	49168	113130	150396	32
661	182692	142666	50592	116406	154751	33
	184531	144102	51101	117577	156309	34
723	199831	156050	55338	127326	169269	35
	201837	157617	55894	128604	170968	36
803	221945	173319	61462	141416	188000	37
	224167	175055	62077	142832	189883	38
1047	289381	225981	80137	184385	245123	39
	292287	228250	80941	186236	247584	40
1077	197673	232456	82433	189668	252146	41
	300662	234790	83260	191572	254678	42
1112	307345	240009	85111	195831	260339	43
	310434	242421	85967	197799	262956	44
1173	324206	253176	89780	206574	274622	45
	327462	255719	90682	208648	277379	46
1274	352120	274974	97510	224360	298266	47
	355659	277738	98490	226615	301264	48
1332	368150	287493	101950	234574	311845	49
	371850	290382	102974	236931	314979	50
1408	389156	303896	107767	247958	329638	51
	393067	306951	108850	250450	332951	52
1883	520442	406419	144123	331609	440845	53
	525670	410502	145570	334940	445273	54

Table 4.2: The threshold levels for each detector and energy. The upper number is the lower threshold value and the lower number is the higher threshold value.

4.2 Choice of semiconductor materials

Several semiconductor materials show the appropriate physical properties to be considered for the realisation of radiation detectors. A non-exhaustive list includes: Si, Germanium (Ge), Cadmium Telluride (CdTe), Cadmium Zinc Telluride (CdZnTe), Silicon Carbide (SiC), Gallium Arsenide (GaAs), Mercuric Iodide (HgI_2) and Diamond. 5 different semiconductors were selected to be employed in the system developed in this work.

- Silicon was chosen because of its moderate intrinsic charge concentration and intrinsic resistivity as well as being a relatively low cost material. These features have led to its widespread use as a detector with a concomitant accumulation of information on how to adapt this material to gain the best performance for a specific application e.g. impurity doping. Due to its widespread use, its integration with a readout system is trivial ([29, 30, 32–34, 37, 38]).

- Diamond because it is a radiation hard material. Detector diamond is manufactured using chemical vapour deposition (CVD) to produce high quality, low impurity crystals that have very low leakage current. Its high radiation tolerance, allows its use in extreme environments that may saturate other detectors ([30]). Other kind of material under intense radiation can be damaged or change their properties.The energy transferred by the interaction of particle may alter the detector performance in different ways: damages on lattice structure, drift in readout electronics, creation of space charge effect and chemical reactions. If the energy transferred in a single event (Single Event Effects) is too high, the damage can be immediate and might reveal to be permanent. In high radiation environmental condition, such as accelerators or nuclear power plants, the energy deposited by interactive particles can damage either the detector or the electronic. The radiation damage may alter the detector performance and structure such as: damage of lattice

structure, creation of space charge effects, drift on the readout electronics and chemical reaction. Two general types of damage occur: bulk damage and surface damage. The damage can be located or clustered. The surface damage, due to ionising energy loss (IEL), has the effect to increase the detector capacitance as well as facilitating the breakdown behaviour. The surface damage involves the defects that are present anyway in the detector. The bulk crystal damage occurs when a lattice atoms is displaced after a particle collision; in this case the energy levels of the semiconductor are modified or new levels are created. An atom can be displaced by its location when the recoil energy of the particle is higher than the energy necessary to dislocate the atom from its lattice (for Si 15 eV [28]). The damage depends on particle and its energy, which is related to the non ionising energy loss (NIEL). The displacement of the atom effects the band structure of the crystal: mid-gap state can be created and the transition between the valance and conduction band is promoted. The current is then increased across the depletion region and the recombination can occur more often due to the mid gap states and the charge can be loss. If the relocation generates a band near by the conduction and valance band edge, charges can be trapped and release after a while which influence the charge collection efficiency (CCE). The last consequence is changing doping characteristic. In figure 4.1 the macroscopic effects of radiation damage are shown [38–43].

- Cadmium Zinc Telluride because it is an established gamma radiation detector material which has a high bulk resistivity and low leakage current. It has been shown to be ideally suited for spectroscopic measurements due to its high detection efficiency, high resolution, thermal stability and relative low cost ([30, 44, 45]).

- Gallium Arsenide because it is a dense material ($5.32/gcm^3$) and therefore has good stopping power for incident photons in comparison to silicon. It also has a higher electron mobility and resistivity than silicon allowing the

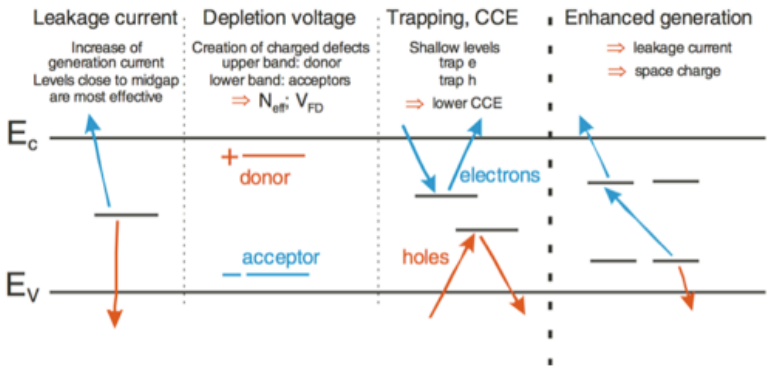

Figure 4.1: Effects of radiation damage in semiconductor.

application of a higher electric field. These properties also allow the detector to be thicker than Si, thereby enabling the exploitation of the full potential of its stopping power ([30, 39, 44, 45]).

- Uranium Dioxide because it is a very high density material (10.97 g/cm^3) and is inherently radioactive. This allows it to be used as a self-calibrating detector. Due to its considerable stopping power on account of its density, it is ideally suited for detection of high energy gamma rays. An additional benefit to using UO_2 is that it also has neutron detection capabilities depending upon the isotopes of Uranium from which the detection crystal is made ([5, 41, 46–49]).

The market was carefully checked to find the best option for the project evaluating the material, material thicknesses, material size and the price. The main features of these materials are summarised in table 4.3.

Material	Si	Diamond	CdZnTe	UO_2	GaAs
Density (g/cm^3)	2.329	3.52	5.78	10.97	5.32
Band Gap ϵ_g eV	1.1	5.5	1.56	2-5	1.42
ϵ **(eV)**	3.62	13	5.65	4.25	4.61
electron mobility μ_e $(cm^2V^{-1}s^{-1})$	1500	2000	1350		8500
hole mobility μ_h $(cm^2V^{-1}s^{-1})$	480	1600	120		400
Z	14	6	48-30-52	92-8	31-33

Table 4.3: Comparison of different semiconductors properties: density, bandgap, energy required to create an electron hole pair, charge carrier mobility and the atomic number ([30], [46], [31].)

4.3 Simulations

In order to study the system proposed in section 4.1, Monte-Carlo simulations were carried out using GEANT4 [50, 51]. GEANT4 was built in 2003 to provide scientist with a simulation toolkit able to simulate the passage of particle through the matter. GEANT4 consist of some fundamental parts which allow to create a reliable system comparable to the reality. The system geometry, tracking, hits and energy deposited in the absorber were built to simulate the real system. The real environmental system can be schematize using the geometry tools, in which is possible define specific material in agreement to what the National Institute of Standard and Technologies (NIST) provides. To create material which is not present in NIST a combination of NIST materials can be used. Additionally, the geometry allows to locate the experimental setup in a specific point in the space, and also to reproduce the dimension of the objects under investigation. GEANT4 was specifically created to simulate the interaction, and absorption, of particles in different detectors. In figure 4.2 a schematic of adopted geometry is shown. The source was placed at a distance of 2 m from the detectors, and to optimise the computational process, photons were emitted in a straight line from the point source to the detector. The space between the detector and the source

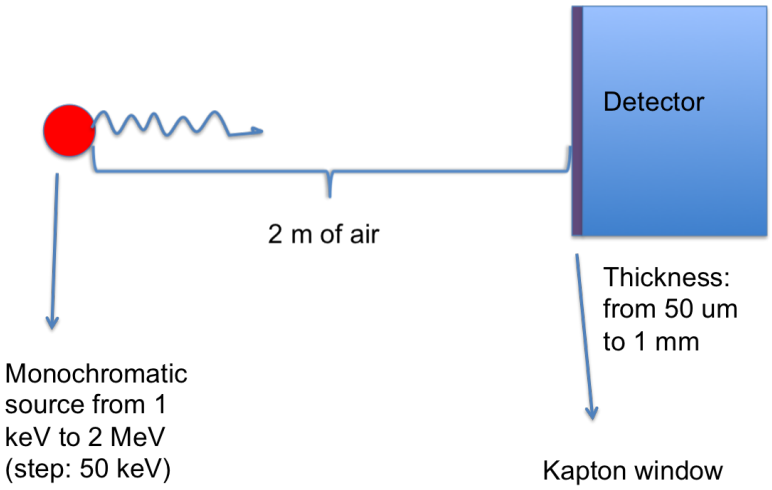

Figure 4.2: Geometry of the simulation.

was filled by air. A Kapton [52] window with a thickness of 8 μm was placed in front of the detector. The detector sizes were maintained constant at 5×5 mm^2. The simulation study was divided into different stages: tests of the response of different detectors to different energies, tests of different thicknesses to find the best material thickness, tests of the selected materials with the sources tabulated in table 4.1, applying the threshold method as discussed in section 4.1 to a single source and to multiple sources. The identification and measurement of the amount of the isotopes will be explained in detail.

Several materials were considered during the first simulation stage: CdZnTe, GaAs, UO_2, Si, diamond, Ge, HgI and SiC. Due to their properties only the first 5 were selected for the actual system. Ge showed a good detection performance, but it needs cooling to liquid nitrogen temperatures to work and HgI is poisonous, which makes them not suitable for application in UAVs. The performance of SiC is comparable to what shown by Si, therefore Si was preferred due to the wide availability of this material.

In figure 4.3 the simulated energy deposited by a 1 MeV photon beam (10^7 photons) in different materials is shown. The materials thicknesses were set to 1 mm. The material with the highest Z, UO_2, stops the largest number of particles, while the diamond (showing a low Z) the smallest. In all the materials it is possible to identify the Compton edge, but only in CdZnTe, GaAs, UO_2 and HgI_2 it is possible

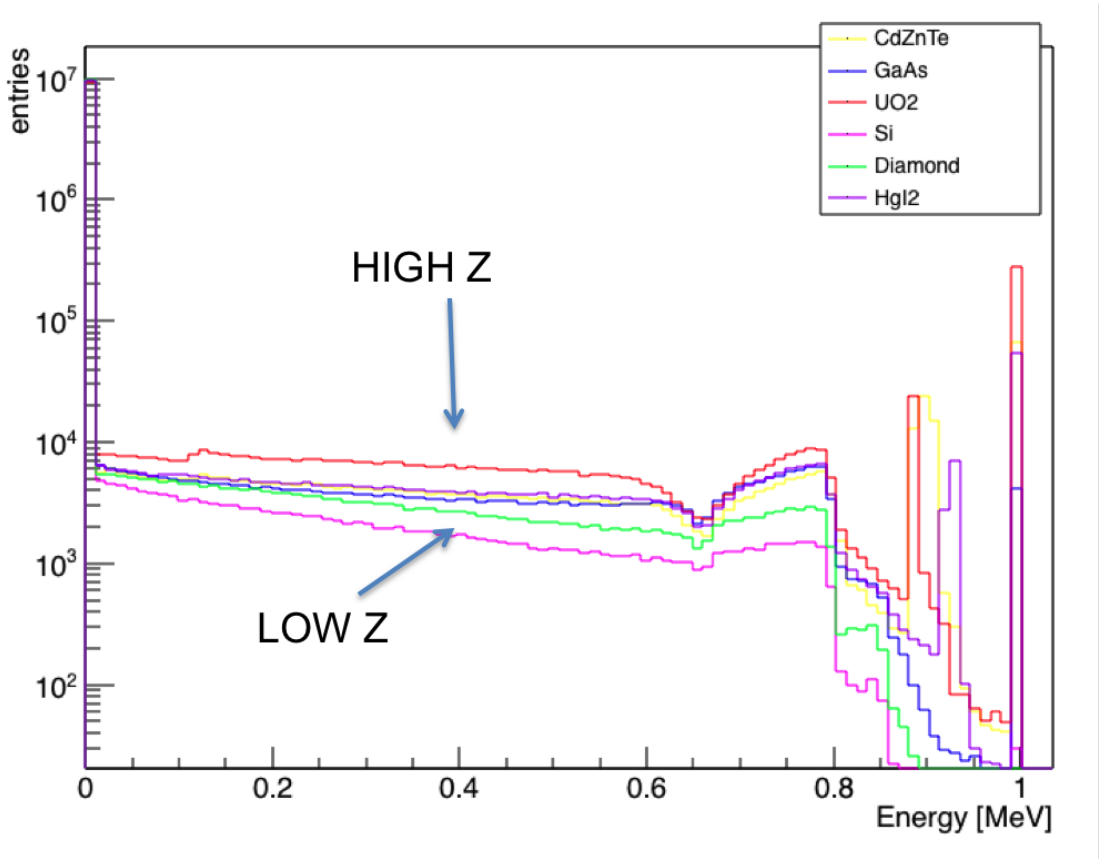

Figure 4.3: Energy deposited by 1 MeV photon beam in different semiconductor materials.

to identify the photopeak. UO_2 detects 5 times more photons in the photopeak compared to HgI_2.

In the simulation, the selected semiconductors were analysed and characterised individually. However, when realising this device, they will be grouped together, resulting in a matrix device that is able to work across an extremely wide energy spectrum.

4.3.1 Simulation of the interaction of photons with matter

As explained in chapter 2, photons interact with matter in 3 different ways according to their energy via the photoelectric effect, Compton scattering and pair production. GEANT4 provides different physics (physics list) and source properties to simulate the physics of the processes, which is the theory model behind the interaction considered. For these simulations the standard electromagnetic physics

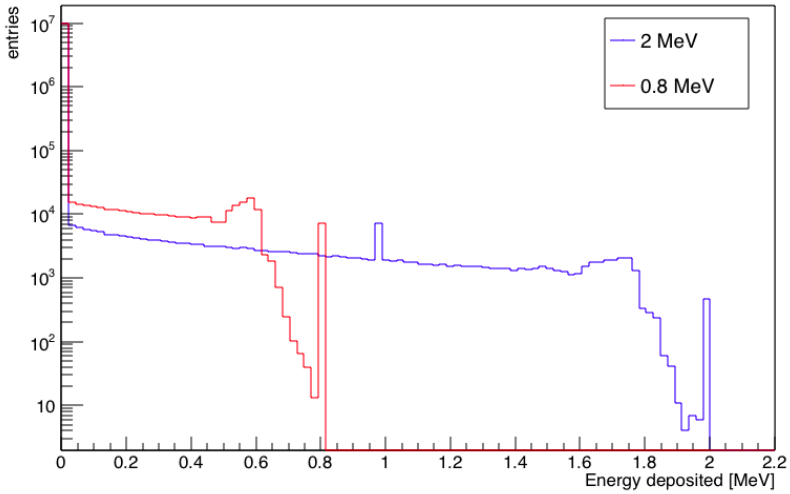

Figure 4.4: Deposited energy spectrum generated by 0.8 MeV photons (in red) and by 2 MeV photons (in blue) in a 1 mm thick GaAs detector.

list was used, in which the interaction of photons with the matter is defined with the probability of each process.

In figure 4.4 the energy deposited in a 1 mm thick GaAs by a 2 MeV and by a 0.8 MeV photon beam is shown. The beam consisted of 10^7 photons. The deposited energy spectrum for 2 MeV photons shows three peaks: the photopeak at 2 MeV, the Compton edge at ∼1.750 MeV and a peak at ∼1 MeV due to pair production. The deposited energy spectrum for the 0.8 MeV- photon beam shows two peaks: the photopeak at 0.8 MeV and the Compton edge at ∼0.6 MeV. The pair production effect does not occur because at least 1.055 MeV of energy is required for this process to occur. A large amount of photons do not interact with the detector, passing through it undisturbed due to the limited thickness of the material which is not sufficient to stop all the travelling photons.

As mentioned in chapter 3 , the deposited energy results in the creation of electron hole pairs. The number of electron hole pairs depends on the ionisation energy

$$n_{e-h} = \frac{E}{\epsilon} \tag{4.1}$$

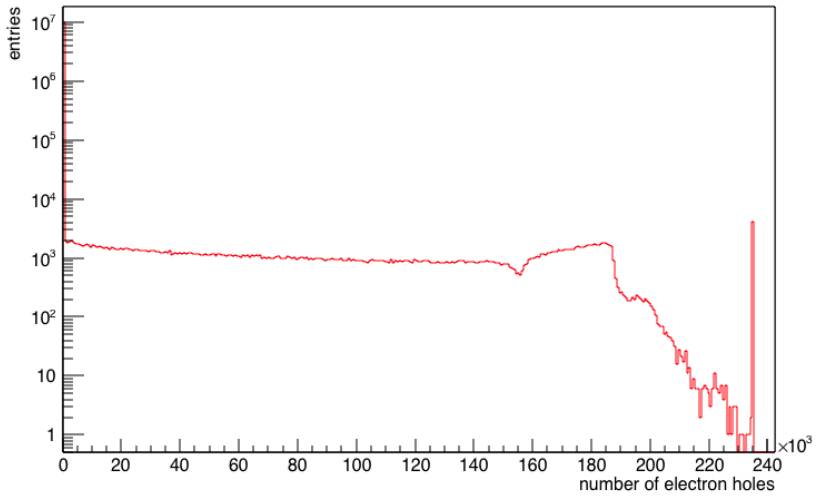

Figure 4.5: Electron-hole pairs in 1 mm thick GaAs detector by 1 MeV photon beam.

Figure 4.5 shows the number of electron-hole pairs generated by a 1 MeV photon beam in a 1 mm thick GaAs detector. Since the number of electron hole pairs is proportional to the deposited energy, all the future studies are shown in term of the deposited energy. The number of electron hole pairs generated in each detector for the same energy photons is quite different. By plotting the deposited energy, the comparison between spectra in different detectors are more easily comparable.

4.3.2 Dependence on material thickness at fixed energy

As discussed in section 2.4 the cross section for photons and thus the deposited energy spectrum depends on the Z of the material, the material thickness and photon beam energy. In this section the energy values deposited by different energy photons, in different thicknesses materials, are presented.

In figure 4.6 the detector response to a 1 MeV photon beam is shown. The material thicknesses considered were: 1000 μm, 500 μm, 300 μm, 200 μm, 100 μm and 2000 μm. As expected, when the material thickness increases the number of collected photons increases as well. Figure 4.6a shows the CdZnTe detector response. A 100 μm thick piece of CdZnTe material is unable to identify the source as no photopeak is present and the Compton edge starts to appear between 0.65 an 0.75 MeV. When

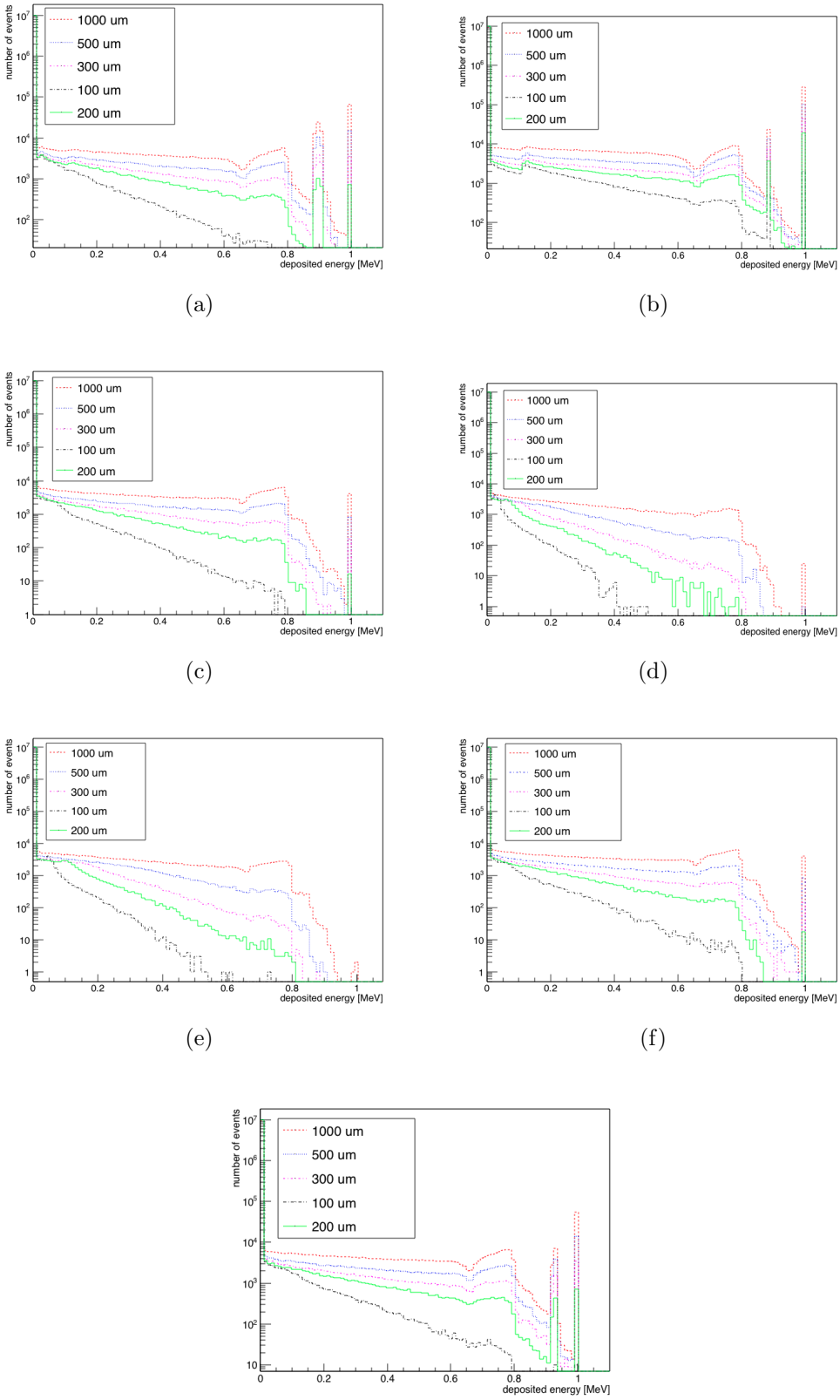

(a) (b)

(c) (d)

(e) (f)

(g)

Figure 4.6: Energy deposited by a 1 MeV photon beam as a function of different material thickness for: a) CdZnTe, b) UO_2, c) GaAs, d) Si, e) diamond, f) Ge and g) HgI_2

the thickness of the detector is increased to 200 μm the obtained spectrum shows the photopeak and the Compton edge. If higher thickness detectors are considered, the energy spectrum is more defined and higher efficiencies are achieved. For example, when the detector thickness is 1 mm a total of $\sim 10^5$ photo peak events are registered while, in contrast, $\sim 10^3$ photons contribute to the photo peak for a 200 μm thickness detector. Figure 4.6.b shows the UO_2 detector response. Compared to CdZnTe, UO_2 has a higher density and also higher Z value. The same thickness pattern is observed but at 100 μm thickness source identification is already possible: the spectrum is more defined compared to CdZnTe and the photopeak and Compton edge are recognisable. Figure 4.6.c shows the response for the GaAs detector. For 100 μm there is no photopeak present, but the Compton edge is already visible. Figure 4.6.d and figure 4.6.e are showing the response for Si and diamond respectively. Compared to the previous materials detectors the response is worst. The photopeak is visible only for a 1 mm thick Si detector. Ge (figure 4.6.f) and HgI_2 (figure 4.6.g) are showing a good trend pattern just as the others: the photopeak can be easily identified for all the different energies.

In figure 4.7 the deposited energy for a 1 MeV photon beam in a 1 mm thick detector is summarised. The photopeak is clearly visible for CdZnTe, GaAs and UO_2, but for Silicon only around 10 events released the photopeak energy in the detector. For diamond detection of the photopeak is impossible, as the deposited energy spectrum stops at approximately 0.8 MeV. The number of events which deposited 1 MeV in the detector is an order of magnitude higher for UO_2 compared to CdZnTe and more than two orders compared to GaAs material.

As the results show, selecting the right detector thickness is fundamental to optimise the response of the detector to radiation. The materials thickness were chosen based on the results of the simulation and the thicknesses available on the market evaluating the price of the detector too.

In thicker detectors the number of photons interacting with the material is higher than in thinner ones. On the market, due to the growth limitations, it is not

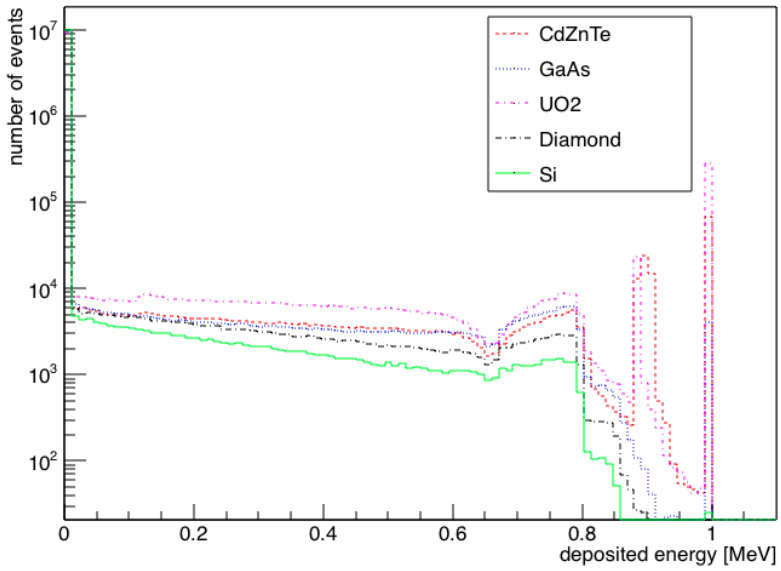

Figure 4.7: Energy deposited by a 1 MeV photon beam in all the detectors considered in the project.

possible find very thick semiconductor materials, for this reason the thicknesses selected are: 1 mm for the UO_2 and GaAs, 0.5 mm for Si and diamond and 2 mm for CdZnTe. Initially, to optimize materials thickness, the number of event collected for each energy and detector was counted and compared with the UO_2 value. Figure 4.8 shows the results for each material (1 mm thick) and for different energies. Clearly, in this way recognised different energies is not possible per each detector: for the CdZnTe there is no difference in counting with respect to the UO_2. The same issue occurs also for GaAs and Germanium, but at higher energy.

Every integral value has to be different for each energy, if this condition occurs is possible identify the source, otherwise the energy is not univocally determined. The integral values were compared for all detectors, energies and thicknesses and the optimum thickness combination was determined. This configuration is shown in figure 4.9.

The detector thicknesses were determinate with these comparisons and material thickness available on the market.

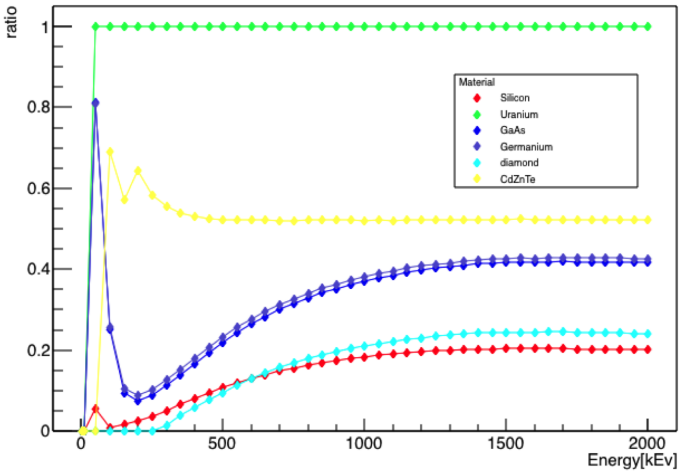

Figure 4.8: Number of event collected in each detector per each energy in 1 mm of material.

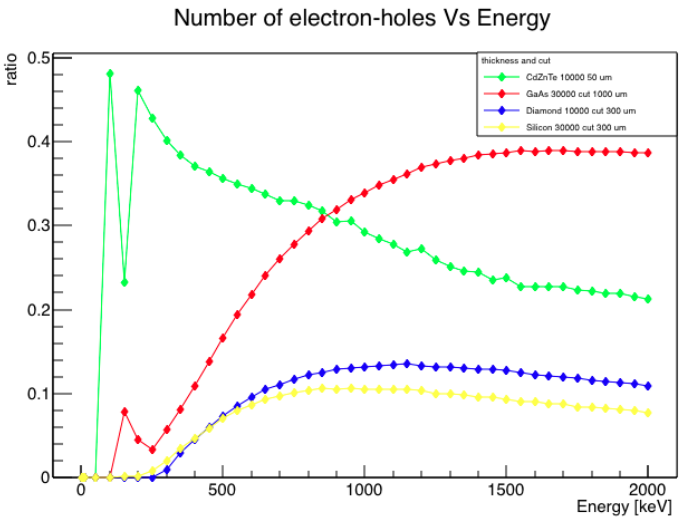

Figure 4.9: Best material thickness combination.

4.3.3 Dependence on energy for fixed thickness

As explained in chapter 2, the cross section for photons is dependent on the photon energy. This becomes visible in the spectrum. In figure 4.10 the deposited energy in 1 mm thick detectors by photons with an energy of 1.5 MeV, 1.2 MeV, 1 MeV, 0.8 MeV and 0.5 MeV is shown for: a) CdZnTe, b) UO_2, c) GaAs, d) Si, and figure 4.11 a) diamond, b) Ge and c) HgI_2. As expected, with increasing energy the photopeak moves towards higher values for all the detector materials. In CdZnTe, UO_2, GaAs, HgI_2 and Ge materials the photopeak is well definend for all energies studied. The number of events registered in the photopeak changes due to the Z of the material: the highest amount is recorded for the UO_2 detector in all the scenarios. Diamond and Si behave differently from the other materials. Diamond, see figure 4.10, shows a clear photopeak only for 0.5 MeV and 0.8 MeV photon beams. For the other energies only the Compton edge is visible. The photopeaks for Si, see figure 4.10.d, are clearly visible for all the photon energies. However, with increasing energy the number of events contributing to the photopeak decreases rapidly.

The deposited energy spectrum varies depending on the energy of the photon beam and the material chosen as detector. Some detectors, such as Si and diamond, work better for the lower energy range otherwise the acquisition time should be significantly increased compared to other detector materials studied, such as UO_2 and CdZnTe. As an example, to identify ^{60}Co source using a CdZnTe detector 1440 photons must interact with the detector, while for Si 7774000 photons have to reach the detector to be able to identify the source. Depending on the activity of the source the acquisition time has to be increased to obtained the minum number of photon which permits the identification.

4.3.4 Source Simulations

All 12 possible sources summarised in table 4.5 were simulated for all the selected detectors. The simulated photon beams consist of 10^7 photons of that specific

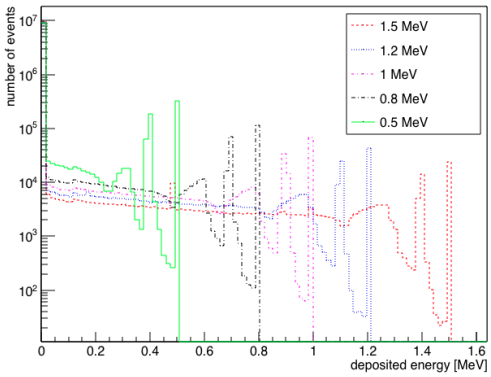

(a)

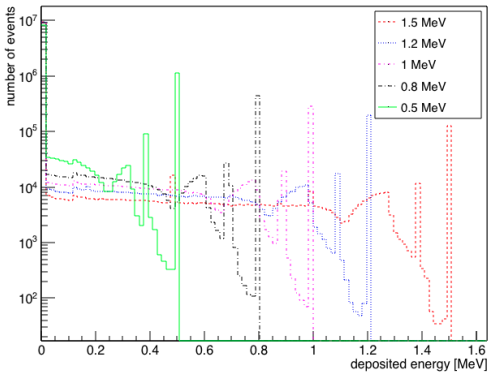

(b)

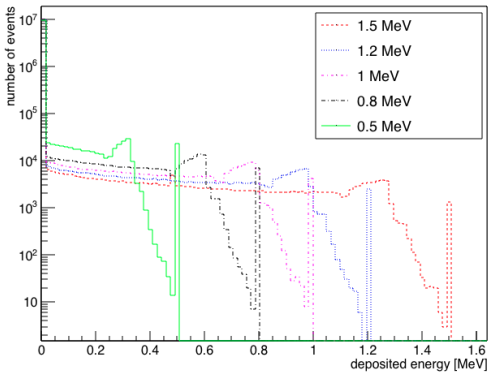

(c)

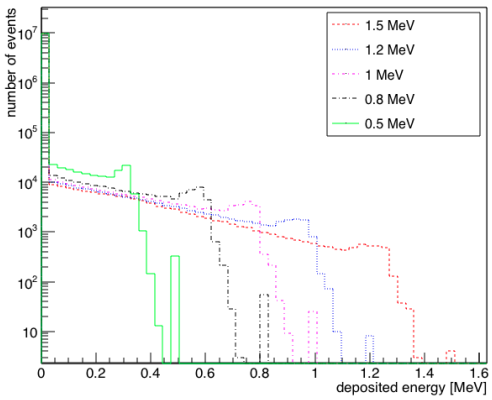

(d)

Figure 4.10: Energy deposited by different photon energy beam in 1 mm thick material: a) CdZnTe, b) UO_2, c) GaAs, d) Si.

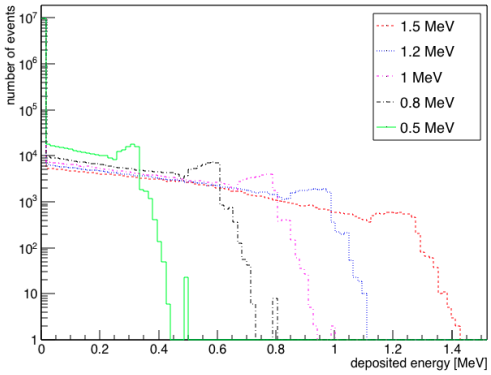

(a)

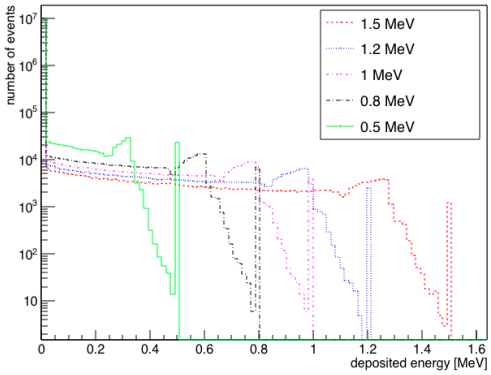

(b)

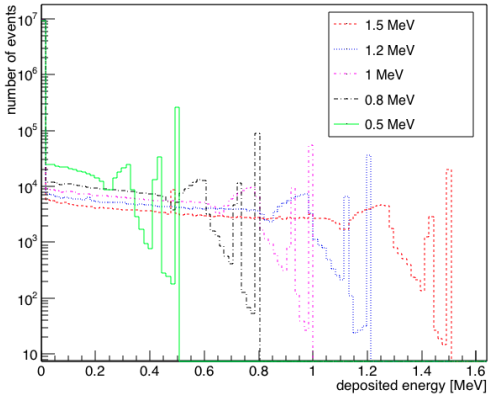

(c)

Figure 4.11: Energy deposited by different photon energy beam in 1 mm thick material: a) diamond, b) Ge and c) HgI_2.

source. Detector materials respond to different sources in different ways, as shown in 4.12 and 4.13. Sources that emit more than one energy photon show different behaviour in different detectors due to the different photon energies. For example figure 4.12.f which shows the response to ^{68}Ga which emits a photon on 1077 keV and a photon of 1883 keV,shows that the first photopeak is almost visible for all the detectors, while the other is not visible for Si and diamond. The last peak has a different ratio between UO_2 and GaAs, with a gap of almost 2 orders of magnitude. For all sources the UO_2 detector response and the CdZnTe is almost comparable, as already shown.

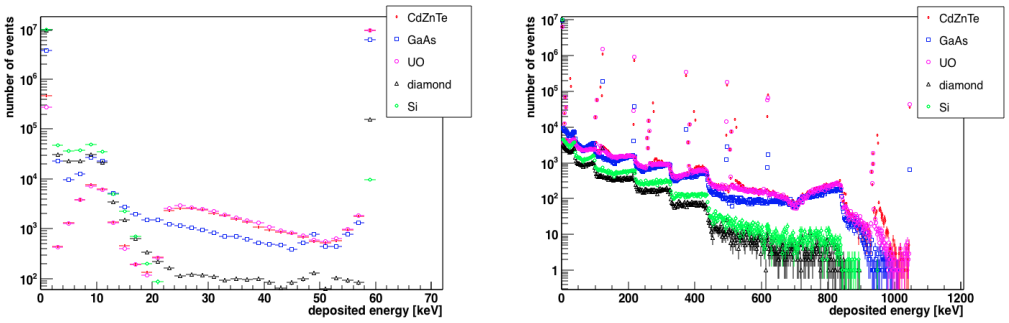

(a)

(b)

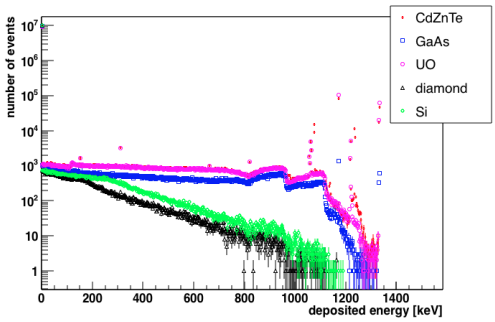

(c)

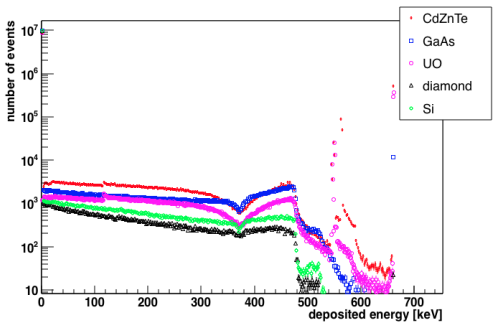

(d)

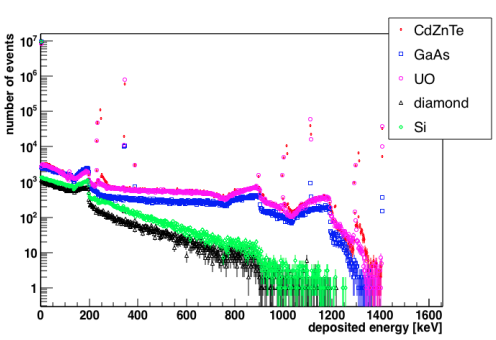

(e)

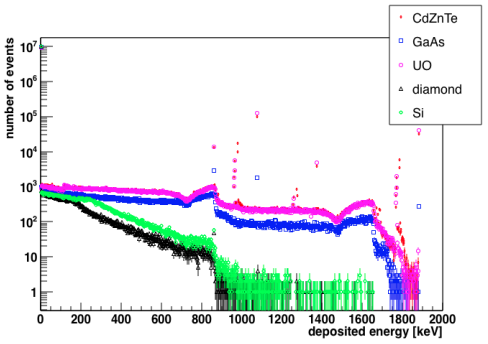

(f)

Figure 4.12: Energy deposited in different detectors by 10^7 photons of different sources: a) ^{241}Am, b) ^{131}Ba, c) ^{6}0Co, d) ^{137}Cs, e) ^{152}Eu, f) ^{68}Ga.

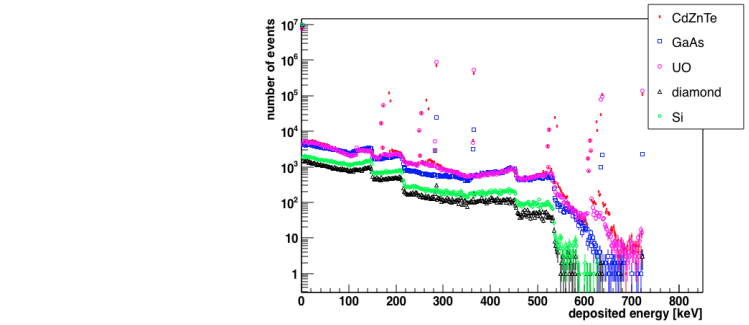

(a)

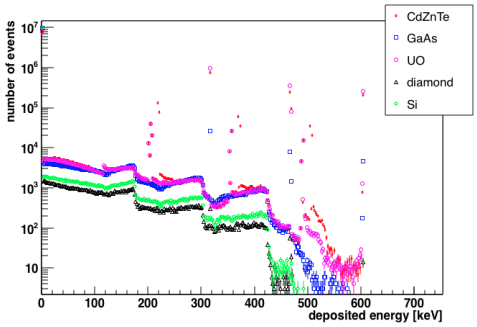

(b)

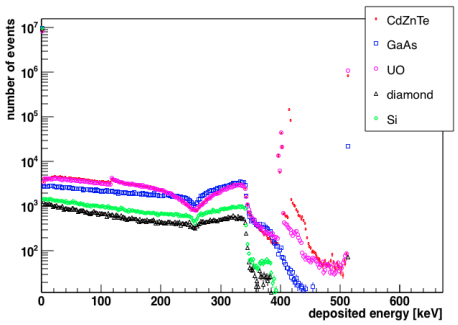

(c)

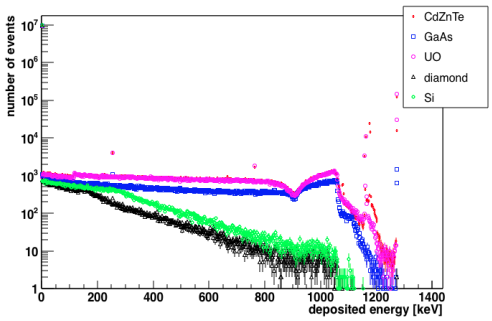

(d)

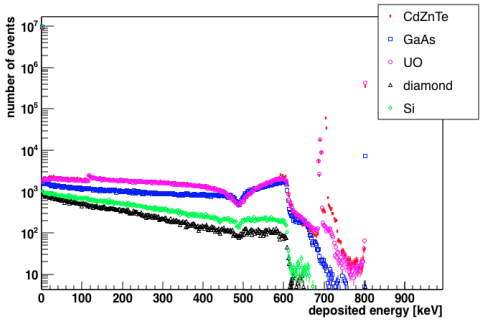

(e)

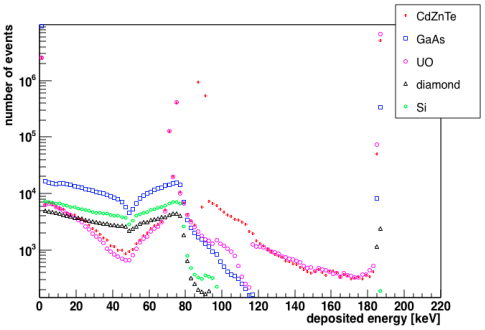

(f)

Figure 4.13: Energy deposited in different detectors by 10_7 photons of different sources: a) ^{131}I, b) ^{192}Ir, c) ^{85}Kr, d) ^{22}Na, e) ^{210}Po, f) ^{226}Ra.

4.4 The reconstruction method

As discussed in section 2.4, the photon interaction cross section is determined by the energy of the incident photon and the Z of the detector material hosting the interaction. From the energy simulation study, discussed in section 4.3.3, silicon and diamond are suitable for low energy photons up to 0.15 MeV, GaAs is able to operate for mid range energy up to 0.9 MeV, CdZnTe is selected to work at a high energy range up to 2 MeV. Moreover the UO_2 can cover the entire range of energy that can be found at a nuclear power plant.

Figure 4.14 shows the simulated spectrum plot (blue line) for a ^{60}Co source in a 1 mm thick UO_2 detector. The detector system presented here uses two thresholds around the photopeaks. Hence, each threshold registers the total number of energy deposits over the threshold. Figure 4.14 (red) also shows the number of detected energy deposits over the threshold, i.e. the accumulated number of deposits, as a function of the threshold value. The line shows clear steps around the photopeaks.

Initially templates with the 12 sources were created for each detector. The sources were all simulated with 10^7 photons. The threshold spectrum was then created and the fit was applied to the simulation under analysis. Only the number of events above each of the 52 thresholds are recorded , see table 4.2. The templates are shown in figure 4.15 . They show different trends which allows to identify the source and reconstruct the relative amount using a fit to measured spectra that optimises the amplitudes of each individual templates for each source.

4.4.1 Radioisotopes identification

The reconstruction method can be split in two different challenges: radioisotope identification and evaluation of relative activities of the identified radioisotopes. Here the identification procedure is presented. First of all the template was created using a single source and the number of photon in each bin were counted. This number is related to the deposited energy and to the relative photopeak. this number is different for each source and so the difference between the counting rate

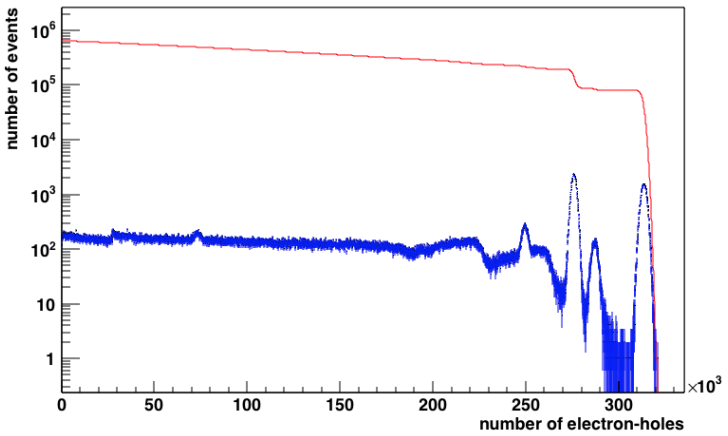

Figure 4.14: In blue the number of electron-hole pairs produced in a 1 mm thick UO_2 detector is shown for a ^{60}Co source. The accumulation plot is shown in red. Please note the log scale on the y axis.

after and before the photopeak considered. Than the chi-squared was minimized. After measuring an unknown spectrum, the spectrum is fit with the template to extract the amplitudes of the individual photon signals. Two criteria were set for single source identification: the reconstructed amplitude has to be 4σ above 0 and the number of reconstructed photon have to be in the range of the simulated number of photons within $\pm 4\sigma$. These conditions were applied to each source in each detector to prove the validity of the method and to find the minimum amount of incident photons necessary to detect the presence of the source. The value of σ was chosen to get reduce the probaility of identify the wrong source.

Before the limits were studied, the robustness of the fits and the fit uncertainties were studied. This was done by studying the emission of 5002000 photons from ^{152}Eu into a 500μm thick Si detector and 24 photons from ^{226}Ra in a 1 mm thick UO_2 detector. This was repeated 100 times and the fit was performed. The results are show in figure 4.16. Each point represents the number of photons identified with the applied fit and the error bars are given by 4σ. As expected, the resulting amplitudes are uniformly distributed around the correct value for both cases. Figure 4.17 shows the distribution of the resulting amplitudes including a Gaussian fit. The results reconfirm that the results are Gaussian distributed around the correct value (emission of 5002000 photons and reconstructed 5.03×10^6). The

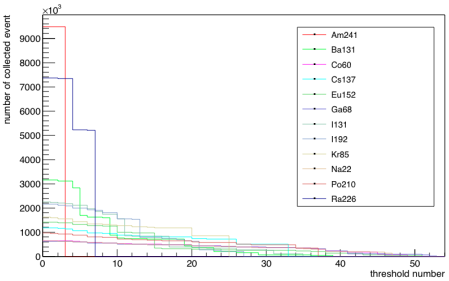

(a)

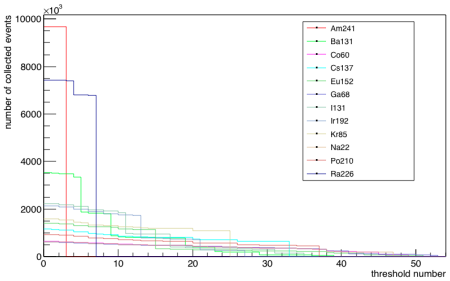

(b)

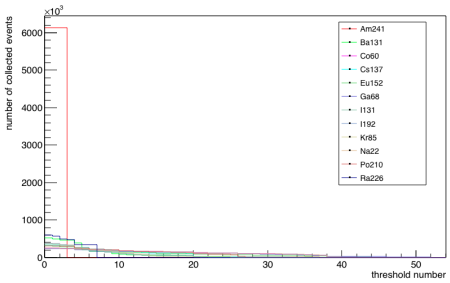

(c)

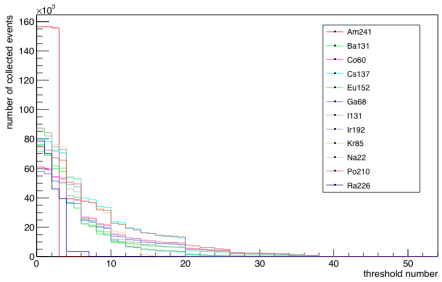

(d)

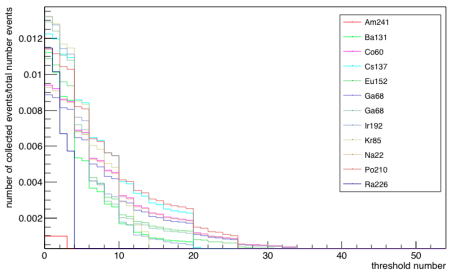

(e)

Figure 4.15: Fit template in all detectors for each source: a) CdZnTe, b) UO_2, c) GaAs, d) Si, e) diamond based on table 4.2.

source	fit value	error value	identification
Am	2045	1577.7	NO
Ba	1012000	8347	YES
Co	2.245	290.328	NO
Cs	6049	4020.7	NO
Eu	-10.91	406.73	NO
Ga	-1.205	193.426	NO
I	-267.3	7438.1	NO
Ir	-6524	6958.6	NO
Kr	329.8	3923.4	NO
Na	2.033	196.558	NO
Po	-19580	3526	NO
Ra	3266	2124.2	NO

Table 4.4: Fit results for all 12 sources. 10^7 photons from ^{131}Ba were simulated and deposited their energy in 2 mm thick CdZnTe detector. As expected the only detected source was ^{131}Ba.

result for Ra shows an additional quantisation effect (the numer of photons reconstructed drops very rapidly and sometimes is 0), which is only relevant for very small numbers of photons. The results show that the fit error is a good reflection of the uncertainty in the amplitude, i.e. the number of reconstructed photons.

In figure 4.18 the fit results for 10^7 photon of ^{131}Ba isotopes in 2 mm thick CdZnTe is shown, as expected only ^{131}Ba was identified correctly. The source template amplitudes and their errors are listed as well in table 4.4. The reconstructed value for Ba is $1.012\times10^7\pm\ 8.347\times10^3$, while for the other possible sources the reconstructed amplitudes are consistent with 0 within errors. The chi-square value founded is lower than 1 but close to it which means that fit and data are in good agreement. The applied fit takes in count all possibles combination of sources and the negative numbers can be considered 0.

The same fit was applied to different numbers of photons for the same single source of Ba to verify the capability to identify the source and reconstruct the correct amount of photons. Figure 4.19 a shows how the number of reconstructed photons increases proportionally to the number of simulated photon for the Ba fit parameter. As an example, the number of photons wrongly identified as coming from a Ga source remains compatible with 0 with errors, as shown in figure 4.19b).

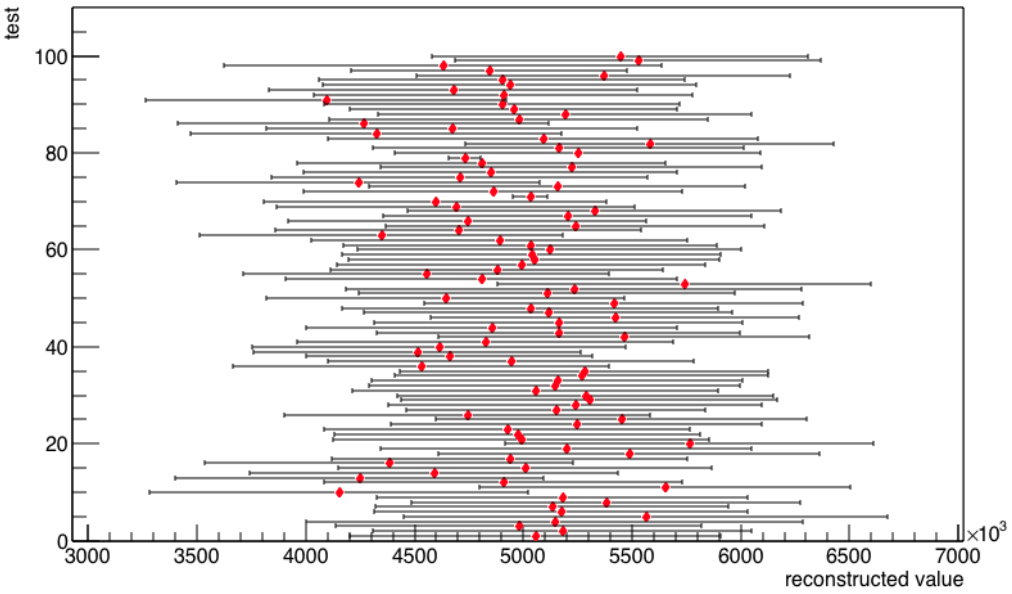

(a)

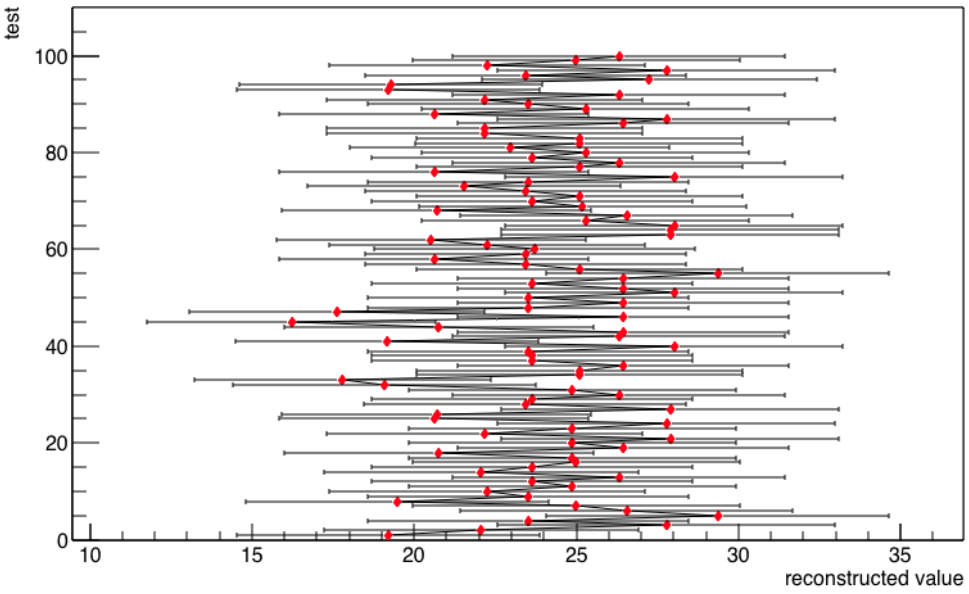

(b)

Figure 4.16: Value of the reconstructed amplitude for the Eu in a)Si and the b)Ra amplitude in UO_2.

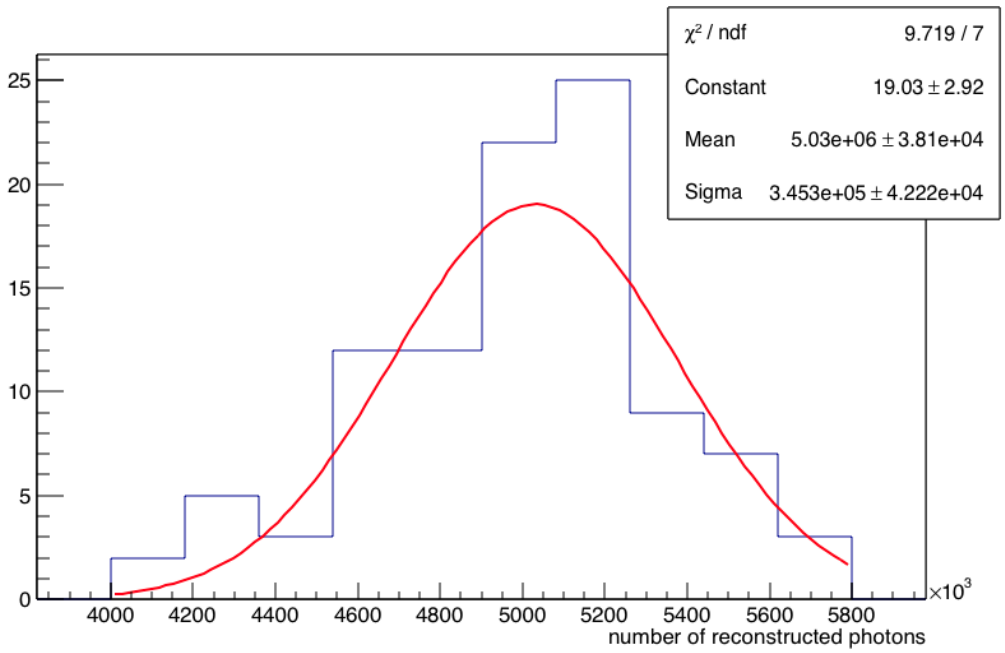

(a)

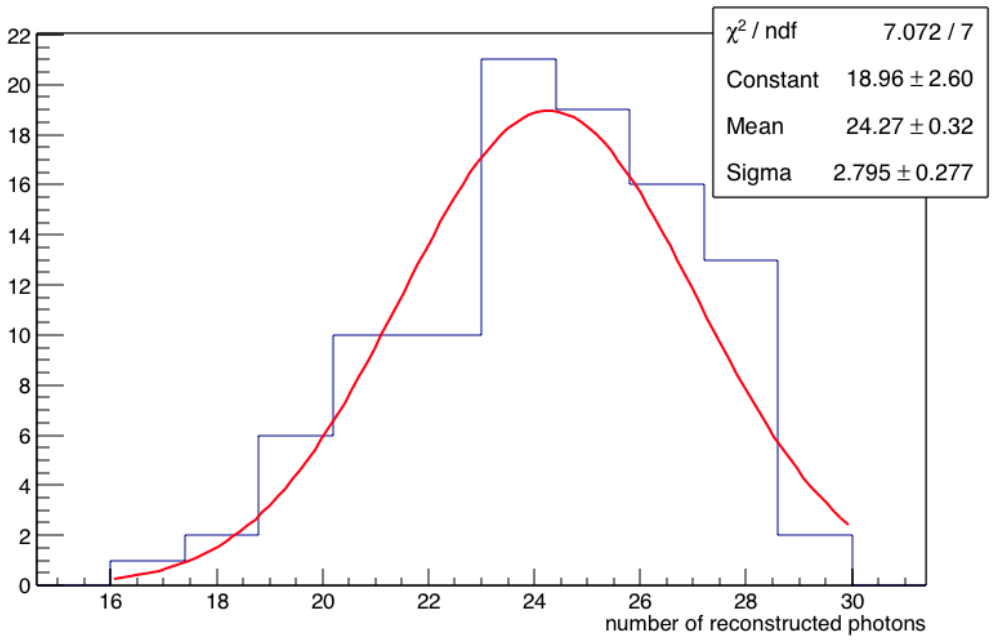

(b)

Figure 4.17: Gaussian fit for the reconstructed parameter for the Eu parameter in Si and Ra parameter in UO_2.

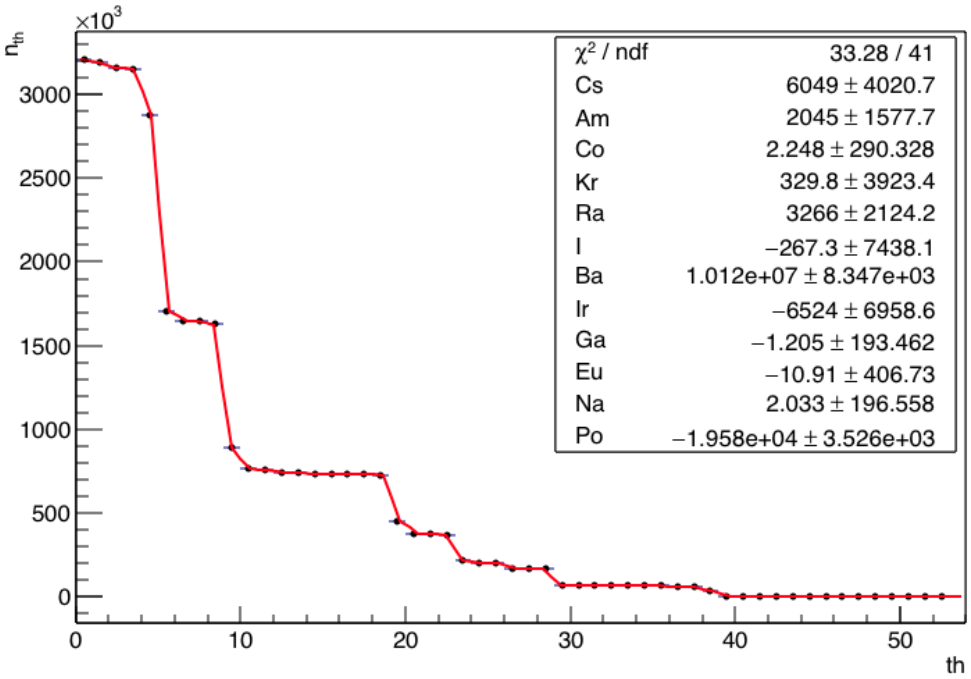

Figure 4.18: Fit to the reconstructed measured spectrum for 10^7 photons beam of Ba source in a 2 mm thick CdZnTe material. The dots represent the accumulation plot, while the red line is the fit.

This study was repeated using an Ir source and a 1 mm thick GaAs detector. Figure 4.20.a shows the results for Ir source, while figure 4.20.b shows the number of photons wrongly reconstructed as coming from a Na source. Again, as expected when the number of photons increases also the number of reconstructed photons for the Ir source increases linearly. The number of photons wrongly identified as coming from Na source remains compatible with 0 within errors.

These two results show that the method works well to detect sources and reconstruct their amplitudes correctly.

The identification criterion can be used to determine the minimum amount of photons required to detect each source and detector. To verify the robustness of the fit 10 different simulations under the same conditions (number of photons and source) were performed. The minimum amount of photons was evaluated using the identification criterion. The results for each source and detector are shown in

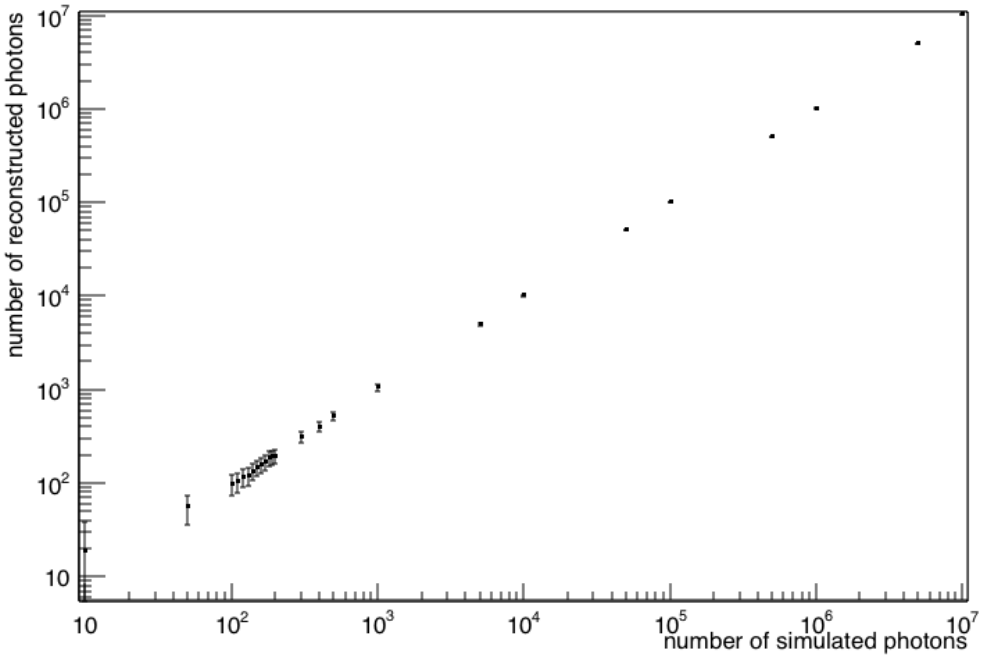

(a)

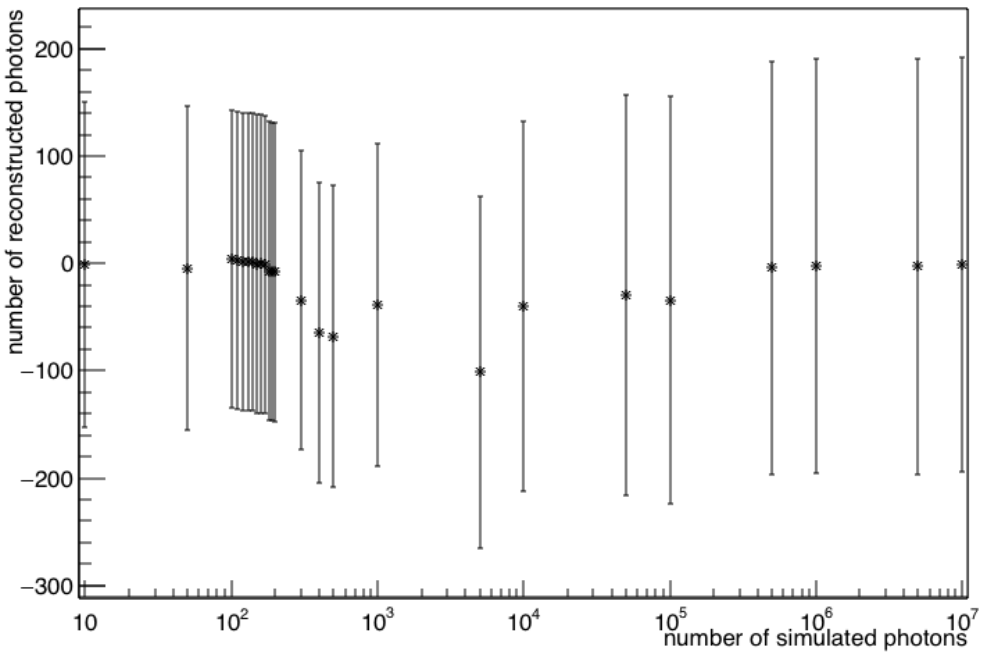

(b)

Figure 4.19: Number of reconstructed photons as a function of the number of simulated photons from a Ba source in 2 mm thick CdZnTe material. Figure a) shows the reconstructed Ba source photons and figure b) the number of photons wrongly reconstructed as coming from a Ga source. The number of reconstructed photons for the Ba source increase linearly with the number of simulated photons while the number of photons reconstructed wrongly as coming from Ga remains 0 within errors.

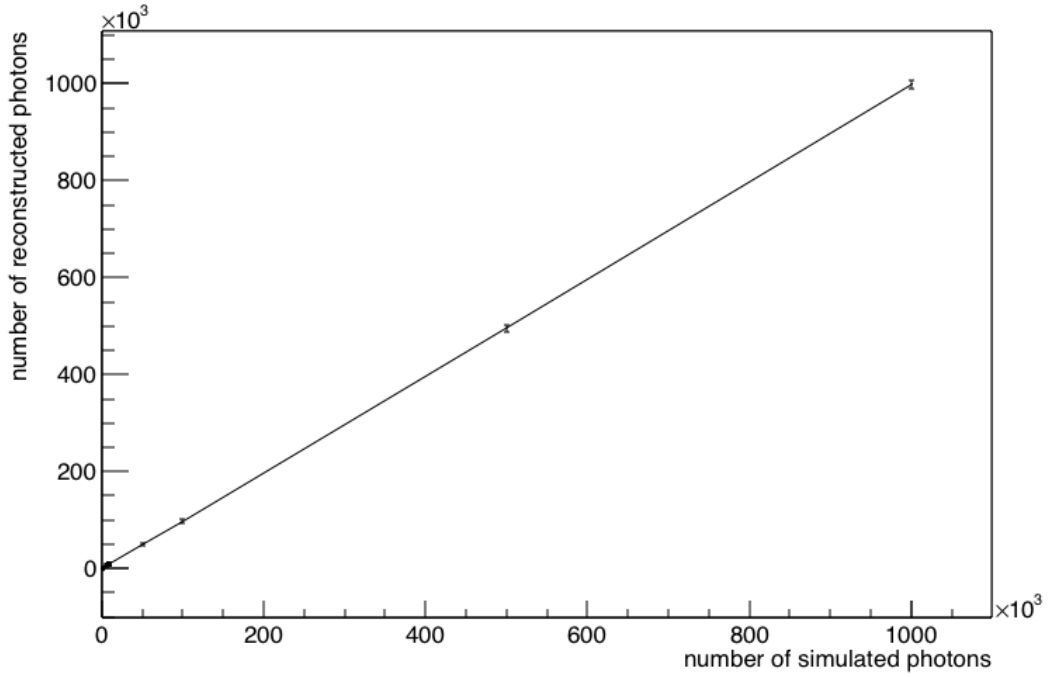

(a)

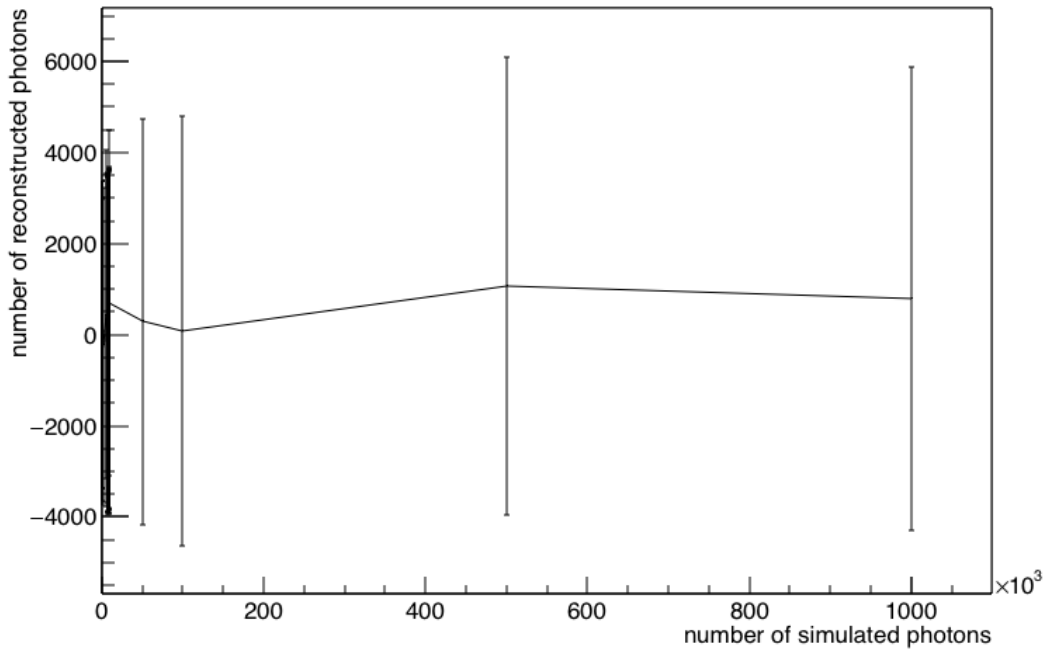

(b)

Figure 4.20: Number of reconstructed photons as a function of the number of simulated photons from a Ir source in 1 mm thick GaAs material. Figure a) shows the reconstructed Ir source photons and figure b) the number of photons wrongly reconstructed as coming from a Na source. The number of reconstructed photons for the Ir source increase linearly with the number of simulated photons while the number of photons reconstructed wrongly as coming from Na remains 0 within errors.

	GaAs	Si	CdZnTe	Diamond	UO_2
Am	27	1740	13	41150	13
Ba	2580	512000	150	201100	130
Co	35000	7774000	1440	5402000	1330
Cs	3500	501000	310	803000	220
Eu	210900	5002000	290	5001000	220
Ga	6750	-	7120	-	510
I	15300	860500	230	715000	220
Ir	8600	141600	220	96100	180
Kr	3300	117950	180	314000	360
Na	299000	5724000	1520	4001000	1140
Po	1880	166050	360	805000	270
Ra	1010	130200	31	36100	24

Table 4.5: Minimum number of photons required to identify a source in each detector.

table 4.5. For Si and diamond it was not possible identify the Ga source up to 5×10^7 simulated photons.

The fit parameter errors with multiple sources are higher than for single sources due to the contributions of all sources to the deposited energy. To prove that the identification criteria works as well in mixtures, several mixtures with different sources with the same amount of photons were created. For all of photons sources 10^4 photons were simulated. In table 4.6 the mixtures created are summarised and the fits are shown in figure 4.21. Mix 1, shown in figure 4.21.a, consists of 4 different sources: Ba, Ga, Po and Kr. The fit results show that those 4 sources are correctly identified in the mixture and the number of reconstructed photons are 10080±480 for Ba, 11010±549 for Ga, 9679±435 for Po and 9846±327 for Kr. Figure 4.21b shows the corresponding fit results for mix2. The reconstructed number of photons are 100110±357 for I and 10230±366 for Ir. Figure 4.22a shows the fit for mix 3. The reconstructed number of photons are 10370±1014 for Co, 10240±142 for Ra, 9945±575 for I, 10280±618 for Eu and 9543±876.4 for Na. The final mixture, see figure 4.22b, consists of a mixture of all 12 sources, and the fit result show the correctly reconstructed values: for Am 10180±149, for Ba 9954±842,for Co 10720±1444, for Cs 10600±672, for Eu 10200±1050, for Ga 11030±696, for I 9507±956, for Ir 10280±899, for Kr 10050±523, for Na 9361±1142, for Po 10300±681 and for Ra 10200±210.

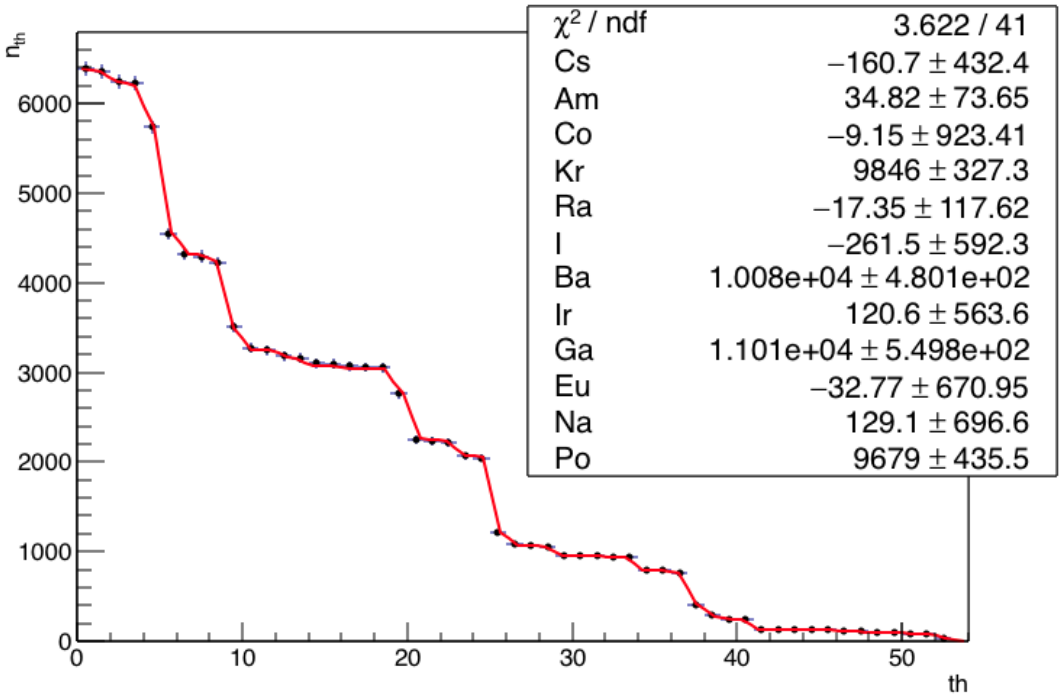

(a)

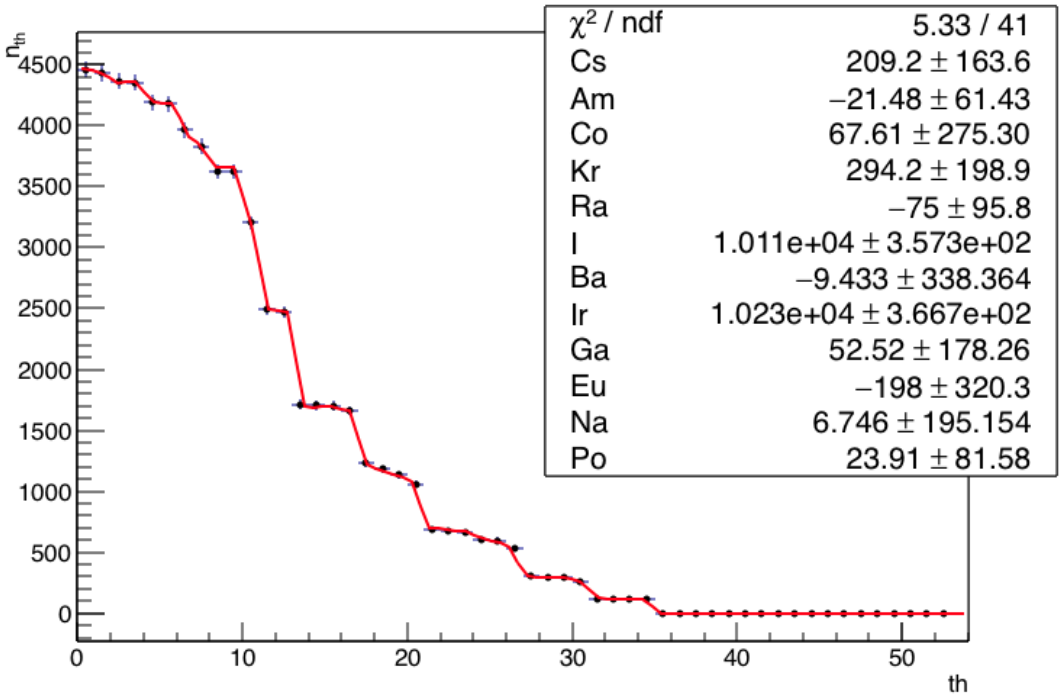

(b)

Figure 4.21: Fit results for the mixtures summarised in table 4.6: a) mix 1, b) mix 2.

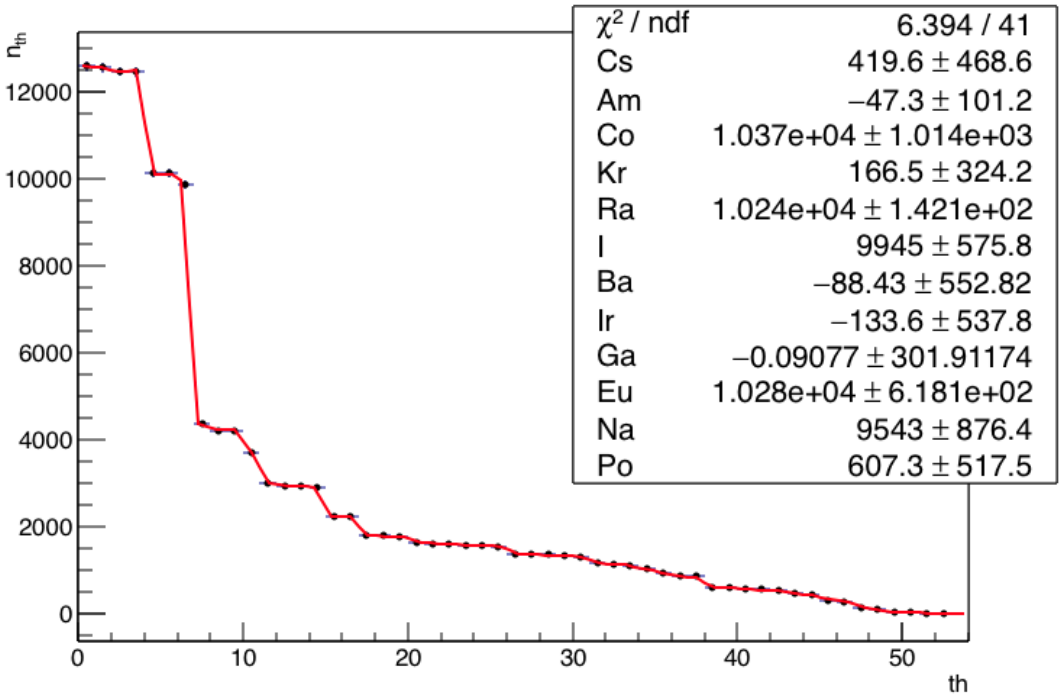

(a)

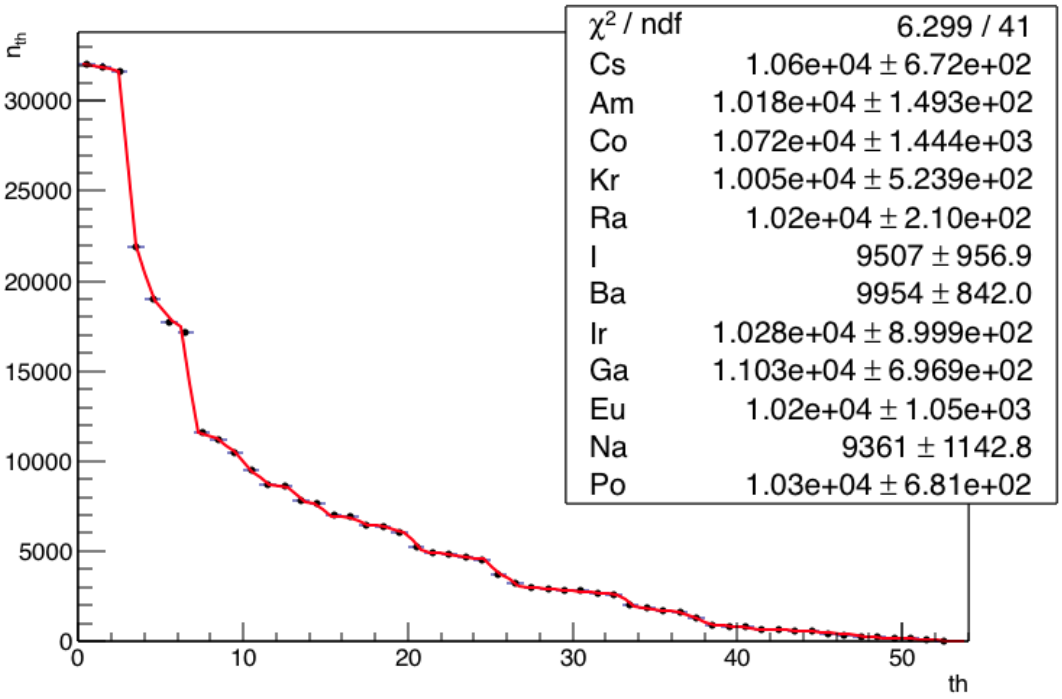

(b)

Figure 4.22: Fit results for the mixtures summarised in table 4.6 a) mix 3 and b) mix 4.

	sources
mix 1	Ba, Ga, Po and Kr
mix 2	Ir and I
mix 3	Eu, Ra, Na, Co, I
mix 4	all sources

Table 4.6: Mixtures of sources created. All the sources have the same amount.

	Cs	**Am**	**Co**
mix 1	0.6	0.3	0.1
mix 2	0.3	0.4	0.3
mix 3	0.4	0.3	0.3
mix 4	0.2	0.2	0.6
mix 5	0.2	0.3	0.5

Table 4.7: Mixtures of sources created. The total amount was kept constant.

The results prove that the threshold technique allows source identification not only for a single sources but also within a mix of different sources with the correct amplitudes. This demonstrated the validity of the device concept.

4.4.2 Relative activities studies

In real conditions it is likely that sources are mixed with different ratios. To study the application of the threshold analysis to real conditions different unknown mixtures were created by modifying the number of sources present and their amount. Three different sources were considered using a 1 mm thick UO_2 detector. The mixtures consisted of Co, Cs and Am sources of which the amounts were changed as listed in table 4.7. The total amount of photon was varied but the source percentage was kept constant in each run and mix.

The total amount of photons emitted by the mystery box was kept constant at 10^8 to evaluate the reconstruction performance of the threshold system. The results are shown in figure 4.23. In all mixes the reconstructed value and the simulated number of photons are in good agreement for all sources.

To study the independence of the reconstructed value on the total amount of photons and the different amount of each source other simulations with different sources were created. The mixtures consists of 3 different isotopes: Co, Ga and

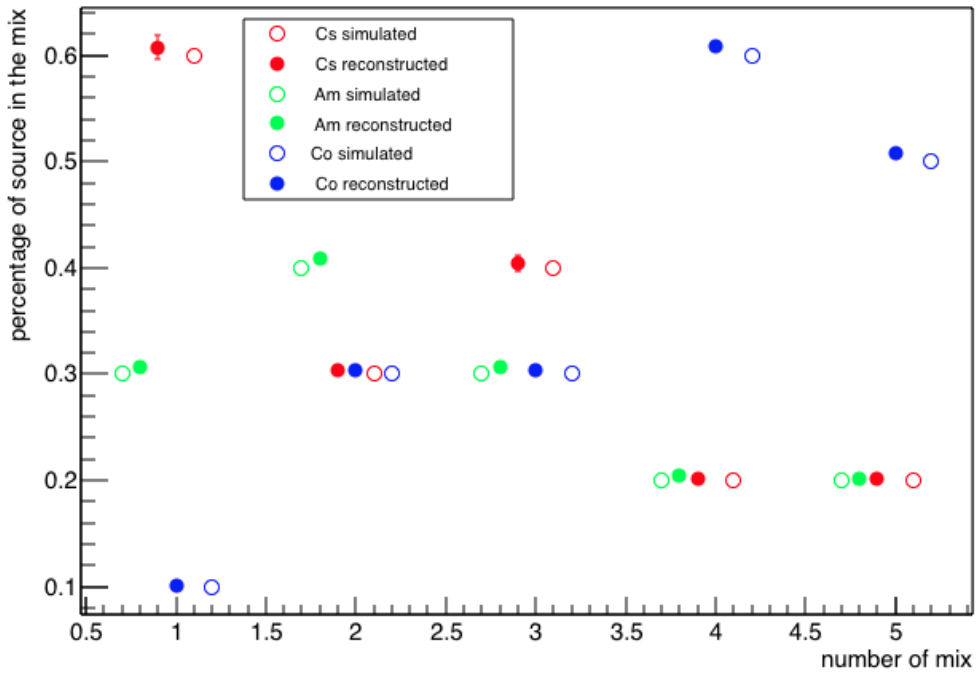

Figure 4.23: Comparison between simulated and reconstructed value for each source (Co, Am and Cs) and mix.

Na. The amount of Co photons was kept constant at 2000 and the amount of Ga and Na was varied. The mixes are summarised in table 4.8.

Figure 4.24 shows the fit results for all the different mixtures summarised in table 4.8. The red line represents the fit result for the Co source, which was kept constant in all the simulation. The fit results are:

$$y = 0.01042(\pm 0.02526)x + 2067(\pm 330) \tag{4.2}$$

The intercept on the y axis is 2067±330, in good agreement with the simulated value of 2000. The reconstructed amount of Co is not dependent on the amount of the other isotopes in the mixture and nor on the total amount of simulated photons. The open markers represent the simulated values of Ga and Na and the filled markers the reconstructed values. In figure 4.25 the differences agree really well between the simulated number of photons and the reconstructed number of

total	Co sim	Co rec	Co error	Ga sim	Ga rec	Ga error	Na sim	Na rec	Na error
13000	2000	2240.7	936.023	8000	8146.48	494.084	3000	3420.62	735.883
15000	2000	2238.8	947.151	8000	8264.71	498.57	5000	4598.39	740.349
18000	2000	2313.19	1001.8	8000	8221.89	511.168	8000	8046.3	789.314
23000	2000	3062.45	1084.83	8000	8340.54	527.25	13000	12386.6	873.521
11000	2000	1234.4	864.597	8000	8352.68	476.689	1000	1229.17	675.255
10500	2000	2504.95	839.017	8000	7603.63	460.538	500	649.061	658.012
15000	2000	2139.45	1012.67	10000	10113.4	541.236	3000	3524.97	792.86
17000	2000	2186.68	1053.89	10000	10508.2	561.545	5000	5041.68	822.421
20000	2000	2557.23	1074.4	10000	9467.65	545.916	8000	8616.99	849.318
25000	2000	2299.45	1152.67	10000	10313.6	575.237	13000	12760.3	917.363
13000	2000	2209.63	927.729	10000	9571.62	513.072	1000	1242.05	722.628
12500	2000	1922.04	910.613	10000	10208.1	515.239	500	164.941	707.809
17000	2000	2394.73	1057.05	12000	11486.2	566.111	3000	2756.56	831.39
19000	2000	2353.89	1111.76	12000	12085.6	587.482	5000	4765.88	873.654
22000	2000	2295.05	1174.82	12000	12328.1	608.026	8000	7889.02	925.905
27000	2000	1906.81	1231.49	12000	12224.7	621.746	13000	12886.8	976.884
15000	2000	2159.17	1023.38	12000	12532	580.615	1000	892.625	791.157
14500	2000	2298.91	1004.66	12000	12085.1	563.624	500	421.802	784.446
11000	2000	2227.85	833.021	6000	5981.28	425.81	3000	3245.06	662.125
13000	2000	2642.03	877.476	6000	6279.74	446.26	5000	5325.17	692.295
16000	2000	2542.09	929.399	6000	6235.29	447.082	8000	7307.49	752.633
21000	2000	2576.74	937.821	6000	5783.77	452.199	13000	12767.1	758.849
9000	2000	2347.71	759.422	6000	6101	414.825	1000	664.975	593.814
8500	2000	2532.37	737.228	6000	5873.62	408.071	500	465.005	572.461
9000	2000	1857.49	701.717	4000	3815.23	344.703	3000	3170.57	564.327
11000	2000	2792.23	800.767	4000	4114.02	369.142	5000	5074.29	660.918
14000	2000	2241.58	804.247	4000	4001.41	370.703	8000	7872.63	664.478
19000	2000	1905.07	850.136	4000	4250.22	396.285	13000	12718.5	702.932
7000	2000	1883.13	673.545	4000	4091.53	343.293	1000	806.337	540.054
6500	2000	2279.49	649.643	4000	4109.98	348.314	500	262.429	513.044
7000	2000	1987.19	594.93	2000	2169.26	276.768	3000	3343.32	487.67
9000	2000	2201.79	649.378	2000	2283.49	290.038	5000	5420.68	541.91
12000	2000	1931.33	624.293	2000	2085.81	282.044	8000	7717.31	525.015
17000	2000	1824.63	655.451	2000	2105.44	291.292	13000	13431.6	571.915
5000	2000	1897.88	520.935	2000	2139.08	264.366	1000	698.838	416.093
4500	2000	2439	534.033	2000	1951.97	247.419	500	417.62	441.549

Table 4.8: Different mixtures combination of Co, Ga and Na. The amount for each source is specified as well as the total amount.

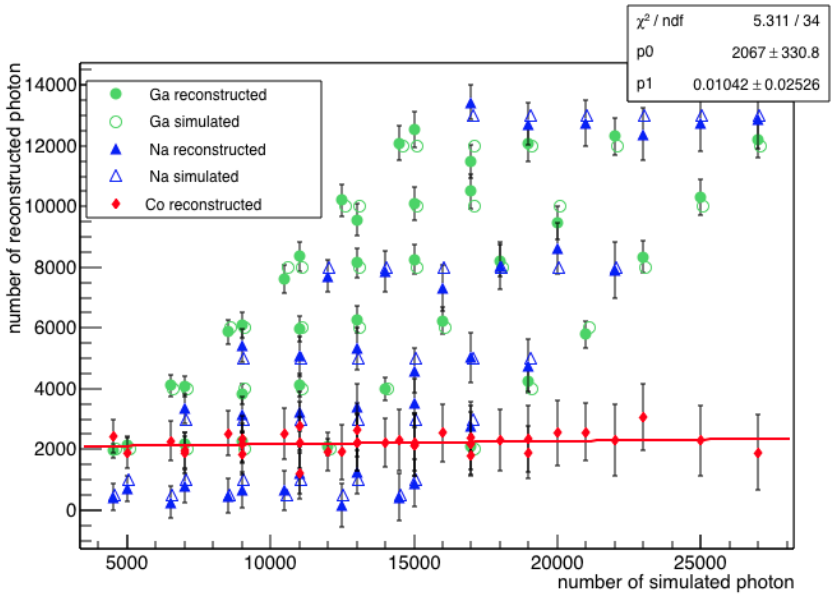

Figure 4.24: Number of reconstructed photons as a function of the number of simulated photons for different mixtures of Co, Ga and Na.

photons for Ga and Na are shown. The reconstructed values agree really well within errors.

This proves that the amount of photons and the combination of sources with different amounts or same amounts of photons do not influence the reconstruction processes. The time to recreate the accumulation plot depends on the amount of radioactivity present in the area under study, so it is not possible given a specific amount of time. The analysis can takes few second in very high radiation environment and the count limit is given in table tab:source. The fit applied is a multi parameter fit and the covariance matrix was taken into account. The number of collected photons in each beam are independent, indeed the integral does not depend on the previous bin value.

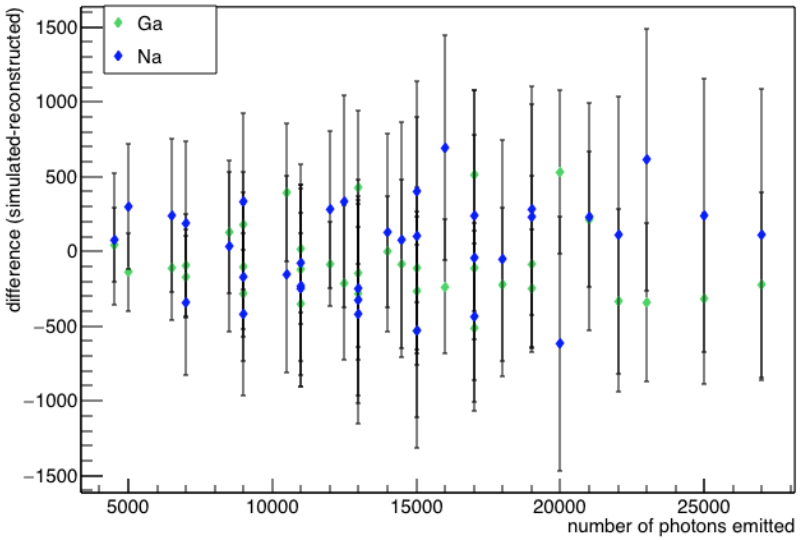

Figure 4.25: Different combinations of Co, Ga and Na.

4.5 Supporting studies

The possible uses of the system described in this thesis are different: it can act as a standalone radiation sensor or as a portable detection system or mounted on moving vehicles (flying or moving on terrain). Some of this uses may require the system to be placed close to the human body (such as in back-pack detection systems) therefore it is important to study the influence that the water might have on the detection performance of detectors. Similarly, it is interesting to study how the system performance is influenced by the distance between the source and the collecting detector. In this appendix simulations aimed at the study of these two situations are presented and briefly discussed.

4.6 Propagation in Water and air

The air is usually the main material in which particles travel before reaching the detector. If the detector is placed in a backpack, particles need to pass through the human body before reaching their final point, thus travelling through a medium with rather different composition than air. In this case, it is important to study the influence that the medium might have on the particle detection system. The density of the air is 0.00120479 g/cm^3 at 20° at sea level, while the density of water,

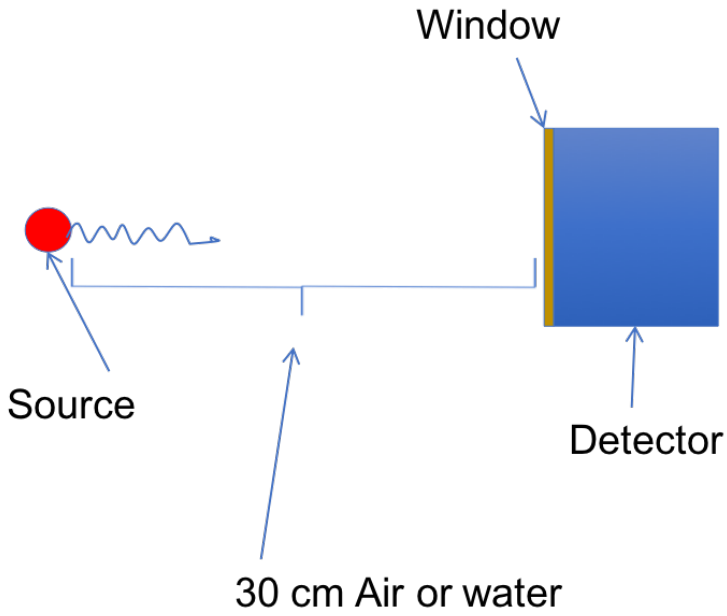

Figure 4.26: Geometry of the simulation.

the main component of the human body, is 1 g/cm^3. This difference induces a difference in the number of particles that are able to reach the detector. Moreover, the number of the secondary particles that are being produced is different. The simulations were carried out with GEANT4 with the geometry shown in figure 4.26. Two different configurations were considered. In both cases the detector was located 30 cm far from the source. The gap between the source and the detector was filled with air in one case and with water on the other case.

Figure 4.27 shows the energy deposited in a 2 mm CdZnTe detector by 10^7 photons emitted by a Cs source located 30 cm far away from the detector. Two different mediums between the source and the detector were considered: water and air. Considering the air the number of event collected in the photopeak is 522912±723 and total amount of interacting photons in the detector is 1248578±1117. After traversing water the photopeak is lower and the number of collected photon at the photopeak energy is 40168±200, approximately the 8% less compare to air. The Compton edge is also lower and other structures appear at lower energy due to the interaction with water and the consequent emission of secondary particles. The total amount of the collected photons after traversing water decreased to

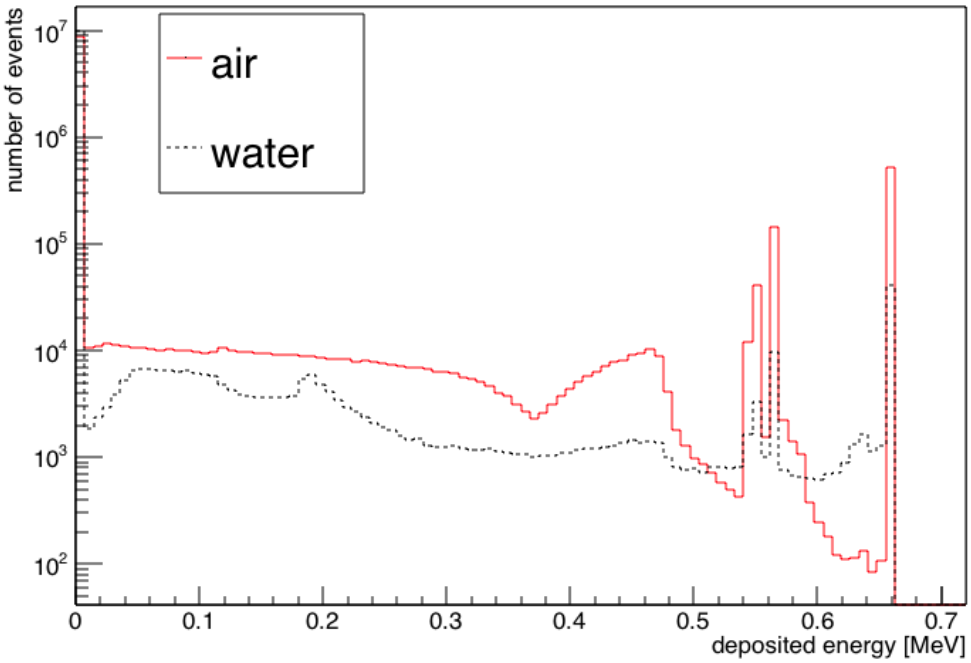

Figure 4.27: Spectrum of the energy deposited by 10^7 photons emitted by a Cs source in a 2 mm thick CdZnTe detector. The medium between the source and the detector was filled with air and water to simulate a human body.

265544±515. Although the water results in a reduction of the number of events, these simulations have shown that the photo peaks are still at the same location and still pronounced and thus the efficient detection of the source is still possible.

4.7 Distances

In this section the number of events collected at different distances is considered. The emitted source considered was a ^{137}Cs with a beam made by 10^7 photons emitting to the direction of the detector. Figure 4.28 shows the results obtained when 3 different distance values were considered. The source was located at 25 cm, 2 m and 4 m far from the detector and the gap between the source and the detector was filled by air. The number of events which deposits energy in the photopeak range decreased with the distance, indeed at 25 cm it was 522331±722, at 2 m was 513797±716 and at 4 m was 504558±710. Figure 4.29 shows the total number of photons which deposited energy into the detector at different distances. The position of the detector was varied in order to produce a distance, between

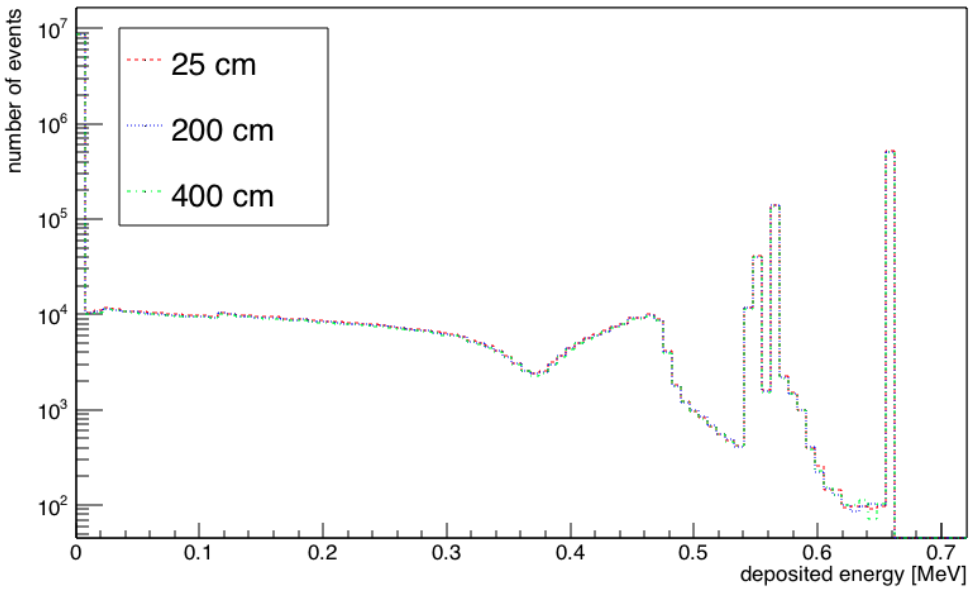

Figure 4.28: Energy deposited by 10^7 photons emitted by a Cs source in a 2 mm thick CdZnTe.

the source and the detector, of 10 cm to 5 m. The total number of event decreased with the distance.

The same study was repeated considering water as a medium between the detector and the source and the result is shown in figure 4.30. In this case the number of events decreases faster due to the attenuation of the water.

The number of photons in the photopeak and the number of total events collected depend on the medium in which the photons are travelling and are also strongly dependent on the distance at which the detector is located. If only air is present between the detector and the source, the fingerprint is still possible, indeed the number of photons collected is still enough to implement the threshold technique. On the other hand, if water is considered as filling medium, the detector has to be placed closer to the source to make possible the identification and amount reconstructions.

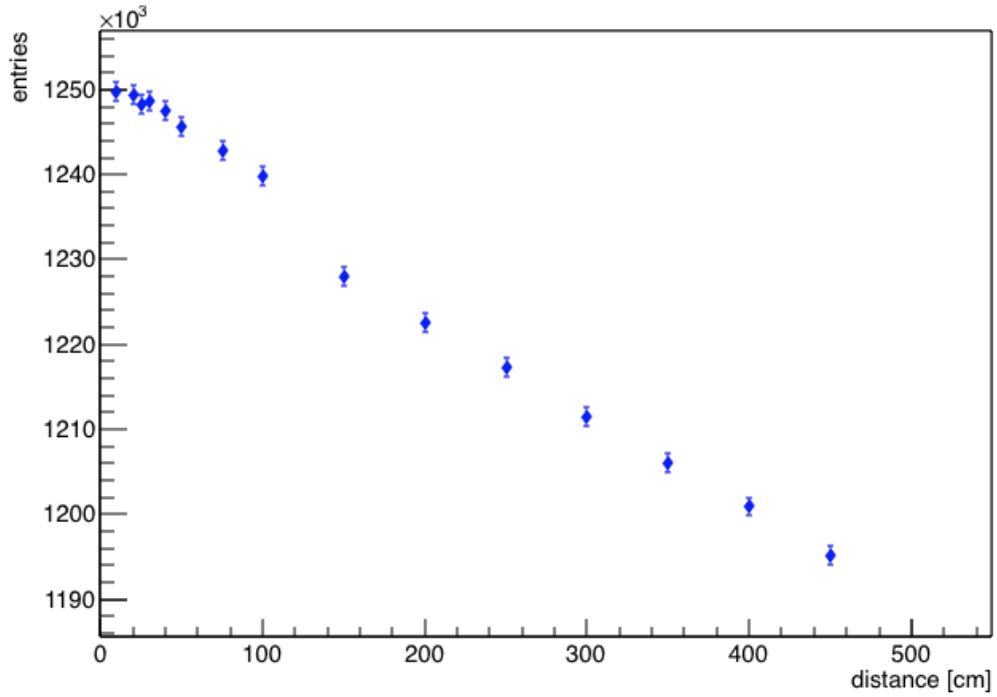

Figure 4.29: Energy deposited by 10^7 photons emitted by a Cs source in a 2 mm thick CdZnTe.

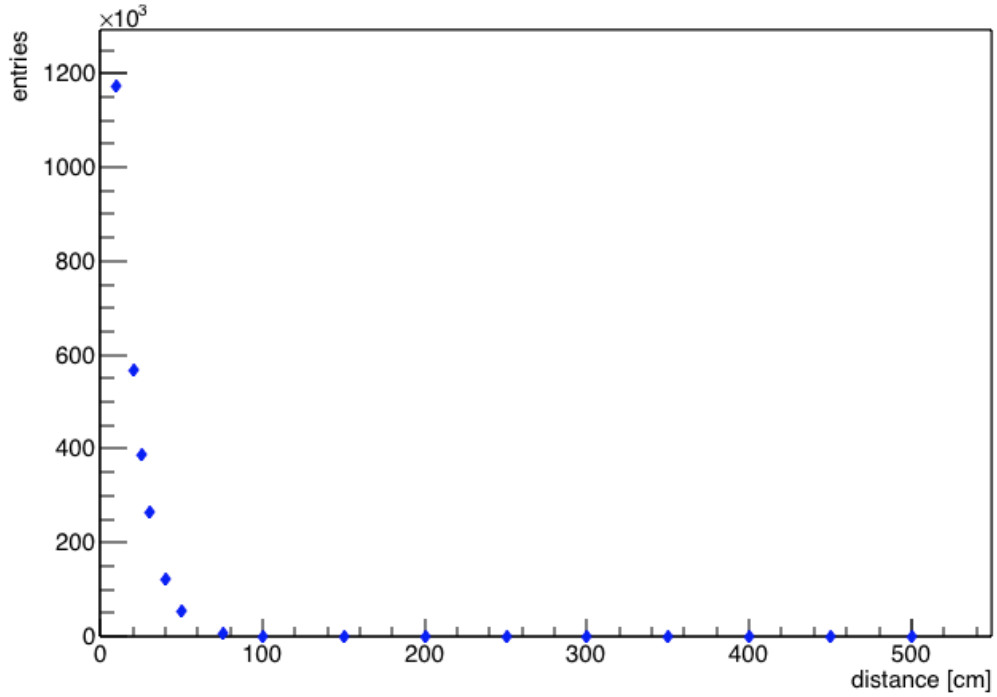

Figure 4.30: Energy deposited by 10^7 photons emitted by a Cs source in a 2 mm thick CdZnTe at different distances. The medium between the detector and the source is water.

4.8 Conclusion

The ability to identify different isotopes present in specific radioactive environments is important for security, decommissioning and health safety reasons. Recent decommissioning activities and nuclear accidents have highlighted the need of lightweight, easy to use detection tools, that will enable authorities and companies to build radiation maps of radioactive sites with different shapes and sizes. Semiconductor detector materials offer a unique opportunity to address such needs, mainly thanks to their physical properties and detection capabilities. In this chapter a novel multi-detector system has been described. This system allows the identification of a variety of radioactive isotopes using a very small number of events, thus enabling a detailed mapping with reduced measurements times. The proposed technique is based on the difference in the number of events around the different photopeaks observed by the detector. Using the analysis method presented in here it is possible to identify the source and measure its quantity. The proposed reconstruction method has the ability to work with single or multiple sources. The identification is not affected by the presence of other sources and their quantities. The proposed thresholding system will allow to operate in much higher maximum rate environments than existing spectrometers without compromising performance for low rate environments. This is key when mapping areas around for example nuclear power plants where rates can differ dramatically over very short distances.

Chapter 5 | Readout electronics and Muon Tomography

In order to store and analyse signals produced by the detectors various electronic processing functionalities have to be realised. The signal charge, in semiconductors is quite small (50 aC for 1 keV x-rays) and consequently, the signal has to be amplified. The signal generated is subject to statistical fluctuations and electronic noise. Specifically, the generated analog signal needs to be amplified (enhancing the signal to noise ratio) and digitally converted allowing for further processing using conventional computer machines.

The readout scheme adopted in this work is shown in figure 5.1. The readout board can be conceptually divided in two different sections, as shown in figure 5.1: the amplification stage and the storage and readout stage. The amplification stage is composed of a preamplifier unit (A250 Amptek charge sensitive preamplifier) followed by a high gain amplifier (ADA4860-1 operational amplifier). The A250 is a component that was specifically designed for semiconductor detectors, displaying an ultra low noise (<100 electrons) performance and a fast rise time (2.5 ns at 0 pF). The power consumption is also relatively low (19 mW). The ADA4860-1 is a low cost, high speed current feedback op-amp. Due to its performance (800 MHz, -3 dB bandwidth and 790Vμs slew rate) it is suitable for high speed applications. The supply current is 0.25 mA. The readout stage consists of two different units: the MAROC3 chip [53] and the FPGA. The MAROC3 consists of 64 different channels equipped with low impedance preamplifiers, trigger signals provided by bipolar fast shapers, and 12 bit Wilkinson Analog Digital Converter (ADC). The Wilkinson ADC uses a combined peak detector/pulse stretcher to acquire the signal amplitude, which is transferred to a memory capacitor. The time necessary for

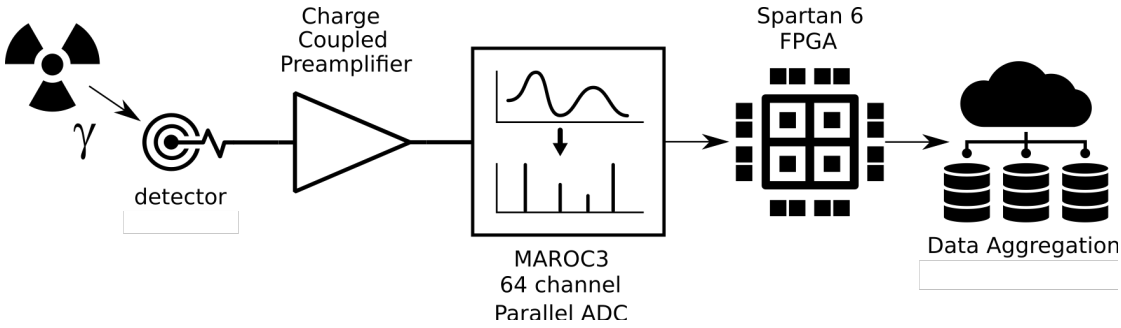

Figure 5.1: Sketch of readout chain. γ's generated by a radioactive source interact with the detector depositing resulting in the generation of charge. The detector is connected to a charge-sensitive preamplification/amplification stage connected to a MAROC3 chip. The MAROC3 chip converts the signal using an ADC and the signal is than collected and stored in the FPGA to be analysed and transferred to an external processor.

the capacitor to discharge is a linear function of the pulse height; the digitised pulse height is provided by the counter content. The counter is located on the MAROC3 board chip, and provides the number of pulses with the same height collected. The MAROC3 unit is interfaced with the FPGA board, which stores the incoming data from the detector and processes them to provide a readable output to the user. The FPGA system with 5 MAROC3 chips connected to it consumes approximately 1 A.

5.1 Signal processing chain

The design of the readout chain of a semiconductor detection system crucially contributes to its performance, thus determining the signal to noise ratio characteristics of the final system.

The signal processing chain is composed of two main functional blocks: the amplification stage and the readout chain. Figure 5.2 shows a sketched representation of the chain while figure 5.3 schematically shows how the different stages of the processing chain alter the signal shape and characteristics First of all, the radiation is absorbed by the sensor which converts the deposited energy in an electrical signal proportional to the deposited energy. The applied electric field moves the charge carriers to the electrodes inducing an electrical current. The integration of

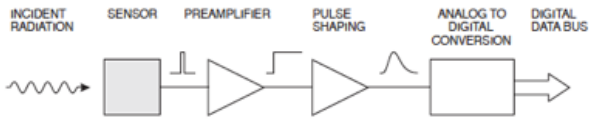

Figure 5.2: Component of readoud chain for semiconductor material [54].

the signal current provides the signal charge, which is related to the number of electron hole pairs generated and therefore to the deposited energy. To improve the signal to noise ratio a pulse shaper is added to the readout chain.

Figure 5.3 schematically shows how the different stages of the chain shape the signal shape. The first unit is a charge sensitive amplifier (preamplifier) that produces a voltage output proportional to collected charge. This amplifier transforms the δ-like pulse arriving from the sensor in to a step impulse with a long-tail. The step is fed into a CR high pass filter and a RC low pass filter which produced a nicely shaped pulse. The peak height is sampled and converted in discrete digital steps using an analog to digital converter (ADC) on the MAROC3 [53].

The noise level of the readout board, and detector, has an important role on the design of the board itself and to the signal acquisition. Noise depends from several factors: device type, manufacturing processes and also the operation condition such as temperature and intensity of the light. The first source of noise is given by the random motion of the charge carriers due to thermal excitation. The internal noise sources are described by Nyquist equations:

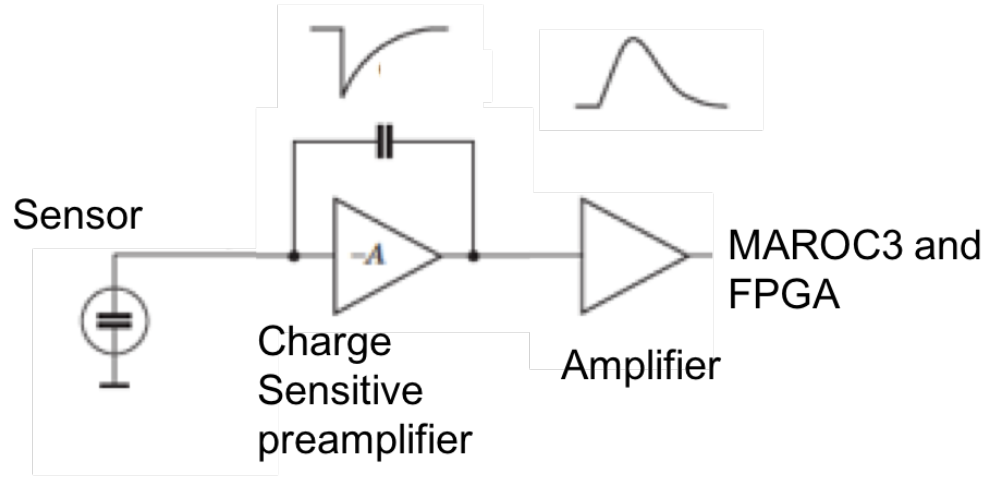

Figure 5.3: Readout chain and sketch indicating the signal shaping process.

$$\begin{aligned} \bar{v_{th}^2} &= 4kTR\Delta f \quad \text{for voltage} \\ \bar{i_{th}^2} &= \frac{4kT\Delta f}{R} \quad \text{for current} \end{aligned} \tag{5.1}$$

where R is the corresponding resistor is parallel, for current source, or in series , for voltage source; T is the absolute temperature, k the Boltzmann constant. and Δf the frequency bandwidth. The mean voltage and current noise are proportional to $\sqrt{\Delta f}$ and it is associated to each resistor in the circuit. The fluctuation of the number if charge carriers due to the presence of recombination and generation centres is another noise source, which can be modelled as:

$$\frac{S_{g-r}(f)}{N^2} = \frac{\left(\bar{\Delta N}\right)^2}{N^2} \frac{4\tau}{1+(2\pi f\tau)^2} \tag{5.2}$$

where τ is the carrier lifetime and $\left(\bar{\Delta N}\right)^2$ the variance of the number of carriers N. The readout board consists of the MAROC3 chip and an FPGA unit.

The MAROC3 chip has a 64 channel discriminator producing 64 corresponding trigger outputs.Initially, the MAROC3 system, used in this thesis project, was created for muon tomography project at Bristol University. By programming the MAROC3 channels with different discriminator values, each channel can be set to trigger at a different pulse height. When (at least) one input goes over threshold and thus triggers the readout out, the results of all 64 comparators generated by the

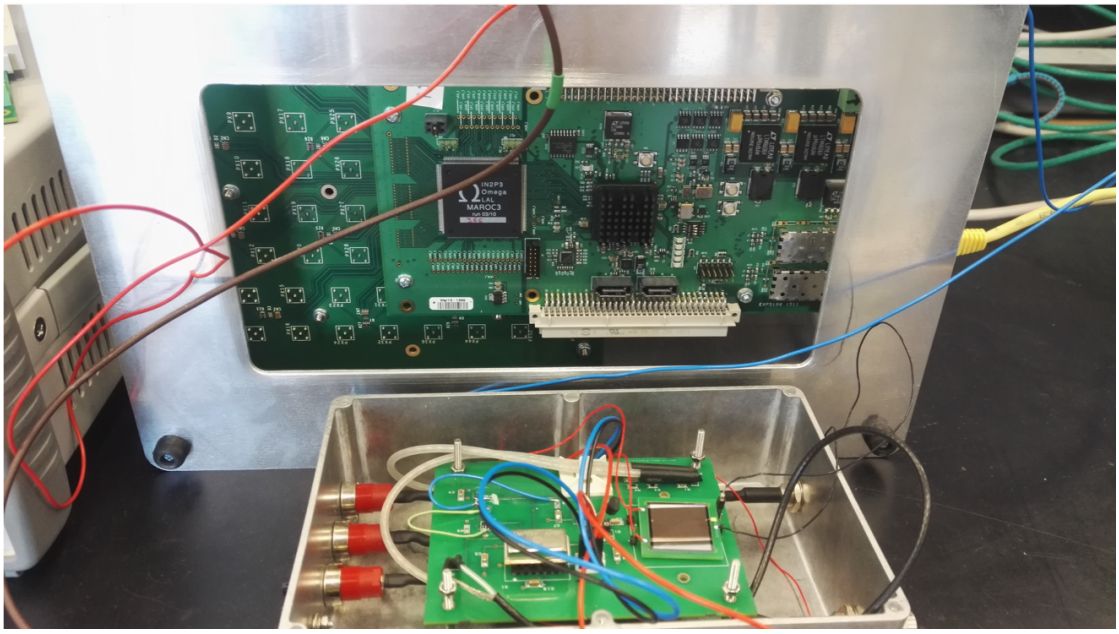

Figure 5.4: The complete system. At the bottom the preamplifier board with a 500 μm thick Si detector on top. On the top the single MAROC3 board is shown
.

MAROC3 is collected and processed by the FPGA system and then transmitted to the PC via an ethernet cable [55, 56]. The data are then collected using LABVIEW code which generates a binary file. The file is than analysed using the technique presented in chapter 4.

The complete system, including the Si detector and the signal processing chain is shown in figure 5.4. The electronic board was 10 cm$\times$ 10 cm; while the readout board considering the MAROC3 chip system and the FPGA was 22 cm $\times$ 15 cm. In the top part of the picture the MAROC3 and the FPGA are visible. At the bottom side, the square 500 μm thick Si detector is placed near to the high voltage connectors. The A250 is visible on the top left side, close to the end edge of the board. The board was placed in an aluminium box to reduce the effect of any external noise.

The amplifier board was specifically designed in house. Two different amplifier boards were designed, fabricated and tested: a single channel board and a multi-channel board, with 64 different output signal. The schematics of the two boards (single and multi-channel) are shown in figure 5.5 and 5.6, respectively.

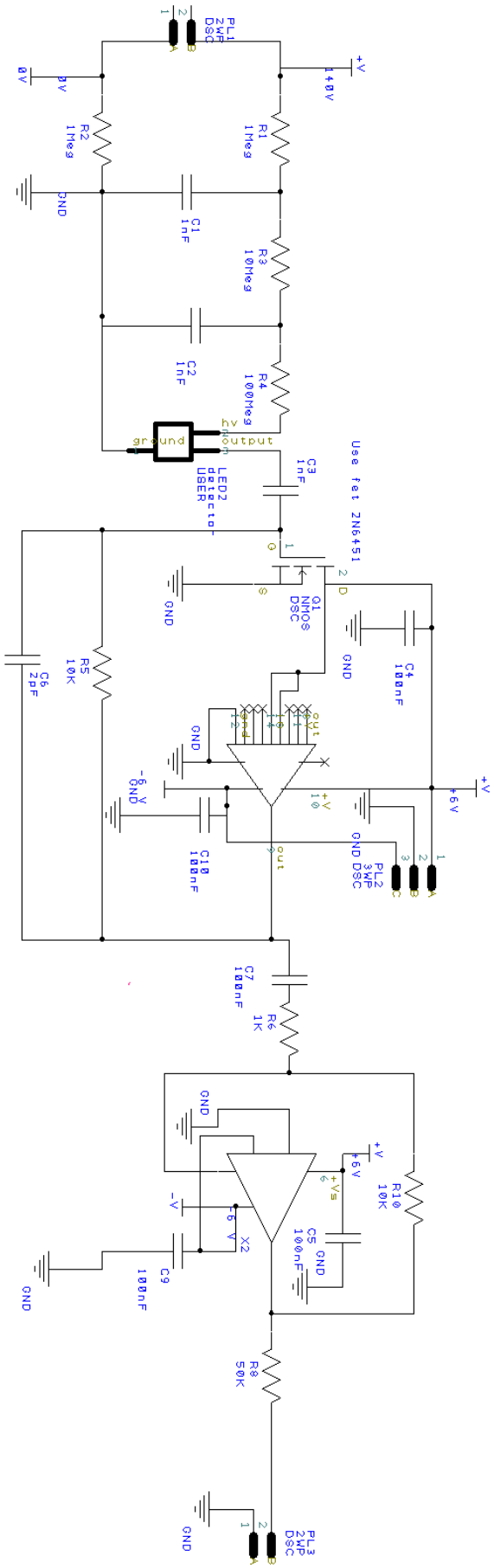

Figure 5.5: Schematic of the board with a single output.

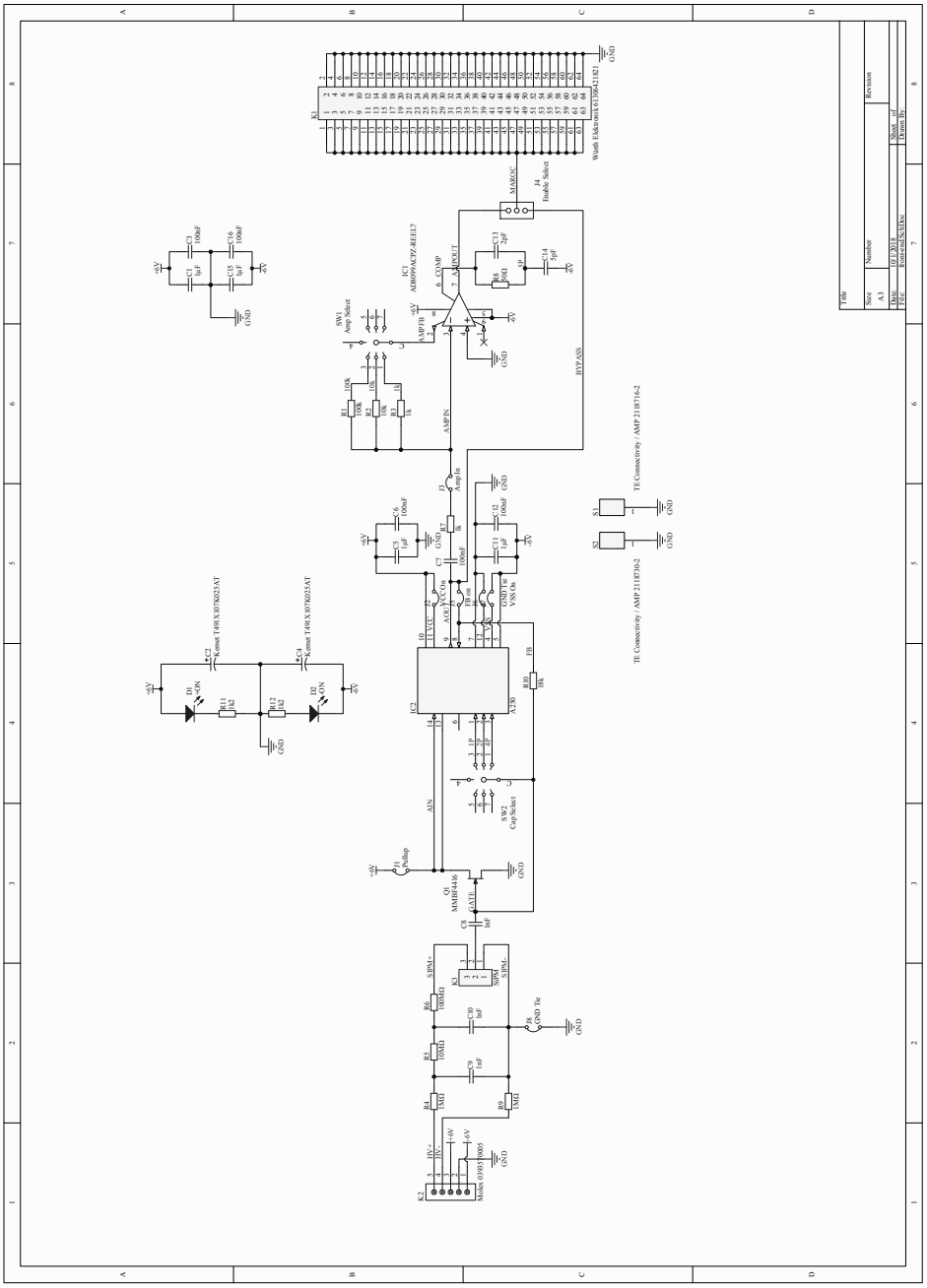

Figure 5.6: Schematic of the board with 64 output channels.

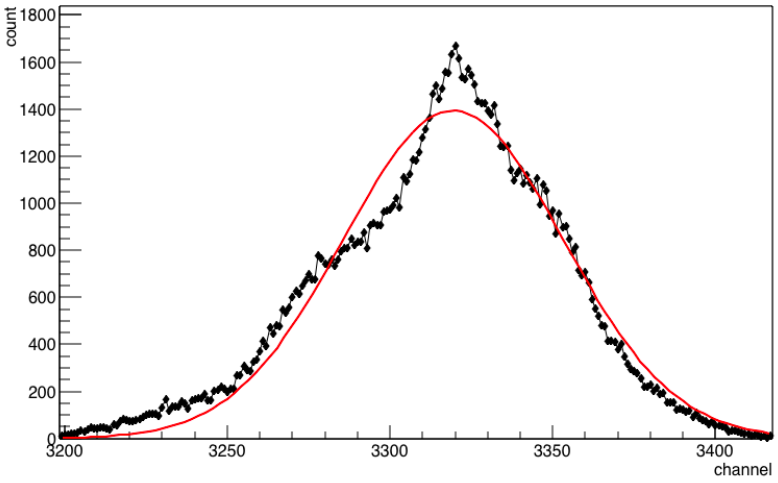

Figure 5.7: Measured board response when a 10 pF capacitor is connected to the board to simulate detector and 15 mV pulses are injected into the capacitor. In red the Gaussian fit.

5.1.1 Single channel board test results

The single channel board was tested using a 10 pF capacitor acting as a charge generator. The injected voltage was varied between 10 to 30 mV. The board was connected to a MCA to measure the board's output. The measured output spectrum using an MCA for a 15 mV input pulse is shown in figure 5.7. The measured signal distribution is wider than the actual output of the board [53]. Reflections generate the weird shape between 3250 and 3300. The spectrum is centred at 3319 channel with a sigma of 33.82. The signal is spread across approximately 200 channel. Between 3250 and 3300 a shape over the signal shape is visible.

Figure 5.8 shows how the mean output varies with the input pulse amplitude. The response is linear up to an injected pulse amplitude of 15 mV, corresponding to injecting a charge of about 62.5k electrons. For comparison the most probably charge generated by a minimum ionising particle traversing a 500 μm thick silicon sensor is approximately 40k electrons. Hence, the linear region extends will above the largest signals we may expect. Above 15 mV the signal begins to saturate. Figure 5.9 shows the result for the data between 10 and 15 mV. The results are fitted with straight line.

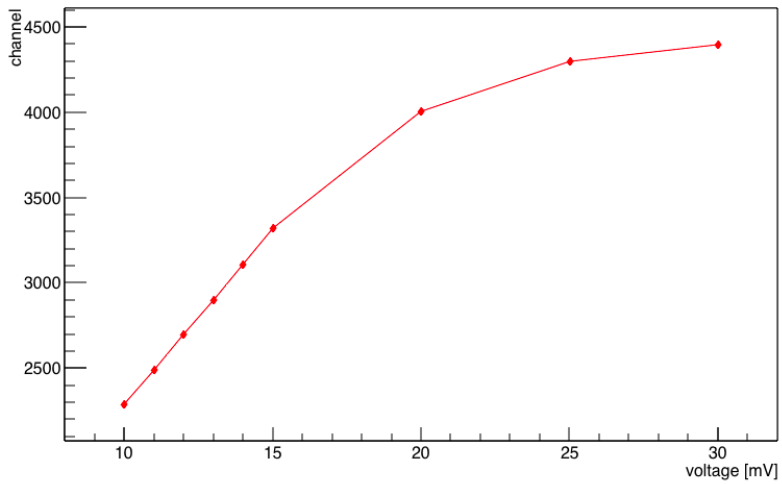

Figure 5.8: MCA board response when a 10 pF capacitor is connected to the board to simulate detector. The injected charge was varied from 10 mV and 30 mV.

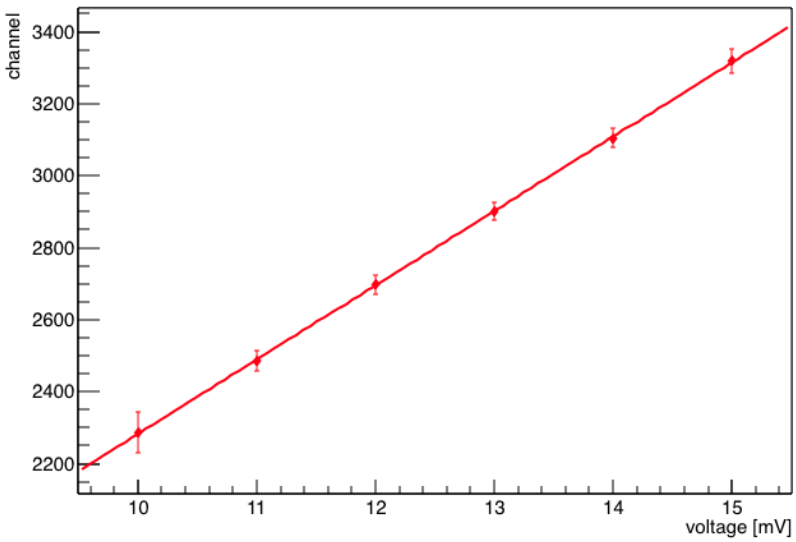

Figure 5.9: MCA board response when a 10 pF capacitor is connected to the board to simulate detector.

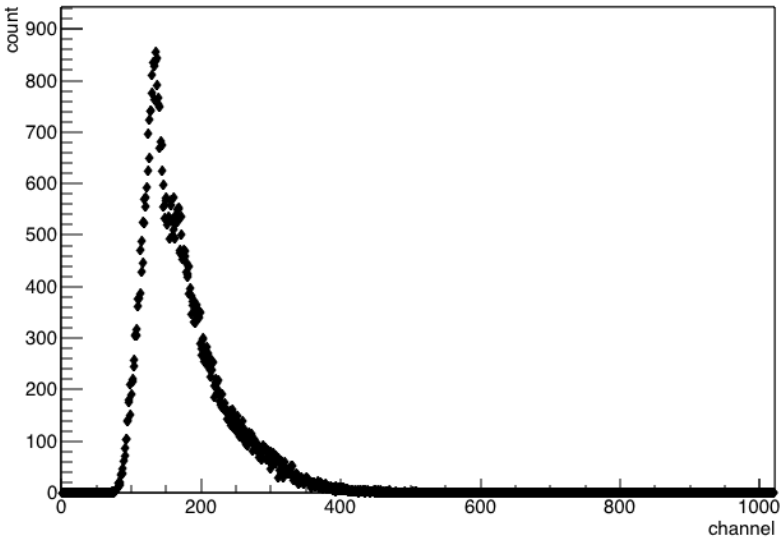

Figure 5.10: MCA response when a 500 μm thick Si detector is connected to the amplifier board.

The board was then tested with a 500 μm Si detector, with a bias voltage set at 70 V which was well above its full depletion voltage of 60 V. An ^{241}Am source was placed at approximately 5 cm distance from the detector surface.

Figure 5.10 shows the output spectrum of the MCA without the α source being present. Figure 5.11 shows the output spectrum of the MCA with the α source being present.Figure 5.11 clearly shows the presence of the α source around 238 ADC counts. The slight shift in pedestal is caused by a minor light leak. These tests confirmed the correct functionality of the various electronic components.

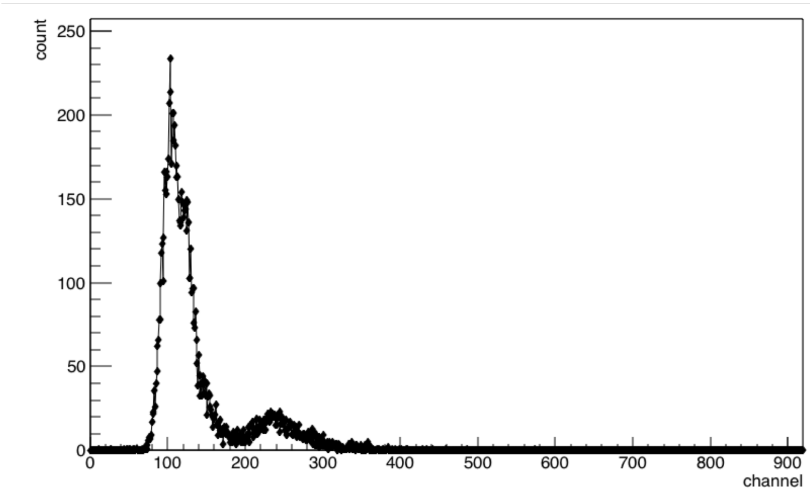

Figure 5.11: MCA response when a 500 μm thick Si detector is connected to the amplifier board and the Am source is placed 5 cm far from the detector surface.

5.2 Muon tomography

Muon tomography is a reconstructing imaging method that exploits cosmic rays. Muons are highly penetrating particles, potentially capable to travel hundreds of meters through the Earth. Depending on the atomic number (Z) of the interacting medium the muons are scattered by different amounts and can be absorbed as well. Thanks to this properties they could be used to reconstruct a 3D object by developing a proper detecting system. University of Bristol is involved in two different applications: identification of mine internal structure and analysis of container to check the presence of nuclear waste. During my PhD, I actively participated on a project based on muon tomography to identify the internal mine structure. The project was developed in tine mine in Geevor, Cornwall.

5.2.1 Geevor system

In order to efficiently detect muons, Resistive Plate Chambers (RPCs) have been chosen because their high efficiency, good spatial and time resolution and a low cost per area.

The RPCs are formed by two glass plates forming a gap, as shown in figure 5.12. This gap (here 2 mm wide) is filled by a gas mixture composed of 95% Freon and 5% Isobutane.

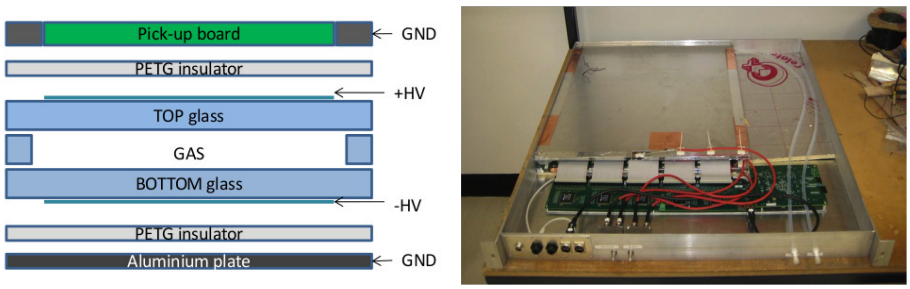

(a) (b)

Figure 5.12: In (a) is shown a structure of single RPC in all components. In (b) a picture of RPC built in Bristol laboratory is presented.

To verify muon tomography concept two different experiments have been performed.

The first experiment has been performed in the Physics Laboratory at University of Bristol, in which 14 RPCs were set in vertical position to detect a steel block, placed in front of them. This preliminary experimental session was aimed to test the functionality of our system, which has then been placed in Geevor, to detect the 2D shape of a real mine.

The system is composed by 14 RPCs (Fig:5.13) with a total length of about 2400 mm and an active area of 500 mm $\times$ 500 mm to cover an angle of 24°. Two scintillators supply trigger signals.

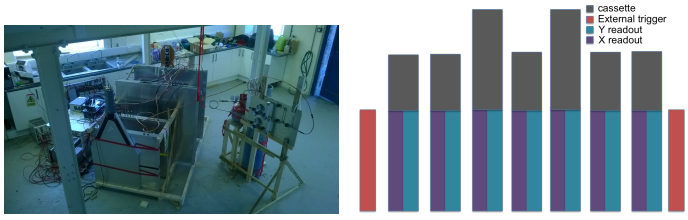

(a) (b)

Figure 5.13: In (a) a picture of Geevor setup is presented. In (b) is shown the structure of cassettes and where trigger scintillators are located.

In order to calibrate the detection system we collected muon rate data coming from the sea direction (at zenith angle, without any object facing the detector)

and from the side facing the mountain (again at the zenith angle). Results are shown in figure 5.15, showing different muons rate for those two different cases, confirming the functionality of our system.

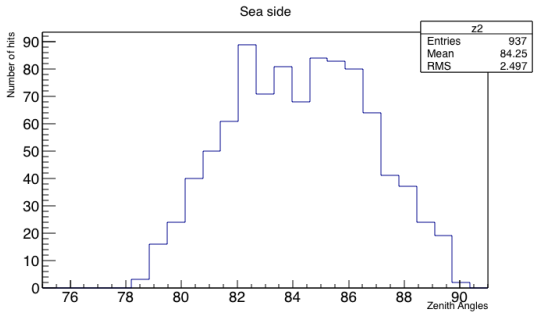

(a)

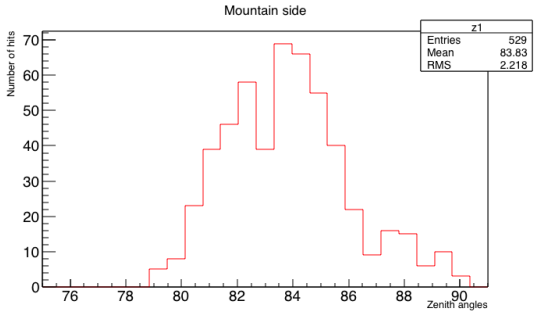

(b)

Figure 5.14: Muons rate data for (a) sea side case and (b) mountain case.

Preliminary results are shown in figure 5.15. In figure 5.15.a and figure 5.15.b are shown examples of hit position as a function of z coordinates (vertical one); due to different signs of angular coefficient it is to possible to assess the particles direction (basically two directions are considered, mountain and sea side). In figure 5.15.c is shown an example of signal to noise ratio trace that exhibits comparable results with respect to what already shown in [55], [56].

To prove the validity of muon tomography system we placed it in Geevor mine from April 2015 to August 2015. The data analysis showed some interesting result but the acquisition time was not enough to get good resolution and to perform a good data analysis.

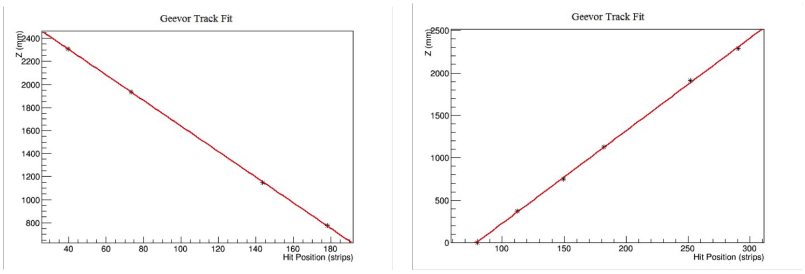

(a) (b)

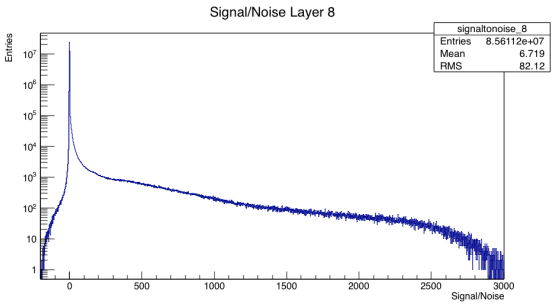

(c)

Figure 5.15: In (a) and (b) two particle tracks are displayed. In (c) an example of signal to noise ratio is shown.

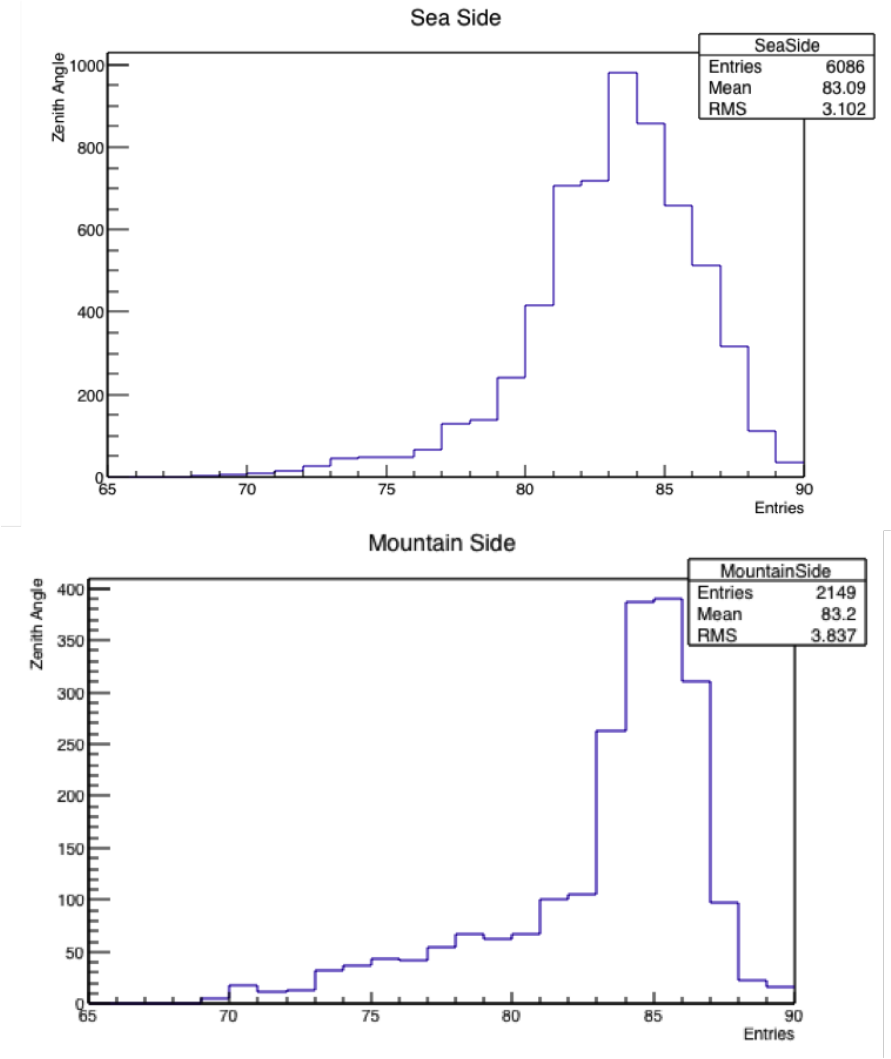

Figure 5.16: Comparison between number of muons per each side.

Chapter 6 | Future Studies and Applications

In this chapter and overview of the development of the system and future possible applications are given. The first part of this chapter is devoted to explain how the physical system can be improved and, consequently, the measurements suggested to obtain a working system. The second part of this chapter is going to explore the possible application of real system in different environments and where it can be used to enhance radioisotopes detection and identification.

6.1 Design Concept Options

The system design consist of a layout of 5 different semiconductor material. Several configurations can be considered to optimize the system for different application. First of all a matrix configuration can be evaluated. To cover a relatively high solid angle detectors can be placed on the same plane, as show in figure 6.1. In this way the radiation reach all the detectors at the same time and a comparison between the number of event collected can provide the value of source intensity and also the location of the source.

A different configuration can be considered with detectors placed in a vertical layout, as show in figure 6.2; this configuration allows a better energy selection in each detector, indeed to stop relatively high energy gamma thick materials are necessary but detector such as Silicon and diamond are not able to identify them

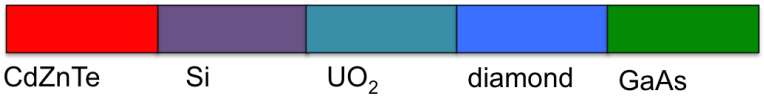

Figure 6.1: Detectors placed on the same plane to maximise the solid angle covered.

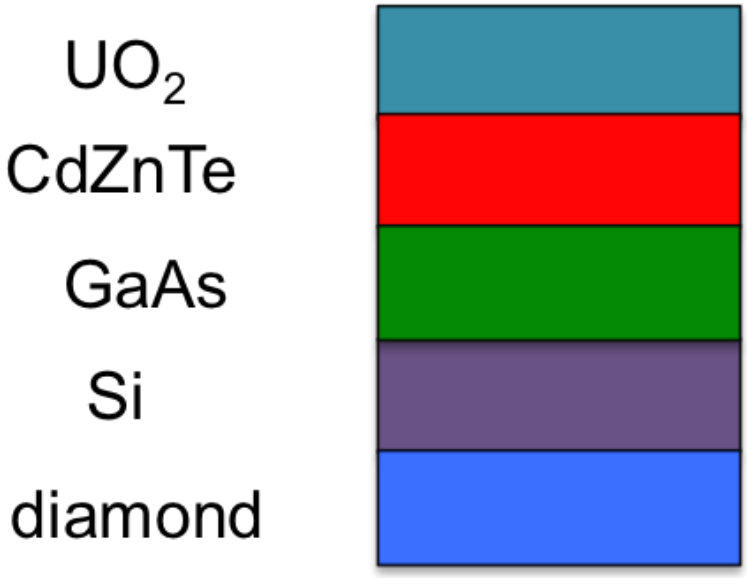

Figure 6.2: Detectors placed one on top of the other to select the energy in each detector.

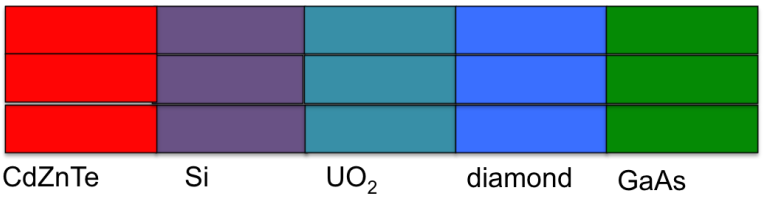

Figure 6.3: Mixture of configuration 1 and 2.

so they can be located as first and second detector in this layout to stop the lower energy photons, while other detectors can identify higher energy one.

Figure 6.3 shows the mixture of those two configuration, where the detectors are located on the same plane but they are also expanded in 3 layers in vertical plane. This configuration is beneficial for energy identification also in material such as Si and diamond, but also to identify the location of sources due to a tracking system based on where the interaction occurs.

In this perspective, different shape configurations can be considered, such as triangle shape as show in figure 6.4 which allows to identify the location of the sources.

The electronic location can also be considered, indeed it is important to have short cable to avoid noise amplification, but also some distance to avoid the temperature rising which can create problems on detectors performances. To avoid electronic radiation damage the electronic can be placed in an aluminium box, and so the

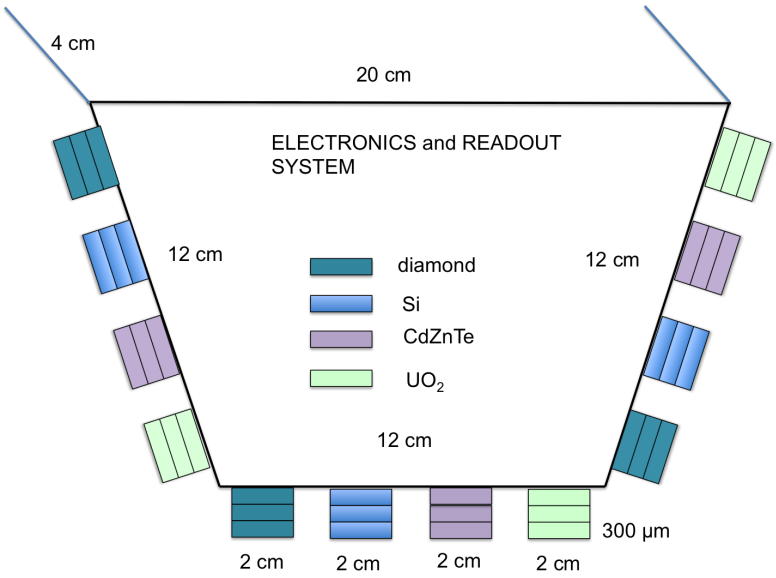

Figure 6.4: Triangular shape detector configuration without GaAs. In this configuration the detector can be swapped and added as required.

detector. To maximise the radiation interaction a kapton window can be placed in front of the matrix of the detector.

6.2 Measurements and Future Development

Simulations described in chapter 4.3 show the ability of the threshold technique to identify and evaluate the amount of sources. In real system this can be achieved using MAROC3 chips connected to FPGA to analyse and store the data. To prove the validity of the technique in real system several steps has to be be carried out. Each detector has to be tested and characterized. The first step consist of identify the IV curve of the detector to find the correct bias voltage; secondly the effect of the temperature must be evaluated to be able to scale the number of event collected with it, as shows in chapter 3. Detectors are then tested with well known sourcse to evaluate their resolution and their ability to identify the source; as first instance this measure can be carried out with an oscilloscope and then with a multi channel analyser. This measurement can be performed with the home made electronics proposed in chapter 4.8, to evaluate the electronic noise and the effect on signal shape. The subsequent measurement could be the identification of different sources thought their photopeak. To evaluate the detector sensitivity, sources wiith closer photopeak can be considered. This measurement it is important to identify the signal to noise ratio to create a better electronics. Once than the threshold level are defined using the MAROC3 chip, all the levels for the sources considered can be setted at the same time using the 64 different channels. A last stage, the full analysis can be implemented. The online analysis is made by the MAROC3 64 channels, while the data are stored and send to the computer using the FPGA board. The off line analysis can be done with ROOT software implementation to validate the data and the analysis performed online. The last implementation could be the introduction of the RF (radio frequency) system to send the data directly to a computer without a cable connection.

6.3 Further System Application

In the recent years, Unmanned Air Vehicles (UAV) have become popular tools in everyday life. Drones can be employed for many different applications: from

gaming to shipping. At the University of Bristol, they are employed as well for radiation detection. Several studies were performed after the Fukushima nuclear accident [57–61]. So far only simple counting was used to produce radiation maps. The experiments have shown that UAVs can also be deployed in areas where human presence is not possible. The system developed during this project does not only count but can also identify the sources and their amounts present in a specific location.

Since the system presented is light weight, rigid, robust and does not consume much power, it is suitable for UAV-based applications. Two options can be considered: quadcopter and airship. Both of those solutions have advantages and disadvantages. Quadcopters can be employed both outside and inside facilities, but due to the rotors they can move radioactive particles which might lead to false radiation measurements. If the radioactive particles are moved by the rotors the safety hazard for the operators can be underestimated, or in the case of nuclear waste, a source can be wrongly classified. On the other hand, an airship can be used only inside because it is too much affected by climate conditions such as wind. It can fly for weeks without any battery restriction, whereas a quadcopter typically has a battery life of only 40 minutes, depending on the model that is considered. Both options are restricted by the maximum weight they can carry: a quadcopter can carry up to 7 kg and fly for approximately 40 minutes before requiring recharging; an airship of 2×1 m^2 can hold up to 120 g plus the battery weight (250 g), which is quite restrictive. Furthermore, UAVs are kept at 2 m from the ground and the mapping can be performed using GPS combined with barometry, magnetometry and a laser range finder. Indoor studies are important during decommissioning. Some places might show high radiation levels and require a proper mapping to identify the dangerous spot. In indoor environments other techniques, such as LiDAR (a system based on pulsed laser light which illuminates the target point and measures with a sensor the reflected pulse) or optical flow sensing [62, 63], can be used to overcome the interference effects with the room walls and create

a map of the room. Rotor systems in indoor environments are subject to several drawbacks such as redistribution of contamination, confined space which enhanced the probability of collision, limited UAV size and consequently limited flight times due to lower maximum payload and hence small batteries.

Weight restrictions are an important issue when employing detectors on UAVs. The weight of the proposed electronics consisting of a readout board, a MAROC3 and an FPGA board is approximately 100 g. The weight and the size can be further reduced in a further design iteraction. The biggest restriction is represented by the high voltage (HV) supply that must be provided for the semiconductor detectors to work. In the quadcopter option the battery can be used to give the right amount of voltage necessary for the FPGA and readout board (12 V) and the detector bias voltage. Since the leakage currents are limited, the HV can be generated using for example Cockroft-Walton voltage multipliers, similar for the circuits used for photomultiplier. The current needed for the readout system is approximately 1.5 A. In this configuration the quadcopter can fly for approximately 20 minutes. The power needed by the system to work can be a problem with the airship, but now at Bristol University, diamond batteries are in development.

Chapter 7 | Conclusion

The first nuclear power plant was built at Obninsk (Russia) and was connected to the power grid in 1954. In 1956 in the UK, Sellafield, was the first operating commercial nuclear power plant in the world. During these 65 years, many other nuclear power plants plants were enabled around the globe. We have now reached the first nuclear decommissioning era and new reactors might replace the old ones that are (or will be soon) put in decommissioning. In order to perform such activity in a safe manner it is vital to be able to map the radiation levels and identify the isotopes present and their quantity. Hence, there is a clear need to develop fast and reliable tools that could undertake this task, while preserving the health and safety of the operators.

Due to their specific energy spectrum, gammas emitted during nuclear decays can be exploited for isotopes fingerprinting. The differences in gamma ray cross sections in different detector materials allow the identification of radioactive materials in high radiation fields. Semiconductor materials are considered one of the best option for this application. They have high Z numbers compared to gaseous detectors and thanks to their relatively high densities are able to stop a broad range of particles with different energies. Moreover, unlike scintillators they are lightweight and they can achieve comparable performance. Furthermore they can be seamlessly integrated with electronics, show good radiation resistance and are mass-producible with relatively low cost.

In this thesis a novel detection system was proposed and tested in a large Monte Carlo study. The results show that the system is capable of identifying the most common isotopes present in radioactive environments (such as nuclear power plants or radioactive accident sites). Specifically, 12 isotopes were considered, each of them emitting one, or more, gammas, thus generating photopeaks at specific, well

defined, energies. The differences in the number of collected photons, before and after the photopeak energy, allows for the source identification. The system implemented in here has been based on a novel threshold scheme along with the use of multiple semiconductors, thus allowing for the detection of a wide energy spectrum and reconstruction of the isotopes amount. The system comprised of 5 different semiconductor materials (Si, diamond, GaAs, CdZnTe and UO_2). The developed system is compact and future studies might be devoted to the full integration of it with a miniaturised signal processing board, thus making the full system portable and very lightweight. Preliminary studies have shown that the system is compatible with the most modern unmanned vehicle systems.

The threshold technique requires a low number of photons to perform a good isotope identification. The number of photon needed varies from source to source and detector by detector. For UO_2 and CdZnTe less than 2000 photons are required for sources identification, except for Ga source in CdZnTe, while for the other detectors the range is wider. This allow a fast identification response related to the activity of the source, or mixture, under study. The speed of the system is also enhanced by the MAROC3 chip which is designed to operate at 40 MHz. The high speed of the readout system and the signal pulse of few picoseconds provides excellent performance at very high counting rates, well exceeding the few 10s of kHz of traditional spectrometers, without comprising the device performance in low rate environment. The actual maximum counting rates will be determined in future experiments.

Appendix A | Signal generation and noise

A.1 Signal generation and acquisition

With reference to chapter 3, semiconductor detectors can be modelled as a parallel plate capacitor with a specific thickness L. The electric field can be considered constant across the material. The energy deposited (E) in the detector is related to the number of electron holes pair produced $n = \frac{E}{\epsilon}$, where ϵ is the energy required for the pair production. The ratio $\frac{\epsilon}{\epsilon_g}$ is constant and does not depend on the radiation type or energy. When the electric field is applied the produced electrons drift towards the anode while the holes towards the cathode, as briefly shown in figure A.1.

The current induced due to the motion of the generated carriers in the vicinity of the electrodes is described by the following equation [30, 35]:

$$i = \frac{dQ}{dt} = q\vec{v}\vec{E}_w \tag{A.1}$$

where $\vec{v}$ is the carrier velocity and $\vec{E}_w$ is the component of the electric field in the direction of v at the charge's instantaneous position, under the following conditions: charge removed, given electrode raised to unit potential, and all other conductors grounded [35]. When the energy is deposited the signal is created but the signal is fully recovered only when the last generated charge carrier reaches the destination electrode. Due to the trapping and recombination effects that are present in the semiconductor material the charge collection is characterised by an efficiency parameter, defined by the Hetch equation [30]:

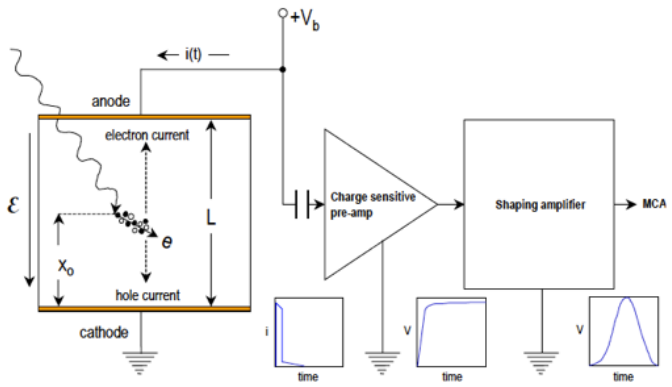

Figure A.1: Semiconductor detector material and its amplification chain. When the particle interacts with the material the electrons and holes produced during the process drift towards the cathode and anode respectively. The signal is transmitted to the preamplifier, shaper and finally to the amplifier.

$$CCE = \frac{Q}{Q_0} = \frac{\lambda_e}{L}\left[1 - exp\left(-\frac{L - x_0}{\lambda_e}\right)\right] + \frac{\lambda_h}{L}\left[1 - exp\left(-\frac{x_0}{\lambda_h}\right)\right] \tag{A.2}$$

where x_0 is the coordinate at which the charge is created, λ_e and λ_h represent the linear space that the charge carriers need to travel before being trapped or collected, for electrons and holes, respectively. As shown by the equation, the CCE depends on the point where the charge is created, i.e. the impact point of the particle with the material. The impact point in the detector is random and the width of the energy spectrum peak it broadens due to the exponential dependence. Relatively low change in the point of interaction generates a high difference in the charge collection efficiency; furthermore the energy peak is widened by this effect due to the collection time of the generated particles, related to the drift time.

A.2 Detector response spectral broadening

In a semiconductor system with a charge sensitive preamplifier read-out electronic system, the electronic noise sets the minimum threshold detection limit and determines the ability of the system in distinguishing different signal levels within the dynamic range of the apparatus. [64].

The noise it is an important characteristics of the device and it has to be taken into account during the design stages as it contributes to the definition of the energy resolution of the semiconductor detector.

A.2.1 Fano noise

The statistical variance of the energy peak is the result of various factors acting simultaneously. Firstly, the energy of the interacting particle (with the detector) can generate phonons via lattice excitation, or electron-hole pairs via ionisation processes. The total energy deposited E_0 is the sum of the energy deposited by excitation (E_{ex}) and ionisation (E_{ion}) as described by the following:

$$E_0 = E_{ion}N_{ion} + E_{ex}N_{ex} \tag{A.3}$$

where their variance expressions are given by $\sigma_{ex} = \sqrt{N_{ex}}$ and $\sigma_{ion} = \sqrt{N_{ion}}$, where N is the number of phonons and pairs produced during the interaction process. Considering a specific energy beam E_0, for a single event the deposited energy, within statistical variation, is constant. If $E_{ion}>E_{ex}$ some ionization and excitation processes release precisely the deposited energy E_0. Therefore , the fluctuation in excitation and ionization must be balanced

$$E_{ex}\Delta N_{ex} + E_{ion}\Delta N_{ion} = 0 \tag{A.4}$$

meaning that when more energy is directed towards the phonon generation process the available energy for the ionisation process is reduced. The variance in the number of ionisation it can be written as:

$$\sigma_{ion} = \frac{E_{ex}}{E_{ion}}\sigma_{ex} = \frac{E_{ex}}{E_{ion}}\sqrt{N_{ex}} \tag{A.5}$$

From equation A.3 the number of generated phonons can be expressed as $N_{ex} = \frac{E_0 - E_{ion}N_{ion}}{E_{ex}}$ and the equation A.5 ca be rewritten as following:

$$\sigma_{ion} = \frac{E_{ex}}{E_{ion}}\sqrt{\frac{E_0}{E_{ex}} - \frac{E_{ion}}{E_{ex}}N_{ion}} = \sigma_{ion} = \frac{E_{ex}}{E_{ion}}\sqrt{\frac{E_0}{E_{ex}} - \frac{E_{ion}}{E_{ex}}\frac{E_0}{\epsilon}} \tag{A.6}$$

where ϵ is the energy required to create an electron-hole pair. Since σ_{ion} is proportional to the variance in the signal charge σ_Q, equation A.6 can be rearranged as:

$$\sigma_Q = \sqrt{F\frac{E_0}{\epsilon}} = \sqrt{FN_Q} \tag{A.7}$$

where F is the Fano factor. The intrinsic resolution of a semiconductor detector can be calculated as:

$$\Delta E_{FWHM} = 2.35\epsilon\sqrt{FN_Q} = 2.35\sqrt{FE\epsilon} \tag{A.8}$$

The Fano factor represents a useful metric to describe the semiconductor internal resolution. However, the energy resolution (ΔE) is also determined by other noise contributions. In particular, it can be shown that in semiconductor detector the internal resolution is typically high, therefore the signal to noise ratio of the system is primarily determined by other noise contributions, such as electronic noise.

A.2.2 Electronic noise

The detector efficiency is influenced by several factors: external interference, imperfect electronics but specifically the electronic noise.

In semiconductor detectors the generated charge current is not stable, but, due to charge carrier movement and interaction point position, it shows time-dependent fluctuations according to:

$$\langle di\rangle^2 = \left(\frac{nq}{w}\langle dv\rangle\right)^2 + \left(\frac{vq}{w}\langle dn\rangle\right)^2 \tag{A.9}$$

The noise is constituted of a velocity component (left-hand side of equation A.9) and a component related to fluctuations in charge carriers (right-hand side of equation A.9). Fluctuations in velocity of carriers are related to the thermal generation and motion described by the limit of Plank's black body. The thermal noise is mostly generated by resistors in the readout electronics and it can be evaluated differently for currents and voltages:

$$\begin{aligned} \frac{di_n^2}{df} &= i_n^2 = \frac{4kT}{R} \quad \text{current} \\ \frac{dv_n^2}{df} &= q_n^2 = 4kTR \quad \text{voltage} \end{aligned} \tag{A.10}$$

where f is the noise frequency, T the absolute temperature and R the resistance of the resistor under investigation. The noise spectral density function is constant over the frequency values, therefore the noise is white noise. The fluctuation in number of charge carriers is due to two factors: carrier trapping and emission over a potential barrier. Carrier trapping effects can occur due to the imperfection of the crystal lattice and its spectral density is given by a power spectrum

$$\frac{dP_n}{df} = \frac{1}{f}^{\alpha} \tag{A.11}$$

where $0.5<\alpha<2$. In trapping situation the noise spectrum is not uniform anymore and the fluctuations are not purely random because of the time constant τ for trapping and releasing of charge carrier. Considering a spectral power density $P_{nf} = S_f/f$ and a voltage density $e_{nf}^2 = A_f/f$, the total noise in a range of frequency band from f_1 to f_2 is:

$$v_{nf}^2 = \int_{f_2}^{f_1} \frac{A_f}{f} df = A_f \ln\left(\frac{f_2}{f_1}\right) \tag{A.12}$$

where A_f is the frequency dependent gain. The fluctuation of the number of charge carriers due to the presence of recombination and generation centres within the semiconductor can be modelled as:

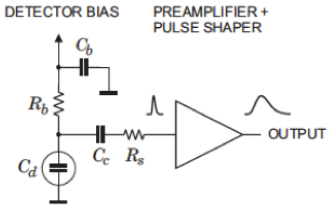

Figure A.2: Amplification chain.

$$\frac{S_{g-r}(f)}{N^2} = \frac{\left(\Delta\bar{N}\right)^2}{N^2}\frac{4\tau}{1+(2\pi f\tau)^2} \tag{A.13}$$

The probability of crossing the voltage barrier is different and independent for each carrier generated. Shot noise is related to the injection of single charge carriers towards the p-n junction. The shot noise is described by:

$$i_n^2 = 2qI\Delta f \tag{A.14}$$

where I is the forward average current.

The total electronic noise, comprised by thermal noise, shot noise and low frequency noise, is obtained integrating the noise power across the working bandwidth. The total electronic noise increases with the square root of the bandwidth and has a Gaussian distribution.

The main contribution to the electronic noise is related to the leakage current and the amplification system. The noise contribution depends also on the signal processing. Each part of the signal processes generates charge movements, which are also related to a generation of noise by the electronic components. In figure A.2 a typical representation of readout scheme is shown. The detector is coupled to a bias supply through a resistor (R_{bias}) and decoupled by a capacitor (C_{bias}). The signal is then passed to the charge preamplifier system and to a pulse shaper

to optimize the signal to noise ratio. The equivalent electronic charge noise can be expressed as equivalent noise charge (ENC), defined as the signal charge that yields a signal to noise (S/N) ratio of one [64]; due to the fact that the deposited energy is transformed in charge, the equivalent noise charge is

$$ENC = Q_n = \frac{Q_S}{S/N} \tag{A.15}$$

where Q_n is the noise charge and Q_S the charge generated by the signal. The energy resolution can be expressed using the ENC as

$$\Delta E_n = E_i \times ENC \tag{A.16}$$

where E_i is the ionization resolution.

As discussed before, the Fano factor and the electronic noise crucially contribute to the definition of the energy resolution of the semiconductor detector. It is interesting to analize how these various effects act together in a real setting. As an example, in figure A.3 it is shown the energy resolution obtained in a 2.5 mm thick CdZnTe detector operated at different energies and at two different temperatures (223 and 253 K). The contribution of the electronic noise is almost constant at the different energy levels and results to be dominant only at low energy values (< 20 keV). At higher energy levels, trapping noise becomes dominant, indeed defining the energy resolution of the system.

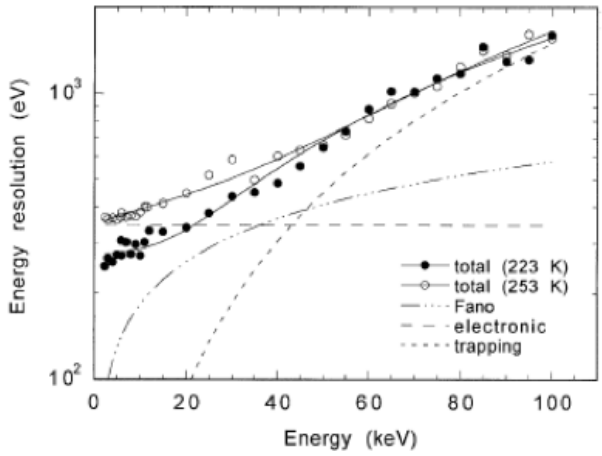

Figure A.3: Energy resolution of 3.1 mm^2, 2.5 mm thick CdZnTe detector [65].

References

[1] International Atomic Energy Agency. *The Fukushima Daiichi Accident.* International Atomic Energy Agency, Vienna„ 2015. https://www-pub.iaea.org/MTCD/Publications/PDF/Pub1710-ReportByTheDG-Web.pdf.

[2] Investigation Committee on the Accident at the Fukushima Nuclear Power Stations of Tokyo Electric Power Company. *Final report.* Cabinet Secretariat of the Government of Japan., 2012. http://www.cas.go.jp/jp/seisaku/icanps/eng/final-report.html.

[3] C. R. (Colin R.) Bayliss and K. F. Langley. *Nuclear decommissioning, waste management, and environmental site remediation.* Butterworth-Heinemann, 2003.

[4] International Atomic Energy Agency. *Costs of Decommissioning Nuclear Power Plants.* International Atomic Energy Agency, Vienna, 2016. https://www.oecd-nea.org/ndd/pubs/2016/7201-costs-decom-npp.pdf.

[5] P. D. Wilson. *The nuclear fuel cycle : from ore to wastes.* Oxford University Press, 1996.

[6] D Delves. *IAEA Safety Glossary Terminology used in Nuclear Safety and Radiation Protection.* International Atomic Energy Agency, Vienna„ 2016.

[7] National Decommissioning Agency. Radioactive Wastes in the UK: UK Radioactive Waste Inventory Report. Technical report, NDA, 2017. https://ukinventory.nda.gov.uk/wp-

content/uploads/sites/18/2014/01/2016UKRWMI-UK-Radioactive-waste-inventory-report.pdf.

[8] Kenneth S Krane. *Introductory Nuclear Physics*. Wiley, 1987.

[9] E. Burge. *Atomic Nuclei and their Particles*. Oxford University Press Inc., New York, second edi edition, 1988.

[10] G. Gilmore. *Practical Gamma-ray Spectrometry*. Wiley edition, 2008.

[11] Nuclide chart. http://www.nndc.bnl.gov/nudat2/.

[12] M.F. L'Annunziata. *Handbook of Radioactivity Analysis*. Academic Press, 2012.

[13] NIST ASTAR. https://physics.nist.gov/PhysRefData/Star/Text/ASTAR.html.

[14] William R. Leo. *Techniques for nuclear and particle physics experiments : A How-to Approach*, volume 58. Springer, 1990.

[15] M. Pfützner, L. V. Grigorenko, M. Karny, and K. Riisager. Radioactive decays at limits of nuclear stability. page 68, nov 2011. http://arxiv.org/abs/1111.0482.

[16] K Nakamura. REVIEW OF PARTICLE PHYSICS * Particle Data Group. *Physics*, 37(7A):075021, 2010. http://stacks.iop.org/0954-3899/37/i=7A/a=075021?key=crossref.de0390bfb70101fa23c6dbe588ea1324.

[17] NIST ESTAR . https://physics.nist.gov/PhysRefData/Star/Text/ESTAR.html.

[18] K Nakamura. REVIEW OF PARTICLE PHYSICS * Particle Data Group. *Physics*, 37:075021, 2010. http://stacks.iop.org/0954-3899/37/i=7A/a=075021?key=crossref.de0390bfb70101fa23c6dbe588ea1324.

[19] V. V. Balashov. *Interaction of particles and radiation with matter*. Springer, 1997.

[20] Thomas, L. H. The calculation of atomic fields. *Proc. Camb. Phil. Soc. 23 (5): 542-548*, 1927.

[21] Fermi, E. Un Metodo Statistico per la Determinazione di alcune PrioprietÃă dell'Atomo. . *Rend. Accad. Naz. Lincei. 6: 602-607.*, 1927.

[22] Schrodinger, E. An Undulatory Theory of the Mechanics of Atoms and Molecules. . *Phys. Rev. 28 (6): 1049-1070.*, 1926.

[23] A. Ashkin J. Bethe and E. Segré. *Experimental Nuclear Physics, Vol. I.* Wiley, 1953.

[24] Glenn F. Knoll. *Radiation Detection and Measurement.* Wiley, 2000.

[25] W. Heitler. *The Quantum Theory of Radiation.* Dover publication edition, 1953.

[26] NIST XCOM. https://physics.nist.gov/PhysRefData/Xcom/html/xcom1.html.

[27] K. Siegbahn. *Alpha-,Beta-, And Gamma-Ray Spectroscopy.* 1965.

[28] Gerhard Lutz. *Semiconductor Radiation Detectors.* Springer Berlin Heidelberg, Berlin, Heidelberg, 2007.

[29] S. M. Sze and K. K. Ng. *Physics of Semiconductor Devices, 3rd.* Wiley, 2007.

[30] Alan Owens. *Compound semiconductor radiation detectors.* CRC Press, 2012.

[31] Claude Leroy and Pier-Giorgio Rancoita. *Silicon Solid State Devices and Radiation Detection.* World Scientific Pub. Co, 2012.

[32] X. Defay et al. Cryogenic silicon detectors with implanted contacts for the detection of visible photons using the Neganov-Luke Effect. *Journal of Low Temperature Physics*, 2016.

[33] L. Casagrande et al. Radiation hard cryogenic silicon detectors. *Nuclear Instruments and Methods in Physics Research Section A:*

Accelerators, Spectrometers, Detectors and Associated Equipment Volume 477, Issues 1-3, 21 January 2002, Pages 299-303, 2002. https://www.sciencedirect.com/science/article/pii/S0168900201018630.

[34] P. Zimmerer. *Performance of cryogenic silicon microstrip detectors at the COMPASS experiment.* PhD thesis, TECHNISCHE UNIVERSITÄT MÜNCHEN, 2011.

[35] S. Ramo. Currents Induced by Electron Motion. *Proceedings of the IRE*, 27(9):584–585, 1939. http://ieeexplore.ieee.org/document/1686997/.

[36] GR1® - Gamma Ray Spectrometer . www.kromek.com/index.php/products/nuclear-technology/czt/gr1-gamma-ray-spectrometer#tab3-content.

[37] Syed Naeem Ahmed. *Physics and Engineering of Radiation and Detection.* 2007.

[38] M. Moll. *Radiation Damage in Slicon Particle Detectors.* PhD thesis, 1999.

[39] E El Allam et al. NIEL calculations for estimating the displacement damage introduced in GaAs irradiated with charged particles. *IOP Conf. Ser.: Mater. Sci. Eng. 186 012005.* https://iopscience.iop.org/article/10.1088/1757-899X/186/1/012005/pdf.

[40] Zheng Jian et al. Isotopic evidence of plutonium release into the environment from the Fukushima DNPP accident. *Scientific Reports*, 2:1–8, 2012.

[41] H. W. Kraner. Radiation Damage in Semiconductor Detectors. *IEEE Transactions on Nuclear Science*, 29(3):1087–1100, 1982. http://ieeexplore.ieee.org/document/4336328/.

[42] J R Srour, Cheryl J Marshall, and Paul W Marshall. Review of Displacement Damage Effects in Silicon Devices. *IEEE TRANSACTIONS ON NUCLEAR SCIENCE*, 50(3), 2003. https://pdfs.semanticscholar.org/5b09/487f24981e4382d0ec5827994dcb2ac2a35f.pdf.

[43] H Dijkstra and J Libby. Overview of silicon detectors. *Nuclear Instruments and Methods in Physics Research Section A: Accelerators, Spectrometers, Detectors and Associated Equipment*, 494(1-3):86–93, nov 2002. http://linkinghub.elsevier.com/retrieve/pii/S016890020201450X.

[44] M. Jamil. Compound Semiconductor Radiation Detectors: Series in Sensors, by Alan Owens. *Contemporary Physics*, 54(2):105–106, apr 2013. http://www.tandfonline.com/doi/abs/10.1080/00107514.2013.777791.

[45] S. Braibant. *Particles and Fundamental Interactions: Supplements, Problems and Solutions: A Deeper Insight into Particle Physics.*

[46] Thomas T Meek, Michael Hu, and Mj Jonathan Haire. Semiconductive Properties of Uranium Oxides. *Waste Management 2001 Symposium*, pages 0–6, 2001. http://www.wmsym.org/archives/2001/14/14-3.pdf.

[47] Kruschwitz C. et al. Semiconductor neutron detectors using depleted uranium oxide. *Conference paper, SPIE*, 9213:92130C, 2014. http://proceedings.spiedigitallibrary.org/proceeding.aspx?doi=10.1117/12.2063501.

[48] Brent M. DeVetter et al. Optical and Chemical Characterization of Uranium Dioxide (UO2) and Uraninite Mineral: Calculation of the Fundamental Optical Constants. *The Journal of Physical Chemistry A*, 2018. https://doi.org/10.1021/acs.jpca.8b05943.

[49] Determination of the Concentrations for Radioactive Elements Around Al-Tuwaitha Center Using Gamma-Ray Spectroscopy and CR-39 Detectors. https://www.researchgate.net/publication/328725347_Determination_of_the_Concentration Tuwaitha_Center_Using_Gamma-Ray_Spectroscopy_and_CR-39_Detectors.

[50] Agostinelli S. et al. Geant4-a simulation toolkit. *Nuclear Instruments and Methods in Physics Research Section A: Accelerators, Spectrometers, Detectors and Associated Equipment*, 506(3):250–303, jul 2003. http://www.sciencedirect.com/science/article/pii/S0168900203013688.

[51] Allison J. et al. Recent developments in Geant4. *Nuclear Instruments and Methods in Physics Research Section A: Accelerators, Spectrometers, Detectors and Associated Equipment*, 835:186–225, nov 2016. http://www.sciencedirect.com/science/article/pii/S0168900216306957.

[52] Janez Megusar. Low temperature fast-neutron and gamma irradiation of Kapton® polyimide films. *Journal of Nuclear Materials*, 245(2-3):185–190, 1997. http://www.sciencedirect.com/science/article/pii/S0022311597000123.

[53] DATASHEET MAROC3. https://www.ge.infn.it/ musico/DownloadFiles/-Maroc/datasheet_MAROC3_V7.pdf.

[54] Prototype of the Front-end Circuit for the GOSSIP-1.

[55] Baesso P. et al. High resolution muon tracking with resistive plate chambers. *Journal of Instrumentation*, 7(11):P11018–P11018, 2012. http://stacks.iop.org/1748-0221/7/i=11/a=P11018?key=crossref.72ee26eba08d154d632b60af80f6edaf.

[56] Baesso P. et al. A high resolution resistive plate chamber tracking system developed for cosmic ray muon tomography. *Journal of Instrumentation*, 8(08):P08006–P08006, 2013. http://stacks.iop.org/1748-0221/8/i=08/a=P08006?key=crossref.b575d00f68e68c7333b959c104999f3c.

[57] P. Martin et al. Development and validation of a high-resolution mapping platform to aid in the public awareness of radiological hazards. *Journal of Radiological Protection, Volume 38, N. 1*, 2018. https://iopscience.iop.org/article/10.1088/1361-6498/aaa914/meta.

[58] Brandl A. Johnson T.E. Steinhauser, G. Comparison of the Chernobyl and Fukushima nuclear accidents: a review of the environmental impacts. *Sci. Total Environ. 470–471, 800–817*, 2014.

[59] Malins A. et al. Fields of View for Environmental Radioactivity, in: Proceedings of the International Symposium on Radiological Issues for Fukushima's Revitalized Future, 2015.

[60] ShikazeY. et al. Field test around Fukushima Daiichi nuclear power plant site using improved Ce:Gd3(Al,Ga)5O12 scintillator Compton camera mounted on an unmanned helicopter. *J. Nucl. Sci. Technol. 1–12*, 2016.

[61] Sanada Y. and Torii T. Aerial radiation monitoring around the fukushima daiichi nuclear power plant using an unmanned helicopter. *J. Environ. Radioact. 139, 294–249*, 2015.

[62] Gageik N. et al. An Autonomous UAV with an Optical Flow Sensor for Positioning and Navigation. *International Journal of Advanced Robotic Systems*, 2013. https://doi.org/10.5772/56813.

[63] Shen C. et al. Optical Flow Sensor/INS/Magnetometer Integrated Navigation System for MAV in GPS-Denied Environment. *Journal of Sensors*, 2016, 2016. http://dx.doi.org/10.1155/2016/6105803.

[64] Helmuth. Spieler. *Semiconductor detector systems.* Oxford University Press, 2005.

[65] A. Owens. The X-ray response of CdZnTe. *Nuclear Instruments and Methods in Physics Research Section A: Accelerators, Spectrometers, Detectors and Associated Equipment*, pages 242–250, 2002.